

# UNIMORE

UNIVERSITÀ DEGLI STUDI DI  
MODENA E REGGIO EMILIA

Behnood Dianat

## **Chalcogenide Glasses for Memory Switching Applications**

Focusing on Modelling and Simulation  
aspects

**Department of Sciences and Methods for Engineering**

Advisor: Prof. Giovanni Verzellesi

Co-Advisor: Prof. Luca Larcher

Director of the School: Prof. Franco Zambonelli

Thesis submitted in fulfillment of the requirements for the degree of Doctor of Philosophy

**2021**



© Behnood Dianat, 2021

*Dissertation submitted to the  
, University of Modena and Reggio Emilia*



*To everyone who supported me throughout this path...*



# Preface

This thesis is submitted in partial fulfillment of the requirements for the degree of *Doctor of Philosophy* at the University of Modena and Reggio Emilia. The research presented here was conducted at the University of Modena and Reggio Emilia, under the supervision of professor Luca Larcher and professor Giovanni Verzellesi.

The thesis is a collection of four papers, presented in chronological order of writing as chapter 3-6. The papers are preceded by an introductory chapter that relates them to each other and provides background information as well as the methodologies of the work.

## Acknowledgements

My Ph.D. would not have been possible without the guidance of Prof. Giovanni Verzellesi, Prof. Luca Larcher, Prof. Arrigo Calzolari and a special thanks to Dr. Andrea Padovani for all his efforts in my supervision.

• **Behnood Dianat**  
Reggio Emilia, April 2021





# Contents

Preface	iii
Contents	v
List of Figures	vii
List of Tables	xiii
<b>1 Introduction</b>	<b>3</b>
1.1 Phase-change memory selectors . . . . .	6
1.2 Optical properties . . . . .	9
1.3 Atomic Structure properties . . . . .	11
1.4 Molecular dynamics simulations and its challenges . . . . .	11
1.5 Thesis outline . . . . .	12
References . . . . .	12
<b>2 Methodology</b>	<b>19</b>
2.1 Multiscale Modeling Simulations . . . . .	19
2.2 Density Functional Theory . . . . .	26
References . . . . .	31
<b>Results</b>	<b>34</b>
<b>3 Multiscale modeling of CeO<sub>2</sub>/La<sub>2</sub>O<sub>3</sub> stacks for material/defect characterization</b>	<b>35</b>
3.1 Introduction . . . . .	35
3.2 Device experiments and simulations . . . . .	36
3.3 Results . . . . .	37
3.4 Conclusion . . . . .	39
References . . . . .	41
<b>4 BELLO: a script tool for bond element and lattice local-order analysis of disordered systems</b>	<b>43</b>
4.1 Introduction . . . . .	43
4.2 Software Design . . . . .	45
4.3 Description of the code . . . . .	46
4.4 Installation, input and Output structure . . . . .	52
4.5 User Inputs . . . . .	54
4.6 Module outputs . . . . .	56
4.7 Conclusion . . . . .	60

References . . . . .	60
<b>5 Hierarchical short- and medium-range order structures in amorphous <math>\text{Ge}_x\text{Se}_{1-x}</math> for selectors applications</b>	<b>63</b>
5.1 Introduction . . . . .	64
5.2 Methods . . . . .	66
5.3 Results and Discussion . . . . .	67
5.4 Conclusion . . . . .	76
5.5 Associated content . . . . .	77
References . . . . .	77
<b>6 A first principle study of the switching mechanism of <math>\text{Ge}_{54}\text{Te}_{216}\text{As}_{20}\text{Se}_{30}</math> for selectors applications</b>	<b>83</b>
6.1 Introduction . . . . .	83
6.2 Methodology . . . . .	84
6.3 Results and Discussion . . . . .	85
6.4 Conclusion . . . . .	91
References . . . . .	91
<b>7 Conclusion</b>	<b>95</b>

# List of Figures

1.1	von Neumann architecture of modern computer . . . . .	3
1.2	Neuron structure in the human brain [int4] . . . . .	4
1.3	Infrared reflectance spectra of a 1 $\mu m$ thin film of GeSb <sub>2</sub> Te <sub>4</sub> with a metallic substrate. A visible difference of the optical characteristics between the amorphous (dotted-line) and the crystalline-state (solid-line) is visible. The crystalline state is characterized by a lower optical band-gap, as evidenced by the fact that reflectance oscillations are observed for a smaller energy range and a higher refractive index, which leads to a smaller spacing of adjacent reflectance maxima. Both differences are related to a change of bonding upon crystallization [int3] . . . . .	7
1.4	Application of phase-change materials on a phase-change optical disc, b PCRAM, c scanning probe phase-change memory, and d phase-change photonic memory . . . . .	8
1.5	Schematic of a thermal switching and b electrical switching (i.e. threshold switching) in phase-change materials . . . . .	9
1.6	a) a treasure map for the phase change materials, b) The modes of crystallization in PCMs are either nucleation driven GST or AIST, The transmission electron microscope (TEM) images show the crystallized states upon heating (marked by the red circles). The TEM images show the outcome of a recrystallization experiment. The region marked by the red circles corresponds to the recrystallized PCM upon heating. In the case of GST, this region displays a clear contrast with its crystalline surrounding owing to the difference in grain size and orientation, showing that crystallization was driven by nucleation. By contrast, AIST exhibits no contrast, indicating a smooth crystal growth from the boundary, yielding a single-crystalline state. The distributions of primitive rings of different size in amorphous GST and AIST are shown in panels c and d. c) Fourfold primitive rings are the dominant structural fragments in amorphous GST. The inset shows an amorphous model of GST, with two ABAB squares and a cube A=Ge B=Sb,Te highlighted. d) In amorphous AIST, the distribution of primitive rings is broad, with fivefold primitive rings being the most abundant structural fragments. The inset shows an amorphous model of AIST, in which some fivefold primitive rings are highlighted. Ge, Sb, Te, Ag and In atoms are rendered in grey, yellow, blue, orange and purple, respectively. The TEM images in panel b are reproduced from [int272] . . . . .	10

2.1	Schematic representation of the different carriers transport mechanisms considered in Ginestra(R): (a) tunneling and others; (b) trap-assisted. The mechanisms are numbered as follows: (1) drift-diffusion; (2) thermionic emission; (3) direct tunneling; (4) electrode-band tunneling; (5) intra-band tunneling; (6) band-to-band tunneling; (7) local generation-recombination; (8) electrode-to-trap capture, $R^{in,el}$ ; (9) trap-to-electrode emission $R^{out,elg}$ ; (10) trap-to-trap transition, $R^{TT}$ ; (11) trap-to-band transition, $R^{TTB}$ . The mechanisms are shown for the case of electron transport, but the same holds for holes transport. . . . .	23
2.2	Schematic representation of the transition rates considered in the calculation of $R_{in,j}$ and $R_{out,j}$ in equation below for a simple case of three traps . . . . .	23
2.3	(a) Band diagram illustrating an example of multi-phonon capture and emission processes in the case of a single-trap conductive path. A monolayer stack has been considered for simplicity. (b) Full energy configuration coordination diagram corresponding to the processes. (c) Representation of the possible transitions between the different resonant vibrational eigenfunctions . . . . .	24
2.4	Schematic representation of the self consistent cycle of density-functional theory: initializing from an approximated density value $n_0$ the Hamiltonian is generated via calculating the exchange-correlation and Hartree potentials $V_{xc}$ and $V_H$ respectively. Then, solving the Kohn-Sham equation for eigen-energies $\epsilon_k$ and wavefunctions $\phi_k$ are calculated resulting in a density value $n_{i+1}$ . The process is repeated until reaching a predefined convergence threshold is reached, it is done by mixing the old and new density values before entering the next step. . . . .	29
3.1	Schematic representation of the different carrier transport mechanisms considered in GINESTRA <sup>TM</sup> , mechanisms are shown in two similar devices for better comprehension. (1) drift-diffusion, (2) thermionic emission, (3) direct tunneling, (4) electrode-band tunneling, (5) intra-band tunneling, (6) band-to-band tunneling, (7) local generationrecombination, (8) electrode-to-trap capture, (9) trap-to-electrode emission, (10) trap-to-trap transition, RTT, (11) trap-to-band transition, RTTB were used for calculations. . .	36
3.2	C-V fittings for a) CeO <sub>2</sub> and b) La <sub>2</sub> O <sub>3</sub> monolayers to that of the reports from literature [ <b>papi11</b> , <b>papi12</b> ], simulations and experimental data are shown with lines and symbols respectively.	38
3.3	Temperature-dependent J-V curves reproduced from five sets of experimental data (a-e) for La <sub>2</sub> O <sub>3</sub> and CeO <sub>2</sub> which were collected from literature [ <b>papi11</b> ] [ <b>papi15</b> , <b>papi16</b> , <b>papi17</b> , <b>papi18</b> ]. For the sake of comparison the simulations are drawn with lines and experimental data are displayed by symbols. . . . .	38

3.4	Depicting J-V curves of CeO <sub>2</sub> /La <sub>2</sub> O <sub>3</sub> stack fittings of reported experimental results [papi19], a comparison between charge transport with (solid lines) and without (dashed lines) TAT are visible. Experimental data are demonstrated by symbols. . . . .	39
3.5	Illustration of La <sub>2</sub> O <sub>3</sub> and CeO <sub>2</sub> bandgap. Orange rectangle represents the range of defect energies extracted by GINESTRA <sup>TM</sup> and blue lines represent calculated neutral and charged oxygen vacancies from DFT calculations reported in literature. . . . .	40
3.6	Bandgap plot of bilayer CeO <sub>2</sub> /La <sub>2</sub> O <sub>3</sub> , scattered dashes represent energy traps. . . . .	40
4.1	Schematic representation of the applied boundary conditions, trajectories with atoms outside of unitcell (a) are move inside (b). atomic distances between the central atom (#2) and the ligands (#2') are calculated considering the boundary condition. (d) shows angle calculation process between ligands. . . . .	47
4.2	Local order geometries with their corresponding q values. . . . .	47
4.3	Total q value illustrated from total-q-output. . . . .	48
4.4	Local order geometries with their corresponding q values. . . . .	48
4.5	3D visualization from PDB module's output for super-cell of chalcogenide Ge <sub>54</sub> Te <sub>216</sub> As <sub>20</sub> Se <sub>30</sub> . . . . .	49
4.6	Bond angle distribution function of Te-Ge-Te from extracted local orders of crystalline Ge <sub>54</sub> Te <sub>216</sub> As <sub>20</sub> Se <sub>30</sub> . . . . .	49
4.7	Local order population variations of extracted statistics corresponding to the trajectory frames. The plot belongs to molecular dynamics simulation from Ge <sub>54</sub> Te <sub>216</sub> As <sub>20</sub> Se <sub>30</sub> . . . . .	50
4.8	Output windows of matplotlib library depicting radial distribution function of GeTe4. . . . .	51
4.9	Detailed coordination number table of extracted geometries from GeTe4. results with 0 value are not reported. (a)(b) illustrates the highlighted structures of local orders corresponding to (a) GeTe <sub>2</sub> and (b) Ge <sub>2</sub> Te <sub>3</sub> . . . . .	52
4.10	Graphic illustration of BELLO's workflow starting from a single trajectory file. Detailed-coordination-number module takes advantage of the Human-readable output produced from BELLO-core to generate coordination number for three types of elements. . . . .	53
4.11	Listing 1 . . . . .	53
4.12	Listing 2 . . . . .	54
4.13	Listing 3 . . . . .	55
4.14	Listing 4 . . . . .	56
4.15	Listing 5 . . . . .	56
4.16	Listing 6 . . . . .	57
4.17	Listing 7 . . . . .	57
4.18	Listing 8 . . . . .	57
4.19	Listing 9 . . . . .	58
4.20	Listing 10 . . . . .	58

## List of Figures

---

4.21	Listing 11 . . . . .	59
4.22	Listing 12 . . . . .	59
5.1	Sample of configurations of (a) 4-fold, (b) tetrahedral, and (c) octahedral structures. (d) The 0-fold, 1-fold, and 2-fold atoms with respective connections scheme rendered as solid spheres, while the neighboring atoms as transparent ones. Color codes for all folds are given at the bottom. . . . .	65
5.2	Radial distribution function, $g(r)$ , for the amorphous phase at 300 K for each $\text{Ge}_x\text{Se}_{1-x}$ system: (a) Ge-Ge, (b) Ge-Se, and (c) Se-Se interactions. . . . .	68
5.3	Faber-Ziman total static structure factors for melt (a) and amorphous (b) phases. Each composition is represented with a different color as shown in the legend above. . . . .	69
5.4	Faber-Ziman partial static structure factors for melt (right) and amorphous (left) phases. Each composition is represented with a different color, as shown in the legend at the top. (a, d) Ge-Ge $\text{Sn}(k)$ , (b, e) Ge-Se $\text{Sn}(k)$ , (c, f) Se-Se $\text{Sn}(k)$ . . . . .	70
5.5	Percentage of folded atoms for each $\text{Ge}_x\text{Se}_{1-x}$ system during the simulation time. The first 10 ns correspond to the melt, the jump corresponds to the quenching, and the last 50 ns correspond to the amorphous phase. In red, data for $\text{Ge}_{0.4}\text{Se}_{0.6}$ ; in green, data for $\text{Ge}_{0.5}\text{Se}_{0.5}$ ; and in blue, data for $\text{Ge}_{0.6}\text{Se}_{0.4}$ . . . . .	71
5.6	Bond angle distribution of Ge-Se-Ge (a) and Se-Ge-Se (b) in amorphous $\text{Ge}_x\text{Se}_{1-x}$ systems at 300 K. . . . .	74
5.7	Ring size probability for $\text{Ge}_x\text{Se}_{1-x}$ systems. . . . .	75
5.8	Connectivity profiles for the $\text{Ge}_x\text{Se}_{1-x}$ system: (a) $\text{Rc}(n)$ , (b) $\text{PN}(n)$ , (c) $\text{Pmin}(n)$ , and (d) $\text{Pmax}(n)$ . . . . .	76
6.1	Radial distribution functions for $\text{GeTe}_4$ (undoped) and $\text{As}_2\text{Se}_3$ (doped) for different element correlations a) Ge-Ge b) Ge-Te c) Te-Te, 10 Å is chosen as the maximum distance for RDF as the first neighbour is in the vicinity of 3 Å. . . . .	86
6.2	Radial distribution functions for ASGT illustrating the correlation between different elements present in the system a) As-As b) As-Se c) Ge-As d) Ge-Se e) Se-Se f) Te-As g) Te-Se. . . . .	86
6.3	Density of state for a) $\text{GeTe}_4$ and b) ASGT ( $\text{As}_2\text{Se}_3$ ) from liquid to solid phases, higher temperatures are illustrated by faded colors, Fermi levels are at 5.7 eV and 8.2 eV for $\text{GeTe}_4$ and ASGT respectively. . . . .	87
6.4	Statistical representation of local order population variations throughout the atomic structure trajectories for a) $\text{GeTe}_4$ b) $\text{As}_2\text{Se}_3$ . the noise in (a) is due to the high number of frames. . .	88

6.5	Order parameter $q$ values shown for a) $\text{GeTe}_4$ b) $\text{As}_2\text{Se}_3$ . arbitrary values are normalized to unit cell density as well as trajectory size. overall increase of the $q$ parameter indicates a more organized atomic structure. . . . .	88
6.6	Present geometrical shapes and their corresponding $q$ value. . . .	88
6.7	Snapshot of the last frame of ASGT structure with only a) 3-Fold b) 4-Fold geometries present. . . . .	89
6.8	Bond angle distribution function for $\text{GeTe}_4$ for a) Te-Te-Ge b) Te-Te-Te c) Ge-Ge-Ge d) Te-Ge-Te e) Ge-Ge-Te f) Te-Ge-Ge g) Ge-Te-Ge h) Ge-Te-Te, axis scale values are changed accordingly. . . . .	89
6.9	Bond angle distribution function for ASGT for angles of a) Te-Te-Te b) Te-Te-Te c) Ge-Te-Ge d) Te-Te-As e) Ge-Te-Te f) Te-Se-Te g) Te-Ge-Se h) Te-Ge-Te. a more pronounced distribution of angles at 90 and 180 degree is observable in comparison with the undoped structure. . . . .	90





# List of Tables

3.1	Table of extracted parameters . . . . .	37
5.1	Percentage (%) of Folded Atoms for Each $\text{Ge}_x\text{Se}_{1-x}$ Amorphous System Computed on the Last 10 ns of Simulations <sup>a</sup> . . . . .	72
5.2	Ring Size Counts for $\text{Ge}_x\text{Se}_{1-x}$ Systems . . . . .	74



## Abstract

Surpassing the standard von Neumann computer architecture calls for new architecture schemes and specifically tailored new materials. Among possible candidates, human brain inspired neuromorphic computers have attracted many attentions. Realization of neuromorphic computers demands for the development of Non-Volatile Memories (NVM) such as Phase-Change random access memories (PCRAM) based on Phase-Change Materials (PCM) as well as memories based on chalcogenide glass selectors. Chalcogenide glasses are a vast spectrum of materials that can switch between amorphous and crystalline phase. A pronounced change in the optical properties accompanies the electrical resistance contrast during the fast and reversible phase changes of chalcogenide materials. Electrical resistance changes by several orders of magnitude between amorphous and crystalline phase, due to a change from covalent to metavalent bonding. Moreover, chalcogenide glasses display high linear and non-linear current voltage curves at different voltages.

In this work, we initially investigate the defect and material characterization of  $\text{La}_2\text{O}_3$  and  $\text{CeO}_2$  high-k dielectric constant materials as gate oxide materials in MOSFETs. We present a simulation-based methodology, relying on an accurate description of charge trapping and transport that is useful to extract relevant information on material and defect characteristics. This methodology was applied to cerium oxide and lanthanum oxide high-k dielectric materials and as a result, material properties alongside defect characteristics were extracted. Consequently, main charge conduction mechanism throughout the device was identified to be the trap-assisted tunneling (TAT).

Then in the second chapter, we introduce a python script-tool for autonomous extraction and characterization of statistical parameters of disordered materials. The aim of the project was to establish a methodology for the structural analysis of amorphous chalcogenide phase-change materials. The code utilizes NumPy and Pandas standard libraries and functions by loading the standard atomic structure trajectories or single configuration from the molecular dynamics calculations as input, subsequently, calculating interatomic distances and angles via trajectory analysis resulting in the extraction of parameters such as: order parameter  $q$ , a detailed coordination number, radial and angle distribution functions, local population statistics and local order coordinates in PDB and XYZ formats. Furthermore, the code is agnostic to the code that generated the single configuration or trajectories as well as the elements of the structure. After that, the third chapter thoroughly investigates the hierarchical short- and medium-range order structures in amorphous glasses for selectors applications. Our study includes an in-depth analysis of the relationship between the bonding mechanisms and the resulting physical properties. By employing the molecular dynamics, we study the structural features such as short-range local orders of both the liquid and amorphous phase in Ge-based chalcogenide binary  $\text{Ge}_x\text{Se}_{1-x}$  systems in the range  $0.4 < x < 0.6$ . Our results indicate the formation of temperature-dependent hierarchical structures with short-range local orders and medium-range structures, which vary with the Ge content. Our classical molecular dynamics

simulations are able to describe the profound structural differences between the melt and the glassy structures of GeSe chalcogenides. These results set the path for understanding the interplay between chemical composition, atomic structure, and electrical properties in switching materials.

Finally, In the fourth chapter, we present a first principle study of the switching mechanism of  $\text{Ge}_{54}\text{Te}_{216}\text{As}_{20}\text{Se}_{30}$  for Memory applications, The electrical and structural properties of  $\text{GeTe}_4$  and the effects of  $\text{As}_2\text{Se}_3$  are studied in the framework of ab initio simulations coupled within the Carr-Parrinello approach and density functional theory. The structural analysis are carried out via utilizing the BELLO code for structural trajectories. In order to simulate the electrical switching behavior of chalcogenide glasses in selectors, the systems are melted up to their melting temperature then quenched back down to 300K. The correlation between the amorphous and crystalline phases are thoroughly studied via our statistical approaches coupled with density functional calculations. Our findings paved new routes towards thermal approaches in chalcogenide glasses studies for switching materials.

# Chapter 1

## Introduction

Currently available computers are considered a breakthrough in human history, they have a considerable impact on our everyday activities such as business, education, entertainment, and sports. Though the functions vary based on the operational system, advancement of the digital computer mainly relies on the progress of both the hardware and software technologies. Recent technological developments on ultra-large-scale integration (ULSI) allow millions or even billions of electronic components to be integrated on a single semiconductor chip, thus, substantially improving the efficiency of the modern computer. Therefore, it is reasonable to picture a future where the human-machine integration is possible. However, currently the architectural difference between computer and human brain are the bottleneck which hinders this goal. It is well known that modern computer usually makes use of the so-called von Neumann architecture that consists of three main components [1], i.e. processor, main memory, and bus, as shown in Figure 1.1. The processor, also known as central processing unit (CPU), comprises arithmetic logic unit (ALU), control unit, and register. As implied by their names, ALU is responsible for all the arithmetic and logical operations such as addition, subtraction, AND, and OR functions, while the control unit decodes the instructions and controls all other internal components of the CPU. Storing the data during execution is done by the register. Then the CPU sends the processed data to Memory for storage. Moreover, address bus and control bus are employed to determine the address of the data inside the memory and the type of the operations (e.g. write and read) between CPU and memory, respectively. According to the descriptions above, the key feature of

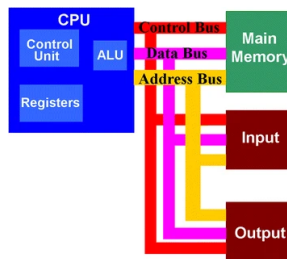


Figure 1.1: von Neumann architecture of modern computer

these computer adoptions of von Neumann architecture is the data is processed and stored by different units in separate places. Thus, increasing the steps for the CPU to retrieve data from the main memory for any computations, after which the data is sent back to the main memory for storage. Considering that for the modern computers the bandwidth between CPU and the main memory is much

lower than the speed that a typical CPU can work, which substantially impacts the processing speed. For solving the problem of von Neumann architecture, several schemes such as Cache memory, multi-threading core, and low-latency command channel have been proposed in the past. Though these approaches seem feasible for the less repetitive operations that only handle small tasks, they do not meet the demands from data-centric applications that usually require repetitive operations on a big data structures such as real-time image recognition and natural language processing[2] Therefore, it is only reasonable to think that a transition from von Neumann architecture to a more efficient scheme is inevitable. Fortunately, an ideal computing system other than von Neumann architecture is available in nature, human brain. The human brain has multiple types of cells within which the main one is known as neuron[3] as shown in Figure 1.2. The neurons in human brain have the ability to process and transmit information through electrical and chemical signals. These Information mostly in the form of an electrical or chemical signal are transmitted from one axon to the other one in neighboring neurons, the conjunction of these axons and the dendrites of the next neuron are called synapse. The synapse has the

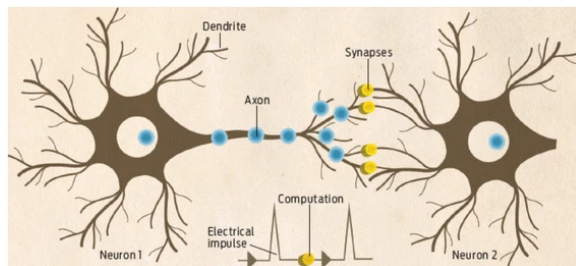


Figure 1.2: Neuron structure in the human brain [3]

ability to evaluate the data via integration in comparison to the synaptic weight, Therefore, sending it to other neurons via their respective axons. Contrary the current computers, the main differing feature of the human brain is that it processes the information while transferring it, thus leaving only a single value by the time that information reaches the neighboring neurons. This promising discovery indicates that human brain allows both data storage and processing to occur at the same time in neurons. Considering that human brain contains about 1011 neurons and 1015 synapses which enables an operation frequency of 1–10 Hz on the power budget of 10–100 W [4] corresponding to an energy consumption of 1–10 fJ per synaptic event[4] The excellent features of the human brain make its architecture a candidate for building a super-intelligent computer which replicates the neural network system of the human brain to completely surpass the von Neumann architecture, Thus, elevating artificial intelligence (AI) technologies to the next level. One of the possible approaches to obtain brain-like computer is the implementation of the behaviors and connections between biological neurons inside the human brain using conventional computers

or even so-called supercomputers in software forms. Despite its capabilities such as flexibility and availability[5][6] the software-based approaches fail to cope with large-scale tasks like pattern recognition, learning, and intelligent cognition[7][8] Furthermore, consuming several more amounts of power compared to that of the human brain[9] In this case, a considerable portion of the recent investigations has been directed towards exploiting a novel hardware architecture which emulates both the biological structure and function of the human brain, concluding the fact that the neuromorphic engineering concept dating back as early as 1980s are feasible approaches[7]. One of the promising methods is further scaling the digital Complementary Metal Oxide Semiconductor (CMOS) technology, which forms the basis for logic circuits within microprocessors and systems on a chip used in computers. This is done by implementing High K and Metal Gate (HKMG) stacks within the Metal Oxide Semiconductor Field Effect Transistors (MOSFETs). Among these materials, lanthanides have shown to improve MOSFET characteristics, such as channel mobility, sub-threshold slope and control over negative threshold voltage shift. Moreover, although lacking, a clear assessment and characterization of the traps present in these materials is crucial for technology optimization as well as for identifying their potential as gate dielectric stacks. However, the concept of neuromorphic computing has not received sufficient attentions until the presence of the emerging non-volatile memories (NVM) such as Ferroelectric Random-Access Memory (FeRAM)[10][11] magnetic random-access memory (MRAM)[12][13] phase-change random-access memory (PCRAM)[14][15] and resistive random-access memory (ReRAM)[16][17] as well as the physical realization of the early proposed ‘memristor’ concept[18][19][20] These contemporary tailored devices have the ability to store data on an ultra-small region during ultra-short interval with minimum energy consumption, resembling the properties of human brain. Moreover, electrical and physical characteristics of such devices which depend on the previous states can be accordingly modified using the external stimulus thus granting them storage capability while in power-off mode. As a result, thin-film based electronic devices consisting of metal oxides[21][22] solid-electrolytes[23][24] carbon nanotubes[25][26] organic electronics[27][28] spin transfer torque MRAM[29][30] and phase-change memory (PCM)[31] based on the mentioned technologies are developed in hope of systematically mimicking the biological function of the human brain, especial interests are focused on the learning and memorization features arising from the synapses. It is worthy to note that the complex structure of the human brain has made this task more challenging, thus, none of these devices were able to demonstrate promising results for neuromorphic computers, whether it might be in the form of physical properties or energy efficiency. However, synaptic-like electronic devices build upon ReRAM and especially PCM technologies are much more promising than its predecessors since phase-change materials have already established their place in industrial applications such as the conventional optical disc[32] to the innovative all-photonics memory[33] Thus, PCRAM is thought to be the leading candidate for the so-called universal memory for NVM applications[34][35] Additionally, a good proportion of theoretical knowledge and experimental methods which relates to

the electrical, optical, thermal, and mechanical properties of the Phase-change memories have already been accomplished along with the development of PCMs that has been extensively studied for the past two decades. Considering the aforementioned facts, a thorough review of the physical and electronic aspects of the phase-change materials and memories for neuromorphic computing becomes indispensable.

## 1.1 Phase-change memory selectors

Currently, industries have realized flash memories via extensive 3D stacking [36][37][38]. In these systems, the three-dimensional cross-point arrays interconnected by selectors can reduce the single cell size to an effective footprint of  $4F^2$ . aside from the MOSFETs which require major breakthroughs, other options are not suitable for the 3D structure owing to the scaling problem. Hence, in order to achieve a small scale while containing a high density a considerable amount of interest has been focused towards the cross-point memory array [39][40][41][42][43]. The concept of 3D stacking of selectors for memory applications has been around since 1950s [44]. However, industries have not yet fully commercialized its applications for cross-point memory. Firstly because of the fabrication problems for manufacturing dense 3D memories with high reliability and high yield, while the development of technology nodes will enable manufacturing processes to surpass this problem. The other reason is that a 3D cross-point memory demands a durable non linearity device-cell (selector) at every connection join to aid the driving current to the desired memory device without interrupting any of the other memory cells in On states while reducing the leakage currents in Off states. The leakage currents have a substantial influence on the energy consumption level of the device considering that the array includes thousands or millions of cross-points. Thus, finding a selector that satisfies all these criteria is difficult, making it the bottleneck for 3D integration. However, the detailed interplay between the parameters that characterize the materials (e.g., structure, composition, doping, and chemical and thermal stabilities) and the influence they have on the device characteristics (e.g., data retention, power consumption, and switching time) has not been completely understood.

Amorphous chalcogenides such as  $Ge_xSe_{1-x}$  compounds have been proposed as ovonic switching materials[45] for both nonvolatile memory devices and selectors[46] in view of their high ON-state drive current, good half-bias linearity, fast switching, endurance, and a higher crystallization temperature with respect to, e.g., GST or GeSbSeTe materials[47]. First experimental evidences indicate that the modulation of the stoichiometry ratio affects the electrical response of the device, in terms of both I-V characteristics and power dissipation[48]. In particular, devices based on Ge-rich GeSe compounds exhibit a high OFF current and a low threshold voltage[49][50], while Se-rich GeSe-based devices have a higher energy gap, a lower OFF-state leakage current, and a higher thermal stability[51]. The origin of this behavior is still unknown: while much effort has been dedicated to GeTe as a prototypical phase change material, or to GeSe2 as



an efficient opto-electronic system, very little is known on quasi-stoichiometric  $Ge_xSe_{1-x}$  compounds.

### 1.1.1 Phase-Change Materials

Phase-change materials adaptations for neuromorphic computing usually refers to chalcogenide alloys which include Ge, Sb, and Te. Interesting features of phase-change materials are their ability to switch reversibly between a metastable amorphous phase with high electrical resistivity and low optical reflectivity and a stable crystalline phase with low electrical resistivity and high optical reflectivity caused by either electrical or optical stimulus. These different properties of the electrical and optical characteristics between the two crystalline and amorphous phases make phase-change materials great candidates for applications in non-volatile memory industry such as optical disc[32] PCRAM[34] scanning probe phase-change memory[35][52][53] and phase-change photonic device[54][55][56] as shown in Figure 1.3. achieving crystallization requires an electric pulse to be applied to the materials at amorphous state to bring its temperature above glass transition temperature but below melting temperature by means of the resulting Joule heating, then followed by a slow cooling process. This procedure

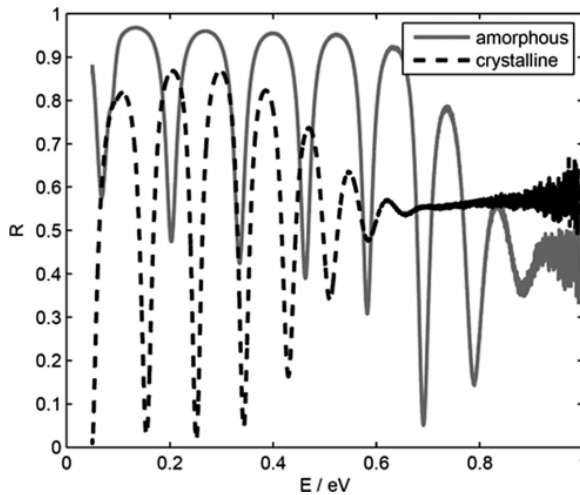


Figure 1.3: Infrared reflectance spectra of a  $1 \mu m$  thin film of  $GeSb_2Te_4$  with a metallic substrate. A visible difference of the optical characteristics between the amorphous (dotted-line) and the crystalline-state (solid-line) is visible. The crystalline state is characterized by a lower optical band-gap, as evidenced by the fact that reflectance oscillations are observed for a smaller energy range and a higher refractive index, which leads to a smaller spacing of adjacent reflectance maxima. Both differences are related to a change of bonding upon crystallization [2]

is usually called the ‘SET’ operation for phase-change materials. Moreover,

amorphization is done via heating the material above melting temperature and then fast quenching it to room temperature, this process is carried out using electrical pulses as well which is referred to as ‘RESET’. generally, the time of SET operation is about a few hundreds of nanoseconds, while ‘RESET’ takes in the range of a few of tens of nanoseconds or even down to picosecond regime. Figure 1.5.a. shows the SET and RESET process in detail. Additionally, phase-change materials tend to present a distinctive electrical switching as well called ‘threshold switching’[57][58][59] Due to this effect (Figure 1.5.b), while in amorphous state, once the bias voltage exceeds the threshold value, electrical resistance of the phase-change material will dramatically drop, resulting in a high current flow for the incoming crystallization. Due to this feature, phase change materials have the ability to phase change at relatively low voltages. Otherwise, phase transition can only occur using very high voltages that results in high power consumption. These characteristics in conjunction with considerable practical and theoretical knowledge obtained from the applications of phase-change materials for NVM field during the last two decades successfully endow phase-change materials with several advantageous features such as an excellent scalability of  $<5$  nm[60] a fast switching speed of  $<1$  ns[61] a long cycle endurance of  $>10^{12}$ [16] and a low energy consumption of less than a petajoule per bit[62] Hence setting the path for using phase change materials to replicate the biological synapse.

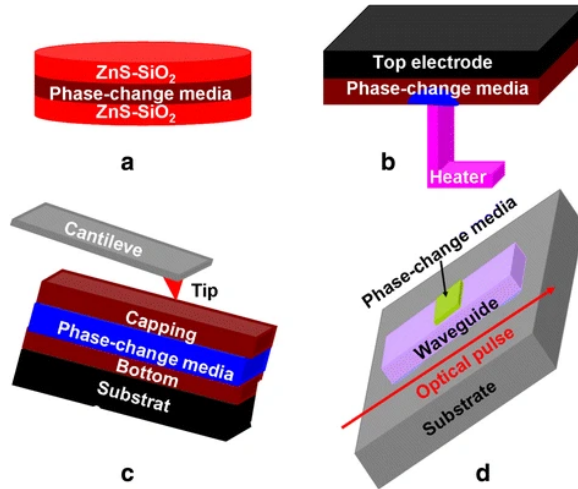


Figure 1.4: Application of phase-change materials on a phase-change optical disc, b PCRAM, c scanning probe phase-change memory, and d phase-change photonic memory

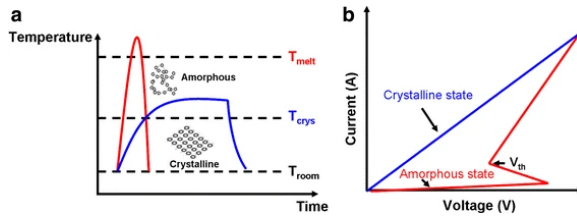


Figure 1.5: Schematic of a thermal switching and b electrical switching (i.e. threshold switching) in phase-change materials

## 1.2 Optical properties

Usually in solid state physics, the crystalline solid is the main focus. The existence of long-range order leads to the formation of unique electronic states, the so-called Bloch electrons. The material characteristics vary based on the crystal structure and the type of atoms in the unit cell of the crystal which can be calculated methodologies such as density functional theory (DFT). But the amorphous state, due to its non-periodic feature requires especial attention, therefore many methodological and theoretical concepts which predict the properties of crystalline solids are not directly usable here. Hence it is interesting to compare the properties of the amorphous and the crystalline state of the same compound to understand the relevance of long-range order. It is worthy to mention that crystallization results in the change of the thermal conductivity, which indicates that the amount of long-range order in material affects the transport properties. Moreover, considering that the amorphous and crystalline state of a solid tends to not dramatically alter its optical properties, it is quite interesting that phase change materials such as GeTe, GeSb<sub>2</sub>Te<sub>4</sub> or Ge<sub>2</sub>Sb<sub>2</sub>Te<sub>5</sub> show mainly different optical characteristics in both the amorphous and crystalline state. Wuttig et al. have reported these properties at [63]. Additionally, it was observable that the reflectance maxima of the crystalline film are smaller than 1, while the same value for the amorphous film is close to 1 [63], This is indicative of an absorption mechanism even below the band edge, like the free carrier absorption. Finally, the close spacing of the reflectance maxima in crystalline sample is due to the refractive index of the films. though, such a pronounced change of the refractive index has been observed for most of the phase change materials [64] The electronic polarizability describes the material's characteristic which allows it to change the charge carrier distribution by an external electromagnetic field. The large value of the electronic polarizability for crystalline phase change materials implies the presence of weakly bonded electrons, which are easily displaced by an external field. The formation of such explicit bonding can be further investigated from the atomic structure properties which we will discuss in the next subsection.

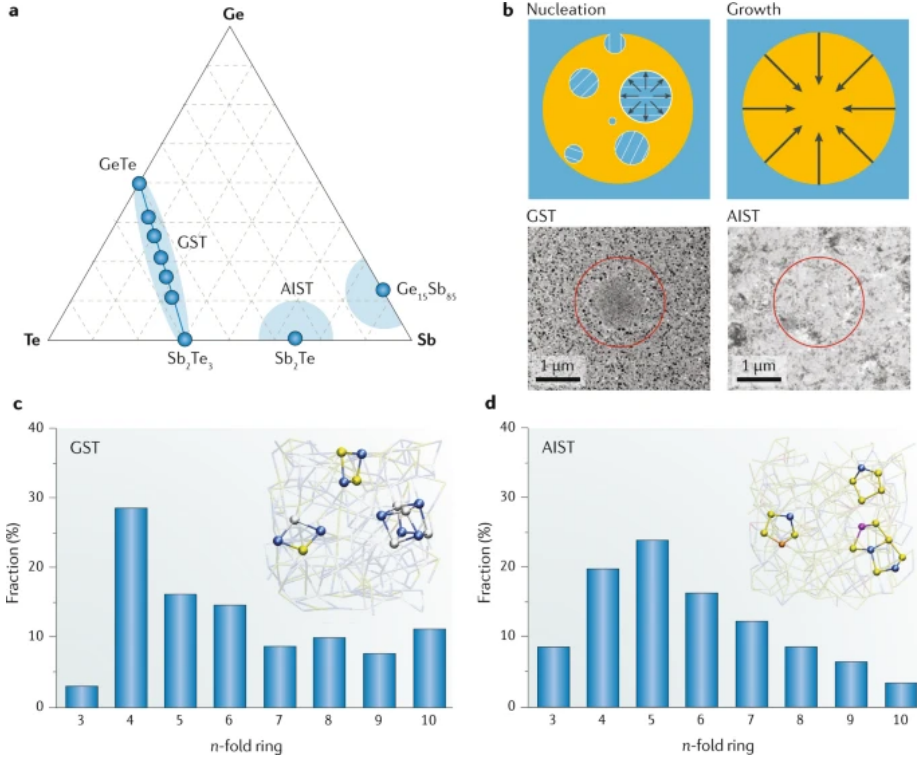


Figure 1.6: a) a treasure map for the phase change materials, b) The modes of crystallization in PCMs are either nucleation driven GST or AIST, The transmission electron microscope (TEM) images show the crystallized states upon heating (marked by the red circles). The TEM images show the outcome of a recrystallization experiment. The region marked by the red circles corresponds to the recrystallized PCM upon heating. In the case of GST, this region displays a clear contrast with its crystalline surrounding owing to the difference in grain size and orientation, showing that crystallization was driven by nucleation. By contrast, AIST exhibits no contrast, indicating a smooth crystal growth from the boundary, yielding a single-crystalline state. The distributions of primitive rings of different size in amorphous GST and AIST are shown in panels c and d. c) Fourfold primitive rings are the dominant structural fragments in amorphous GST. The inset shows an amorphous model of GST, with two ABAB squares and a cube A=Ge B=Sb,Te highlighted. d) In amorphous AIST, the distribution of primitive rings is broad, with fivefold primitive rings being the most abundant structural fragments. The inset shows an amorphous model of AIST, in which some fivefold primitive rings are highlighted. Ge, Sb, Te, Ag and In atoms are rendered in grey, yellow, blue, orange and purple, respectively. The TEM images in panel b are reproduced from [65]

### 1.3 Atomic Structure properties

From the atomic structure point of view, the main challenge is A substantial amount of research has been done on the structures of GST and the originating material GeTe in the amorphous phase. Previous investigations via X-ray absorption fine-structure spectroscopy revealed that most of the Ge atoms were tetrahedrally coordinated, and an umbrella flip model was suggested to explain the fast crystallization[66] But the ab-initio molecular dynamic (AIMD) calculations in the framework of density functional theory[67][68] yielded different results. They simulated amorphous models with only one third of Ge atoms in a tetrahedral structure. Thus, leaving a considerable proportion of Ge atoms in a defective octahedral structure[69][70] Moreover, the local energy and bonding analysis suggest that these tetrahedral Ge localities are locally stabilized due to the quenched-in homopolar Ge–Ge bonds[71] and will most likely disappear during the spontaneous structural relaxation of the glass[72][73] followed by a reinforced bond distortion. The proposed model satisfied the observations from X-ray absorption near-edge structure measurements[74] Additionally, the TEM measurements in conjunction with local reverse Monte Carlo simulations supports this. It should be noted that in these studies Ge atoms in amorphous GST belong to the octahedral local orders but with a more noticeable bond distortion than their crystalline phase[75] Additional studies of the short- and medium-range order of the amorphous network through structural analysis and rings topology[67][56] shed some light into the physics of crystallization in GST and AIST. In amorphous GST, fourfold primitive rings are the most abundant structural fragments (Figure 1.6.c), and more than 80% of these fourfold primitive rings have the form ABAB (A=Ge or Sb, B=Te), as supported by AIMD calculations[69][76]and reverse Monte Carlo simulations based on synchrotron-radiation X-ray diffraction data[77] These ABAB squares are the smallest structural units in rock-salt GST, Moreover, two ABAB local orders can merge to form a cube (Figure 1.6.c, inset) [78]. Therefore, key structures for fast nucleation in GST[76][77] originates from these square. On the other hand, the calculations on the amorphous phase of  $\text{Ag}_4\text{In}_3\text{Sb}_6\text{Te}_{26}$  (AIST) indicates a wider distribution of rings from 3-fold to 7-fold while the 5-fold rings taking up the majority of rings (Figure 1.6.d). These findings suggest that the structural features are different from the octahedral-like coordination in crystalline AIST.

### 1.4 Molecular dynamics simulations and its challenges

Aside from the properties and predictions which were extracted from AIMD simulations, some challenging steps are still standing. Namely, a considerable amount of crystal growth rate deviation of atomic diffusivity of  $\text{Ag}_4\text{In}_3\text{Sb}_6\text{Te}_{26}$  in between the experiments and calculations are observed at  $< 500\text{K}$ . The problem arises from the fact that in the simulations a fast-cooling effect is applied, but further study is required. Additionally, the definition of the size of the critical nuclei which is a function of temperature is still needed. Current

molecular dynamics simulations lack the incomplete statistical sampling. A full characterization of memory cells demands simulations with substantial time and length scales to be performed. Moreover, the existence of interfacing materials such as substrates with the PCM should be thoroughly considered as such interfaces can lead to significant modifications of the activation energy of the crystallization.

## 1.5 Thesis outline

The work presented in this study is organized as follows: In the methodology section, we describe the frameworks in which the studies were carried out. Then in the Chapter 3, we investigate the material and defect characteristics of La<sub>2</sub>O<sub>3</sub> and CeO<sub>2</sub> high-k dielectric materials as potential candidates for resistive random-access memories and gate materials for MOSFETs. Chapter 4 introduces the python script-tool “Bond Element Lattice Locality Order (BELLO)” which was developed for automatic analysis of the local-order-related statistics of amorphous materials. After that, chapter 5 presents our findings regarding the hierarchical short- and medium-range order structures in amorphous Ge<sub>x</sub>Se<sub>1-x</sub> used in selectors which took advantage of BELLO’s capabilities. Finally, in chapter 6, we present our studies on the memory switching effects of As<sub>2</sub>Se<sub>3</sub> doping in GeTe<sub>4</sub> for selectors applications. We investigated the electronic properties in the framework of density functional theory coupled with Carr-Parrinello simulations and the structural analysis via BELLO tool. Our findings has set the route for better understanding the switching behaviour in chalcogenide glasses.

## References

- [1] Von Neumann, J. and Godfrey, M. D. “First Draft of a Report on the EDVAC”. English. In: *IEEE Annals of the History of Computing* vol. 15, no. 4 (1993). Cited By :207, pp. 27–75.
- [2] Burr, G. W. et al. “Neuromorphic computing using non-volatile memory”. English. In: *Advances in Physics: X* vol. 2, no. 1 (2017). Cited By :399, pp. 89–124.
- [3] Versace, M. and Chandler, B. “The brain of a new machine”. English. In: *IEEE Spectrum* vol. 47, no. 12 (2010). Cited By :65, pp. 30–37.
- [4] Upadhyay, N. K., Joshi, S., and Yang, J. J. “Synaptic electronics and neuromorphic computing”. English. In: *Science China Information Sciences* vol. 59, no. 6 (2016). Cited By :38.
- [5] Ananthanarayanan, R. et al. “The cat is out of the bag: Cortical simulations with 109 neurons, 1013 synapses”. English. In: *Proceedings of the Conference on High Performance Computing Networking, Storage and Analysis, SC '09*. Cited By :180. 2009.

- [6] Ananthanarayanan, R. and Modha, D. S. “Anatomy of a cortical simulator”. English. In: *Proceedings of the 2007 ACM/IEEE Conference on Supercomputing, SC’07*. Cited By :64. 2007.
- [7] Mead, C. “Neuromorphic Electronic Systems”. English. In: *Proceedings of the IEEE* vol. 78, no. 10 (1990). Cited By :905, pp. 1629–1636.
- [8] Djurfeldt, M. et al. “Brain-scale simulation of the neocortex on the IBM Blue Gene/L supercomputer”. English. In: *IBM Journal of Research and Development* vol. 52, no. 1-2 (2008). Cited By :77, pp. 31–42.
- [9] Izhikevich, E. M. and Edelman, G. M. “Large-scale model of mammalian thalamocortical systems”. English. In: *Proceedings of the National Academy of Sciences of the United States of America* vol. 105, no. 9 (2008). Cited By :622, pp. 3593–3598.
- [10] Scott, J. F. and Paz De Araujo, C. A. “Ferroelectric memories”. English. In: *Science* vol. 246, no. 4936 (1989). Cited By :3405, pp. 1400–1405.
- [11] Ishiwara, H. “Impurity substitution effects in BiFeO<sub>3</sub> thin films - From a viewpoint of FeRAM applications”. English. In: *Current Applied Physics* vol. 12, no. 3 (2012). Cited By :46, pp. 603–611.
- [12] Prejbeanu, I. L. et al. “Thermally assisted MRAMs: Ultimate scalability and logic functionalities”. English. In: *Journal of Physics D: Applied Physics* vol. 46, no. 8 (2013). Cited By :77.
- [13] Chen, E. et al. “Progress and prospects of spin transfer torque random access memory”. English. In: *IEEE Transactions on Magnetics* vol. 48, no. 11 (2012). Cited By :27, pp. 3025–3030.
- [14] Wong, H. - P. et al. “Phase change memory”. English. In: *Proceedings of the IEEE* vol. 98, no. 12 (2010). Cited By :1042, pp. 2201–2227.
- [15] Burr, G. W. et al. “Phase change memory technology”. English. In: *Journal of Vacuum Science and Technology B: Nanotechnology and Microelectronics* vol. 28, no. 2 (2010). Cited By :656, pp. 223–262.
- [16] Jeong, D. S. et al. “Emerging memories: Resistive switching mechanisms and current status”. English. In: *Reports on Progress in Physics* vol. 75, no. 7 (2012). Cited By :657.
- [17] Wouters, D. J., Waser, R., and Wuttig, M. “Phase-Change and Redox-Based Resistive Switching Memories”. English. In: *Proceedings of the IEEE* vol. 103, no. 8 (2015). Cited By :94, pp. 1274–1288.
- [18] Chua, L. O. “Memristor—The Missing Circuit Element”. English. In: *IEEE Transactions on Circuit Theory* vol. 18, no. 5 (1971). Cited By :5088, pp. 507–519.
- [19] Strukov, D. B. et al. “The missing memristor found”. English. In: *Nature* vol. 453, no. 7191 (2008). Cited By :6410, pp. 80–83.
- [20] Yang, J. J. et al. “Memristive switching mechanism for metal/oxide/metal nanodevices”. English. In: *Nature Nanotechnology* vol. 3, no. 7 (2008). Cited By :2120, pp. 429–433.

- [21] Choi, H. et al. “An electrically modifiable synapse array of resistive switching memory”. English. In: *Nanotechnology* vol. 20, no. 34 (2009). Cited By :109.
- [22] Wu, Y. et al. “AlOx-based resistive switching device with gradual resistance modulation for neuromorphic device application”. English. In: *2012 4th IEEE International Memory Workshop, IMW 2012*. Cited By :31. 2012.
- [23] Hasegawa, T. et al. “Learning abilities achieved by a single solid-state atomic switch”. English. In: *Advanced Materials* vol. 22, no. 16 (2010). Cited By :216, pp. 1831–1834.
- [24] Jo, S. H. et al. “Nanoscale memristor device as synapse in neuromorphic systems”. English. In: *Nano Letters* vol. 10, no. 4 (2010). Cited By :2323, pp. 1297–1301.
- [25] Gacem, K. et al. “Neuromorphic function learning with carbon nanotube based synapses”. English. In: *Nanotechnology* vol. 24, no. 38 (2013). Cited By :28.
- [26] Shen, A. M. et al. “Analog neuromorphic module based on carbon nanotube synapses”. English. In: *ACS Nano* vol. 7, no. 7 (2013). Cited By :53, pp. 6117–6122.
- [27] Scott, J. C. and Bozano, L. D. “Nonvolatile memory elements based on organic materials”. English. In: *Advanced Materials* vol. 19, no. 11 (2007). Cited By :864, pp. 1452–1463.
- [28] Tour, J. M. et al. “Nanocell logic gates for molecular computing”. English. In: *IEEE Transactions on Nanotechnology* vol. 1, no. 2 (2002). Cited By :119, pp. 100–108.
- [29] Zhang, D. et al. “All Spin Artificial Neural Networks Based on Compound Spintronic Synapse and Neuron”. English. In: *IEEE Transactions on Biomedical Circuits and Systems* vol. 10, no. 4 (2016). Cited By :46, pp. 828–836.
- [30] Sengupta, A. et al. “Spin-orbit torque induced spike-timing dependent plasticity”. English. In: *Applied Physics Letters* vol. 106, no. 9 (2015). Cited By :59.
- [31] Kuzum, D., Yu, S., and Philip Wong, H. -. “Synaptic electronics: Materials, devices and applications”. English. In: *Nanotechnology* vol. 24, no. 38 (2013). Cited By :603.
- [32] Yamada, N. et al. “Rapid-phase transitions of GeTe-Sb<sub>2</sub>Te<sub>3</sub> pseudobinary amorphous thin films for an optical disk memory”. English. In: *Journal of Applied Physics* vol. 69, no. 5 (1991). Cited By :1169, pp. 2849–2856.
- [33] Rios, C. et al. “Integrated all-photonics non-volatile multi-level memory”. English. In: *Nature Photonics* vol. 9, no. 11 (2015). Cited By :403, pp. 725–732.



- [34] Burr, G. W. et al. “Recent Progress in Phase-Change Memory Technology”. English. In: *IEEE Journal on Emerging and Selected Topics in Circuits and Systems* vol. 6, no. 2 (2016). Cited By :176, pp. 146–162.
- [35] Meena, J. S. et al. “Overview of emerging nonvolatile memory technologies”. English. In: *Nanoscale Research Letters* vol. 9, no. 1 (2014). Cited By :331, pp. 1–33.
- [36] Cai, Yu et al. “Neighbor-cell assisted error correction for MLC NAND flash memories”. In: *ACM SIGMETRICS Performance Evaluation Review* vol. 42, no. 1 (June 2014), pp. 491–504. DOI: [10.1145/2637364.2591994](https://doi.org/10.1145/2637364.2591994).
- [37] Park, Ki-Tae et al. “Three-Dimensional 128 Gb MLC Vertical nand Flash Memory With 24-WL Stacked Layers and 50 MB/s High-Speed Programming”. In: *IEEE Journal of Solid-State Circuits* vol. 50, no. 1 (Jan. 2015), pp. 204–213. DOI: [10.1109/jssc.2014.2352293](https://doi.org/10.1109/jssc.2014.2352293).
- [38] Cai, Yu et al. “Threshold Voltage Distribution in MLC NAND Flash Memory: Characterization, Analysis and Modeling”. In: *Design, Automation & Test in Europe Conference & Exhibition (DATE), 2013*. IEEE Conference Publications, 2013. DOI: [10.7873/date.2013.266](https://doi.org/10.7873/date.2013.266).
- [39] Lee, M. -. et al. “2-Stack ID-IR cross-point structure with oxide diodes as switch elements for high density resistance RAM applications”. English. In: *Technical Digest - International Electron Devices Meeting, IEDM*. Cited By :228. 2007, pp. 771–774.
- [40] Chen, A. “A comprehensive crossbar array model with solutions for line resistance and nonlinear device characteristics”. English. In: *IEEE Transactions on Electron Devices* vol. 60, no. 4 (2013). Cited By :106, pp. 1318–1326.
- [41] Yasuda, S. et al. “A cross point Cu-ReRAM with a novel OTS selector for storage class memory applications”. English. In: *Digest of Technical Papers - Symposium on VLSI Technology*. Cited By :15. 2017, T30–T31.
- [42] Sasago, Y. et al. “Cross-point phase change memory with 4F2 cell size driven by low-contact-resistivity poly-Si diode”. English. In: *Digest of Technical Papers - Symposium on VLSI Technology*. Cited By :116. 2009, pp. 24–25.
- [43] Shenoy, R. S. et al. “Endurance and scaling trends of novel access-devices for multi-layer crosspoint-memory based on mixed-ionic-electronic-conduction (MIEC) materials”. English. In: *Digest of Technical Papers - Symposium on VLSI Technology*. Cited By :23. 2011, pp. 94–95.
- [44] Goodwin, W. E. P. In: (1954). Cited By :1.
- [45] Liu, G. et al. “Increasing Trapped Carrier Density in Nanoscale GeSeAs Films by As Ion Implantation for Selector Devices in 3D-Stacking Memory”. English. In: *ACS Applied Nano Materials* vol. 2, no. 9 (2019). Cited By :3, pp. 5373–5380.

- [46] Sun, Y. et al. “Short-Term and Long-Term Plasticity Mimicked in Low-Voltage Ag/GeSe/TiN Electronic Synapse”. English. In: *IEEE Electron Device Letters* vol. 39, no. 4 (2018). Cited By :30, pp. 492–495.
- [47] Yoo, S. et al. “Chemical interactions in the atomic layer deposition of Ge-Sb-Se-Te films and their ovonic threshold switching behavior”. English. In: *Journal of Materials Chemistry C* vol. 6, no. 18 (2018). Cited By :15, pp. 5025–5032.
- [48] Song, B. et al. “An ovonic threshold switching selector based on Se-rich GeSe chalcogenide”. English. In: *Applied Physics A: Materials Science and Processing* vol. 125, no. 11 (2019). Cited By :7.
- [49] Kim, S. -. et al. “Effect of Ge concentration in GeXse1-x chalcogenide glass on the electronic structures and the characteristics of ovonic threshold switching (OTS) devices”. English. In: *ECS Solid State Letters* vol. 2, no. 10 (2013). Cited By :23, Q75–Q77.
- [50] Shin, S. -. et al. “The effect of doping Sb on the electronic structure and the device characteristics of Ovonic Threshold Switches based on Ge-Se”. English. In: *Scientific Reports* vol. 4 (2014). Cited By :32.
- [51] Chai, Z. et al. “Dependence of Switching Probability on Operation Conditions in GexSe1-x Ovonic Threshold Switching Selectors”. English. In: *IEEE Electron Device Letters* vol. 40, no. 8 (2019). Cited By :6, pp. 1269–1272.
- [52] Bezanilla, F. “Voltage-gated ion channels”. In: *IEEE Transactions on Nanobioscience* vol. 4, no. 1 (2005). Cited By :91, pp. 34–48.
- [53] Ambrogio, S. et al. “Unsupervised learning by spike timing dependent plasticity in phase change memory (PCM) synapses”. In: *Frontiers in Neuroscience* vol. 10, no. MAR (2016). Cited By :88.
- [54] Suri, M. et al. “Physical aspects of low power synapses based on phase change memory devices”. In: *Journal of Applied Physics* vol. 112, no. 5 (2012). Cited By :81.
- [55] Pernice, W. H. P. and Bhaskaran, H. “Photonic non-volatile memories using phase change materials”. In: *Applied Physics Letters* vol. 101, no. 17 (2012). Cited By :79.
- [56] Kim, S. et al. “NVM neuromorphic core with 64k-cell (256-by-256) phase change memory synaptic array with on-chip neuron circuits for continuous in-situ learning”. In: *Technical Digest - International Electron Devices Meeting, IEDM*. Vol. 2016-February. Cited By :77. 2015, pp. 17.1.1–17.1.4.
- [57] Prejbeanu, I. L. et al. “Thermally assisted MRAMs: Ultimate scalability and logic functionalities”. In: *Journal of Physics D: Applied Physics* vol. 46, no. 8 (2013). Cited By :77.
- [58] Djurfeldt, M. et al. “Brain-scale simulation of the neocortex on the IBM Blue Gene/L supercomputer”. In: *IBM Journal of Research and Development* vol. 52, no. 1-2 (2008). Cited By :77, pp. 31–42.

- [59] Lai, S. and Lowrey, T. “OUM - A 180 nm nonvolatile memory cell element technology for stand alone and embedded applications”. In: *IEDM Tech.Dig.* (2001). Cited By :75, pp. 3651–3654.
- [60] Wankerl, K. et al. “L-type voltage-gated Ca<sup>2+</sup> channels: A single molecular switch for long-term potentiation/long-term depression-like plasticity and activity-dependent metaplasticity in humans”. In: *Journal of Neuroscience* vol. 30, no. 18 (2010). Cited By :74, pp. 6197–6204.
- [61] Stegmaier, M. et al. “Nonvolatile All-Optical 1 × 2 Switch for Chipscale Photonic Networks”. In: *Advanced Optical Materials* vol. 5, no. 1 (2017). Cited By :72.
- [62] Versace, M. and Chandler, B. “The brain of a new machine”. In: *IEEE Spectrum* vol. 47, no. 12 (2010). Cited By :65, pp. 30–37.
- [63] Wuttig, Matthias and Raoux, Simone. “The science and technology of phase change materials”. In: *Zeitschrift für anorganische und allgemeine Chemie* vol. 638, no. 15 (2012), pp. 2455–2465.
- [64] Shportko, Kostiantyn et al. “Resonant bonding in crystalline phase-change materials”. In: *Nature materials* vol. 7, no. 8 (2008), pp. 653–658.
- [65] Wang, M. et al. “Robust memristors based on layered two-dimensional materials”. In: *Nature Electronics* vol. 1, no. 2 (2018). Cited By :181, pp. 130–136.
- [66] Yamada, N. et al. “Rapid-phase transitions of GeTe-Sb<sub>2</sub>Te<sub>3</sub> pseudobinary amorphous thin films for an optical disk memory”. In: *Journal of Applied Physics* vol. 69, no. 5 (1991). Cited By :1169, pp. 2849–2856.
- [67] Boybat, I. et al. “Neuromorphic computing with multi-memristive synapses”. In: *Nature Communications* vol. 9, no. 1 (2018). Cited By :165.
- [68] Singh, S., Ediger, M. D., and De Pablo, J. J. “Ultrastable glasses from in silico vapour deposition”. In: *Nature Materials* vol. 12, no. 2 (2013). Cited By :160, pp. 139–144.
- [69] Rupp, M. “Machine learning for quantum mechanics in a nutshell”. In: *International Journal of Quantum Chemistry* vol. 115, no. 16 (2015). Cited By :153, pp. 1058–1073.
- [70] Zhu, M. et al. “One order of magnitude faster phase change at reduced power in Ti-Sb-Te”. In: *Nature Communications* vol. 5 (2014). Cited By :141.
- [71] Cheng, Z. et al. “On-chip photonic synapse”. In: *Science Advances* vol. 3, no. 9 (2017). Cited By :138.
- [72] Kent, A. D. and Worledge, D. C. “A new spin on magnetic memories”. In: *Nature Nanotechnology* vol. 10, no. 3 (2015). Cited By :385, pp. 187–191.
- [73] Zidan, M. A., Strachan, J. P., and Lu, W. D. “The future of electronics based on memristive systems”. In: *Nature Electronics* vol. 1, no. 1 (2018). Cited By :375, pp. 22–29.

- [74] Kim, I. S. et al. “High performance PRAM cell scalable to sub-20nm technology with below 4F<sup>2</sup> cell size, extendable to DRAM applications”. In: *Digest of Technical Papers - Symposium on VLSI Technology*. Cited By :136. 2010, pp. 203–204.
- [75] Liu, C. et al. “A semi-floating gate memory based on van der Waals heterostructures for quasi-non-volatile applications”. In: *Nature Nanotechnology* vol. 13, no. 5 (2018). Cited By :133, pp. 404–410.
- [76] Kim, K. et al. “A carbon nanotube synapse with dynamic logic and learning”. In: *Advanced Materials* vol. 25, no. 12 (2013). Cited By :152, pp. 1693–1698.
- [77] Sebastian, A., Le Gallo, M., and Krebs, D. “Crystal growth within a phase change memory cell”. In: *Nature Communications* vol. 5 (2014). Cited By :129.
- [78] Zhang, Wei et al. “Designing crystallization in phase-change materials for universal memory and neuro-inspired computing”. In: *Nature Reviews Materials* vol. 4, no. 3 (2019), pp. 150–168.

# Chapter 2

## Methodology

### 2.1 Multiscale Modeling Simulations

#### 2.1.1 Introduction

Semiconductor device simulations are becoming increasingly complex because of the continuous size shrinking, the adoption of complex 3D geometries, the introduction of new materials and the integration in the Back End of Line (BEOL). These fundamental changes complicate severely the technology development due to:

- **new physical phenomena**, either detrimental for device reliability, or purposely exploited for device operation (for example ion migration, phase change, ferroelectricity, ...);
- **new active materials** like oxides, chalcogenides and ferroelectrics;
- **atomic level defects and interface material properties**, critically affecting device performance and determining statistics and device reliability.

In this scenario, new simulation tools are needed, leveraging the material-device connectivity and going beyond the semiconductor physics. Ginestra(R), a novel multi-physics, multi-scale Material-Device Simulation Platform, allows to address all the above issues, establishing a functional link between material properties (either calculated using DFT or extracted from electrical measurements) and device electrical performances. Ginestra(R) allows exploring the material/defect effects on the device electrical performance, including reliability (e.g. retention and endurance), noise, DC/AC/pulsed-regime performances and statistics, with a focus on emerging technologies (RRAM, CBRAM, PCM, OTS, Ferro). Material properties (including defects) can be obtained from DFT calculations, extracted from electrical measurements through automatic routines, or simply taken from the Ginestra(R)Material Library. Ginestra(R) drives the acceleration of the technology development through ad-hoc tools supporting:

- **learning**: defect spectroscopy and parameter extraction allow to extract material/ defect properties from multiple electrical measurements, supporting process monitor/improvement;
- **exploration**: parametric simulations allow to investigate how material/geometry/ process variations affect the device electrical performances including reliability and variability;
- **material/device design and optimization**: virtual Design of Experiments (DoE) allows for material screening and performance optimization.

Ginestra(R) relies on a kinetic Monte-Carlo engine and a solid physical description of trap-carriers interaction and of the most relevant charge-transport and material modifications mechanisms occurring during device operation and degradation/ aging. Both conventional (FinFET, DRAM, 3D NAND) and

emerging technologies (RRAM, CBRAM, PCM, Ferro, OTS) can be considered. Charge trapping and transport (dominated by trap-assisted contributions) are self-consistently modeled by accounting for power dissipation and temperature increase, and a variety of material changes such as bond breakage and restoration, redox, drift and diffusion of atomic species, phase changes are included.

## 2.1.2 Physics

This chapter provides a comprehensive overview of the physics in Ginestra(R).

### 2.1.2.1 Potential and Electric Field

The electric potential  $\phi(x; y; z)$  within the semiconductor device is calculated by solving the Poisson's equation. It correlates the electric potential and field to a given charge density distribution in a certain space while accounting for the different charges that may be present (e.g. electron and hole carriers, fixed and mobile charges)

$$\nabla(\epsilon_0\epsilon_r\nabla\phi(x, y, z) + P_{FE}(x, y, z)) = -q(p - n + N_D - N_A) - \rho_{fixed} - \rho_{ions} - \rho_{traps} \quad (2.1)$$

Where:

$\epsilon_0$  is the vacuum permittivity

$\epsilon_r$  is the relative permittivity of the material

$P_{FE}$  is the ferroelectric polarization

$q$  is the elementary electron charge

$p$  and  $n$  are the hole and electron densities, respectively

$N_D$  and  $N_A$  are the ionized acceptor and donor concentrations

$\rho_{fixed}$  is the charge density due to the fixed charges

$\rho_{ions}$  is the charge density due to mobile ion charges

$\rho_{traps}$  is the charge density due to traps (determined by the defects initial charge state and the charge trapped at the defect)

### 2.1.2.2 Electrical Boundary Conditions

The solution of the Poisson's equation requires to use proper electrical boundary conditions at the electrodes. These conditions are applied based on the type of the material in simulation.

**Metal.** If the material in use is a metal the Dirichlet conditions apply and the potential is determined by the applied voltage  $V$  and the work function difference between the electrodes  $\phi_{MS}$ :  $\phi = V - \phi_{MS}$ .

**Semiconductor.** for the case of semiconductors, the electrode is defined as a semiconductor. Dirichlet conditions apply and the potential is determined by the applied voltage  $V$  and the work function difference between the electrodes  $\phi_{MS}$  and the surface potential  $\psi_S$ :  $\phi = V - \phi_{MS} - \psi_S$ . The latter is calculated differently depending on whether the quantization effects are considered or

not. When the quantization effects at the semiconductor interface are not taken into account, the surface potential  $\psi_S$  is calculated iteratively from the solution of the equation giving the total charge per unit area  $Q_S$  in the semiconductor:

$$Q_S(\psi_S) = \frac{1}{A} \iint D \cdot n = \frac{1}{A} (\epsilon_0 \epsilon_r \nabla \phi + P_{FE}) \cdot n \quad (2.2)$$

Where:

A is the semiconductor area

D is the electric displacement field

n is the normal vector

The carriers density used to calculate  $Q_S$  in the solution above is determined using either the Maxwell-Boltzmann:

$$f(E) = \frac{1}{\exp\left(\frac{E-E_F}{k_B T}\right)} \quad (2.3)$$

or the Fermi-Dirac distributions function:

$$f(E) = \frac{1}{1 + \exp\left(\frac{E-E_F}{k_B T}\right)} \quad (2.4)$$

where E is the carrier energy,  $E_F$  is the Fermi energy level,  $k_B$  is the Boltzmann's constant and T is the temperature.

### 2.1.2.3 Dielectric Permittivity Model

In GINESTRA(R) the permittivity of a material is generally considered to be isotropic and constant. The value of the static dielectric permittivity can be defined in the software. In the case of AC simulations, the permittivity can be considered to depend on the electric field (as expected in some dielectrics, such as SrTiO<sub>3</sub>) through the Johnson's model:

$$\epsilon_r(F) = \frac{\epsilon_r(0)}{1 + \left(\frac{F}{F_C}\right)^2} \quad (2.5)$$

where F is the electric field,  $\epsilon_r(0)$  the static dielectric permittivity at zero field, and  $F_C$  is the critical value of the electric field (in MV/cm) at which the dynamic dielectric constant is half of  $\epsilon_r(0)$ . The Johnson's model can be manually activated. The Johnson's model is considered only in AC simulations. In transient simulations  $\epsilon_r$  can be considered to be dependent on material stoichiometry (i.e. on the density of defects). This is important to accurately calculate the local permittivity during degradation (e.g. dielectric breakdown) and RRAM simulations. In this types of simulation, a large amount of defects (e.g. oxygen vacancies) is expected to be generated under the applied electrical stress. This determines a (usually local) transformation of the material from its initial state (e.g. oxide) to a different one (e.g. metal-like) that is accompanied by a change (increase) of the material permittivity. This effect is relevant also to account for the redistribution of the electric

led that occurs between pristine and highly degraded regions (or layers in multi-layer structures). Dielectric constant changes with material stoichiometry (i.e. defect density) are managed internally by Ginestra(R) through the following functional relation:

$$\epsilon_r = \frac{\epsilon_{r,2} \cdot \epsilon_{r,1}}{\epsilon_{r,1} - (\epsilon_{r,2} - \epsilon_{r,1}) \exp -SF \cdot (\frac{N_T}{N_C - N_T})} \quad (2.6)$$

Where:

$\epsilon_{r,1}$  is the relative permittivity of the initial material state (e.g. oxide)

$\epsilon_{r,2} = 300$  is the relative permittivity of the highly sub-stoichiometric state (e.g. metal-like)

$N_T$  is the local defect density (depends on x, y, z position)

$N_C = 10^{28}$  is the critical defect density (in  $m^{-3}$ )

SF = 1 is the shape factor

Above equation is calculated as a function of spatial position (x, y, z) in the whole material volume, allowing accounting for local variations of the relative permittivity.

## 2.1.3 Carriers Transport Mechanisms

Figure 2.1 shows a schematic representation on a device band diagram of the carriers transport mechanisms that are considered in simulations. a more detailed description of the transport mechanisms are available at [1]. In this section we will explain the Trap-assisted-tunneling mechanism in detail since the majority of the simulations govern this transport phenomena.

### 2.1.3.1 Defect-Assisted Mechanisms: Trap-Assisted Tunneling

One of the most relevant carrier transport mechanisms (especially in oxides) is the one assisted by defects. In Ginestra(R) the defect-assisted carriers transport is described through the quantum-mechanical multi-phonon trap-assisted-tunneling (TAT) theory that includes the electron phonon coupling and lattice relaxation [2] [3] [4]. The model is described here with reference to electron transport and considering standard bi-state defects, although Ginestra(R) fully supports also multi-state and metastable defects. the total rate associated to a given trap j is calculated by solving the trap's charge balance equation that in transient regime can be written as:

$$\frac{dF_j}{dt} = R_j^{in}(t) \cdot (1 - F_j(t)) - R_j^{out}(t) \cdot F_j(t) \quad (2.7)$$

where  $R_j^{in}$  and  $R_j^{out}$  are the input and output rates to and from the j-th trap, respectively. They are calculated considering every possible charge transition, illustrated in figure 2.2.

$$R_j^{in}(t) = R_j^{in,el} + \sum F_k(t) \cdot R_{kj}^{TT} + \int dr R_j^{in,TTB} \quad (2.8)$$



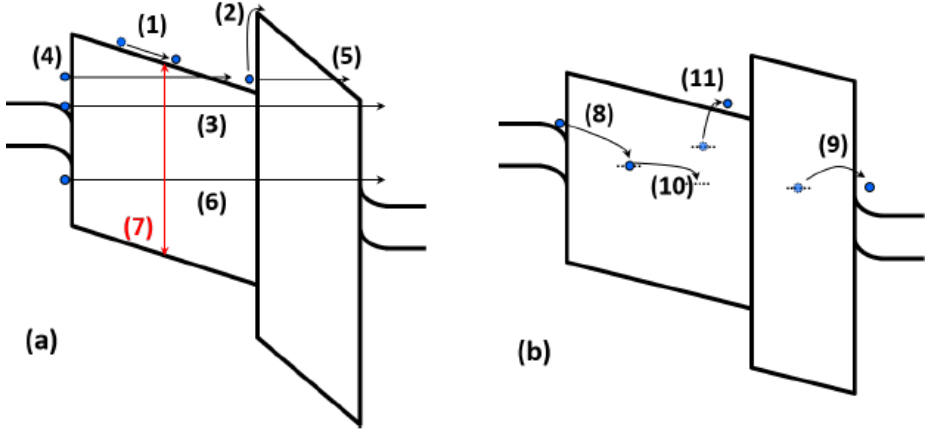


Figure 2.1: Schematic representation of the different carriers transport mechanisms considered in Ginestra(R): (a) tunneling and others; (b) trap-assisted. The mechanisms are numbered as follows: (1) drift-diffusion; (2) thermionic emission; (3) direct tunneling; (4) electrode-band tunneling; (5) intra-band tunneling; (6) band-to-band tunneling; (7) local generation-recombination; (8) electrode-to-trap capture,  $R^{in,el}$ ; (9) trap-to-electrode emission  $R^{out,elg}$ ; (10) trap-to-trap transition,  $R^{TT}$ ; (11) trap-to-band transition,  $R^{TTB}$ . The mechanisms are shown for the case of electron transport, but the same holds for holes transport.

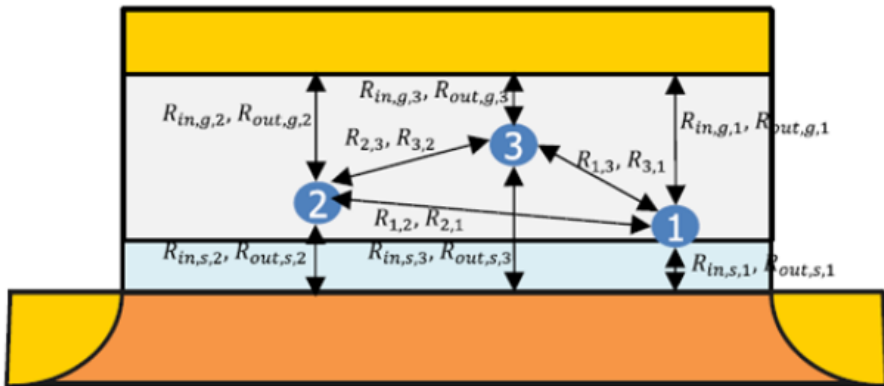


Figure 2.2: Schematic representation of the transition rates considered in the calculation of  $R_{in,j}$  and  $R_{out,j}$  in equation below for a simple case of three traps

$$R_j^{out}(t) = R_j^{out,el} + \sum R_{kj}^{TT} \cdot (1 - F_k(t)) + \int dr R_j^{out,TTB} \quad (2.9)$$

where:

$N_T$  is the total number of traps

$R_j^{in,el}$  is the transition (capture) rate between the j-th trap and the electrodes, see mechanism (8) in Fig. 2.1

$R_j^{out,el}$  is the transition (emission) rate between the j-th trap and the electrodes, see mechanism (9) in Fig. 2.1.

$R_{kj}^{TT}$  is the transition rate from the k-th (j-th) trap to the j-th (k-th) trap, see mechanism (10) in Fig. 2.1.

$R_j^{in,TTB}(R_j^{out,TTB})$  is the rate from the band (trap) to the trap (band), see mechanism (11) in Fig. 2.1.

The transition rates in both equations above are all calculated in the framework of the multi-phonon TAT theory, with some small differences related to the starting and arrival point (i.e. electrode, band, trap). The model considers carriers coupling to the oxide phonons, which are assumed to be of a single frequency  $\omega_0$ . The rates associated with the carrier transport via the j-th trap are calculated by summing the contributions  $R_{j,m}^{in}$  and  $R_{j,n}^{out}$  associated to the discretized phonon energies (indexes m and n):

$$R_j^{in} = \sum R_{j,m}^{in} \quad (2.10)$$

$$R_j^{out} = \sum R_{j,n}^{out} \quad (2.11)$$

As shown in Figure 2.3 (for the case of electron TAT capture/emission process

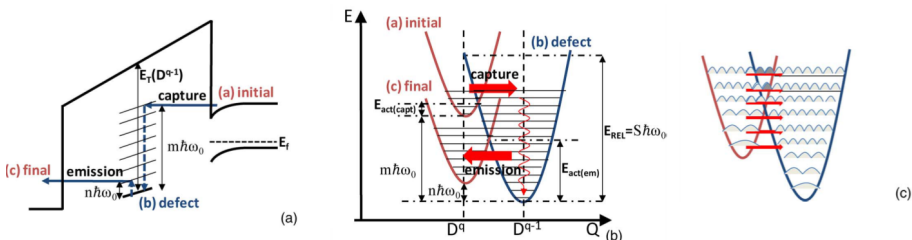


Figure 2.3: (a) Band diagram illustrating an example of multi-phonon capture and emission processes in the case of a single-trap conductive path. A monolayer stack has been considered for simplicity. (b) Full energy configuration coordination diagram corresponding to the processes. (c) Representation of the possible transitions between the different resonant vibrational eigenfunctions

from a semiconductor conduction band to a metal electrode),  $R_{j,m}^{in}$  is the time required for the carrier capture into the j-th trap, which is associated with the release of the carrier energy  $m\hbar\omega_0$  to the lattice, with m being the number of phonons involved.  $R_{j,n}^{out}$  is the time required for the carrier emission from the j-th trap, which is associated to the absorption of the carrier

energy  $n\hbar\omega_0$  from the lattice, with n being the number of phonons involved [2] [3]:

$$R_{j,m}^{in} = N_{j-1}(E_{j,m})f_{j-1}(E_{j,m})Ca_{j,m}P_T(E_{j-1}, E_{j,m}) \quad (2.12)$$

$$R_{j,n}^{out} = N_{j+1}(E_{j,m})[1 - f_{j+1}(E_{j,n})]Em_{j,n}P_T(E_{j,n}, E_{j+1},) \quad (2.13)$$

$$E_{j,l} = E_j + l\hbar\omega_0 \quad (2.14)$$

where:

$E_j$  is the absolute energy of the j-th trap

$N_j$  and  $f_j$  are the density of states and the Fermi-Dirac occupation probability at the cathode ( $j = 0$ ), in the trap states ( $1 \leq j \leq Nt$ ) or at the anode ( $j = Nt + 1$ )

$P_T$  is the tunneling probability

$Ca_{j,m}$  is the carrier multi-phonon capture rate

$Em_{j,n}$  is the carrier multi-phonon emission rate

The capture and emission rates in these equations are calculated in the framework of the multi-phonon theory accounting for the carrier-phonon interactions where the emission rate peaks at  $n=0$  and decreases exponentially with n, thus indicating that the electrons are typically emitted from the trap state with minimal phonon absorption [5].  $c_0$  is the field-independent constant associated to the non-adiabatic transitions [6]:

$$c_0 = \frac{5\pi^2(S\hbar\omega_0)^2r_t^3}{\hbar} \quad (2.15)$$

and L is the multi-phonon transition probability that accounts for the carrier phonon coupling:

$$L(m) = \left(\frac{f_B + 1}{f_B}\right)^{\frac{m}{2}} \exp -S(2f_B + 1)I_m(2S\sqrt{f_B(f_B + 1)}) \quad (2.16)$$

where  $f_B$  is the Bose function providing the phonon occupation number:

$$f_B = \frac{1}{\exp \frac{\hbar\omega_0}{K_B T} - 1} \quad (2.17)$$

where:

$r_t$  is the capture radius (in meters) with  $\sigma_t$  being the capture cross-section of the defect

$I_m$  is the modified Bessel function of order m [4]

S is the Huang-Rhys factor [3] [4], representing the number of phonons required for the atomic-scale lattice rearrangement around the defect that is required to accommodate the trapped charge [2]. According to Fermi's golden rule, the transition probability L(m) between two defect charge states is calculated by summing the transition probabilities between the different resonant vibrational eigenfunctions, which are proportional to their overlap integrals. Therefore, in order to obtain an optimal overlap, the system needs to surmount a thermal activation barrier  $E_{act(capt)}, E_{act(em)}$  that plays a fundamental role in setting the T dependence of the process. Though, the transition can also occur between two

vibrational states that are below the barrier due to the non-null overlap between the exponential tails of two vibrational wavefunctions in the classically forbidden region. Such process, named nuclear tunneling, is a known phenomenon in the electron transfer reactions and becomes dominant at cryogenic temperatures. The transition probability  $L$  which was described in above equation takes into account all the contributions by summing the overlap integrals calculated for all the resonant states of the initial and final vibrational configurations [2] [3].

## 2.2 Density Functional Theory

In this section a description of the Density-Functional Theory is presented covering the general equations governing the approach followed by the description of the molecular dynamic method employed in the third paper. A more in-depth description of the exact parameters used in each simulation are available in the corresponding paper section.

In the late 1920s Fermi and Thomas [7][8] proposed a methodology which was based on the electron density, by utilizing the energy functional for a non-interacting electron gas via uniform density. Then in the 1964, Hohenberg and Kohn [9] introduced a revolutionary scheme which set the foundation of density-functional theory as it is used to this day.

### 2.2.1 Hohenberg and Kohn Theorem

Hohenberg and Kohn [9] introduced two theorems setting the basis of density functional theory:

- 1: Aside from a continuous shift, the system's external potential of interacting particles is solely determined by the ground-state particle density of the system.
- 2: For every possible external potential, there exists a universal functional  $F[n]$ . The minimization of the functional  $F[n]$  (equation below) with respect to the particle density  $n(r)$  determines the exact ground-state energy of the system. This particle density equals the ground-state density  $n_0$  of the system of interacting particles.

The mentioned theorems simply state that if the functional is known, knowing all the properties of the system in ground state is possible. The problem is that these statements do not give any hints on constructing such desired functional. In the following part we will consider spin-unpolarized electron-based systems  $\psi = \psi(e)$  where  $n=n(\text{up})+n(\text{down})$  which the disperses spin's freedom. Hartree atomic units will be used for convenience. Thus, after distinguishing the interactions between ion-ion and evaluating the expecting value of the electronic system's Hamiltonian, one can express the energy in terms of functional of the electron density  $n(r)$ :

$$E_{HK}(n) = \langle \Psi | T + V_{int} + V_{ext} | \Psi \rangle = T(n) + E_{int}(n) + \int dr V_{ext}(r)n(r) \quad (2.18)$$

Based on the results from Levy [10] the  $F(n)$  functional can also be expressed as:

$$F(n) = \min_{|\Psi\rangle \rightarrow n(r)} (\langle \Psi | T + V_{int} | \Psi \rangle) \quad (2.19)$$

## 2.2.2 Kohn-Sham Equations

A year after the publication of Hohenberg-Kohn paper on the description of the external potential using the density of the particles, Kohn and Sham [11] introduced an innovative methodology which could be successfully used to create appropriate energy functionals. The general idea revolved around the construction of an auxiliary fictive system of non-interacting particles which would result in the same ground-state density as the actual physical system with interacting electrons. The Hamiltonian of the defined system can be expressed as:

$$H = T_0 + V_{KS} \quad (2.20)$$

where the  $T_0$  is the kinetic energy operator and  $V_{KS}$  is the effective local potential. In the following we will define the effective local potential. Calculating the electron density of the non-interacting system of electrons is carried out by summarizing all of the occupied single-particle orbitals  $\phi_i$ .

$$n(r) = \sum |\psi_i|^2 \quad (2.21)$$

thus the kinetic energy functional will be defined as:

$$T_0(n) = -\frac{1}{2} \sum \langle \phi_i | \nabla^2 | \phi_i \rangle \quad (2.22)$$

in which the  $|\phi_i\rangle$  are the one-electron orbitals, moreover the summation goes over all of the electrons in the system. All of the system orbitals are occupied considering the Pauli exclusion principle. Thus we can write the Kohn-Sham energy functional as:

$$E_{KS}(n) = T_0(n) + E_{Hartree}(n) + E_{xc}(n) + \int dr V_{ext}(r)n(r) \quad (2.23)$$

where  $F(n)$  can be defined as the summation of the terms  $T_0(n)$ ,  $E_{Hartree}(n)$ ,  $E_{xc}(n)$ . kinetic energy is already described above, the Hartree energy can also be defined as:

$$E_{Hartree}(n) = \frac{1}{2} \int \int dr dr' \frac{n(r)n(r')}{|r - r'|} \quad (2.24)$$

Finally, the exchange-correlation energy functional  $E_{xc}(n)$  is specified which embodies all of the quantum mechanical many-body interactions. Then, by applying the Ritz variational principle for the electron density with the constraint of  $\langle \phi_i | \phi_j \rangle = \delta_{ij}$  results in the variational equation of:

$$\frac{\delta}{\delta n} (E_{KS}(n(r)) - \sum \epsilon_{ij} (\langle \phi_i | \phi_j \rangle - \delta_{ij})) = 0 \quad (2.25)$$

by diagonalizing this we obtain a Schrodinger-like Kohn-Sham equation:

$$\left(-\frac{1}{2}\nabla^2 + \frac{\delta E_{Hartree}}{\delta n} + \frac{\delta E_{xc}}{\delta n} + V_{ext}\right)\phi_i = \epsilon_i\phi_i \quad (2.26)$$

Identifying the Hamiltonian will yield:

$$(T_0 + V_{KS})\phi_i = \epsilon_i\phi_i \quad (2.27)$$

Thus the effective Kohn-Sham potential can be expressed as:

$$V_{KS} = \frac{\delta E_{Hartree}(n)}{\delta n} + \frac{\delta E_{xc}}{\delta n} + V_{ext} = v_H + v_{xc} + v_{ext} \quad (2.28)$$

The only term which is not calculated is the exchange-correlation energy functional  $E_{xc}$ . The exact form or value is not known but substantial approximations are available. In their main paper Kohn and Sham suggested a local density approximation to overcome this challenge. Additionally, they also proposed an improvement using a gradient expansion which will be discussed in the next section.

**Self consistent solution:** Since both of the exchange-correlation and Hartree potentials have dependencies to the electron density, system's ground state energy should be calculated. the practical approach is the iterative and self-consistent approach. As can be seen in Figure 2.4, initially, an approximated electron density of the non-interacting system is used to set up the Kohn-Sham potential of the system. after that, the Kohn-Sham equations are solved using this approximated value ,which yields a new density. Stabilization of the self-consistent cycle (numerically) is carried out via introducing a mixing scheme to the methodology which mixes the old and new density, this value is then passed to the next iteration for the generation of a new wave-function. This process is repeated until an energy convergence up to a defined precision is reached.

### 2.2.3 Exchange and Correlation

**Local density approximation (LDA):** local density approximation (LDA) in which the exchange-correlation energy of an inhomogeneous electron system, is estimated by that of a homogeneous electron gas:

$$E_{XC}^{LDA}(n) = \int dr n(r)(e_x(n(r)) + e_c(n(r))) \quad (2.29)$$

It's worth to mention that for the homogeneous electron gas, the exchange part is can be analytically defined as:

$$e_x(n(r)) = -\frac{2}{3}\left(\frac{3}{\pi}n(r)\right)^{\frac{1}{3}} \quad (2.30)$$

Thus, leaving only the correlation part to be estimated via quantum Monte-Carlo simulations [12]. Efficiency of the LDA originates from the fact that the long range Coulomb term in the Kohn-Sham approach is separately treated as the

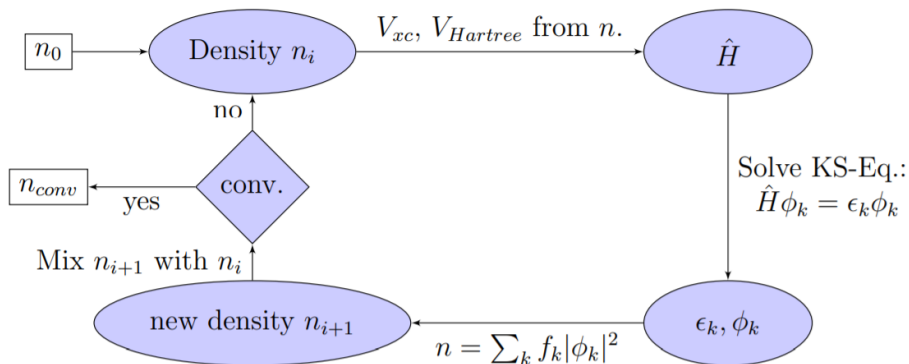


Figure 2.4: Schematic representation of the self consistent cycle of density-functional theory: initializing from an approximated density value  $n_0$  the Hamiltonian is generated via calculating the exchange-correlation and Hartree potentials  $V_{xc}$  and  $V_H$  respectively. Then, solving the Kohn-Sham equation for eigen-energies  $\epsilon_k$  and wavefunctions  $\phi_k$  are calculated resulting in a density value  $n_{i+1}$ . The process is repeated until reaching a predefined convergence threshold is reached, it is done by mixing the old and new density values before entering the next step.

rest of the interactions in many practical cases are almost local. Moreover, the LDA fulfills the uniform scaling relations [10]. On the other hand, the two disadvantages of LDA are:

- 1- Having no dependency on the density gradient
- 2- If the Wigner-Seitz radius is approaches to near-zero values (for large densities), while the exact correlation energy approaches a constant, the correlation energy mails towards infinity.

This problem set the inspiration for the development of a new approximation, hence, resulting in the appearance of the generalized gradient approximation.

## 2.2.4 Generalized gradient approximation (GGA)

: GGA in most cases yields better results by employing a scheme in which the density gradient is enhancement via  $F_{xc}$ :

$$E_{XC}^{GGA}(n) = \int dr n(r) (e_x(n(r)) F_{xc}(|\nabla n(r)|)) \quad (2.31)$$

where  $e_x(n(r))$  is the exchange energy density. Different from the LDA which is universal, approximating the exchange correlation functional have many ways while each one is tailored for solving a distinct problem. The mostly used tailored

GGA variations are the Perdew-Wang (PW91) [13], Perdew-Burke-Ernzerhof (PBE) [14], PBE-sol [15] and Armiento-Mattsson (AM05) [16].

## 2.2.5 Car-Parrinello approach

Initially proposed by Roberto Car and Michele Parrinello 1985 [17], the Car-Parrinello approach accurately simulates molecular dynamics. It establishes the electronic degrees of freedom as fictitious dynamical variables for keeping the system close to the Born-Oppenheimer surface. Based on this scheme, Car and Parrinello introduced this Lagrangian:

$$L_{CP} = \sum \frac{1}{2} M_l R_l^2 + \sum \mu \langle \phi_i | \dot{\phi}_i \rangle - \langle \psi_0 | H_e^{KS} | \psi_0 \rangle + \sum \Lambda (\langle \phi_i | \dot{\phi}_i \rangle - \delta_{ij}) \quad (2.32)$$

In which the terms are the nuclei kinetic energy, the fictitious kinetic energy of the KS orbitals  $\phi_i$ , KS energy, a Lagrange multiplier respectively. Moreover,  $\mu$  is the fictitious mass,  $M_l$  and  $R_l$  represent mass and position of the  $l$ -th nucleus,  $\psi_0$  is the many-body wave function constructed with the orbitals obtained from KS Hamiltonian  $H_e^{KS}$ , and  $\Lambda_{ij}$  are the Lagrange multipliers. Thus the following Car-Parrinello equations of motion is generated from the Lagrangian equation:

:

$$M_l R_l''(t) = -\nabla_l \langle \psi_0 | H_e^{KS} | \psi_0 \rangle \mu \phi_i(t) = -H_e^{KS} \phi_i + \sum \Lambda_{ij} \phi_j \quad (2.33)$$

The fictitious mass  $\mu$  is reversly related to the maximum and minimum electron frequencies:

$$\omega_e^{min} = \left( \frac{E_{gap}}{\mu} \right)^{\frac{1}{2}} \omega_e^{max} = \left( \frac{E_{cut}}{\mu} \right)^{\frac{1}{2}} \quad (2.34)$$

where  $E_{cut}$  is the largest kinetic energy in an expansion of the wave function over the space in terms of a plane wave basis sets and  $E_{gap}$  is the electronic energy difference between the highest occupied (HOMO) and the lowest unoccupied (LUMO) orbital. Furthermore, for a stable Car-Parrinello propagation resulting from an adiabatic separation of the electronic and nuclear subsystems, the nuclear and electronic subsystems must be separated dynamically, meaning, the difference between the highest phonon frequency  $\omega_e^{max}$  and the lowest electron frequency  $\omega_e^{min}$  and should be substantial. Since  $\omega_e^{max}$  and  $E_{gap}$  are parameters which are defined by the physics of the system, the only parameter to control adiabatic separation is the fictitious mass  $\mu$ . By decreasing the  $\mu$ , not only the electronic spectrum on the frequency scale shifts upwards (as desired), but also an increase of the maximum electron frequency  $\omega_e^{max}$  will be achieved. Since the time step is inversely proportional to  $\omega_e^{max}$ , the larger  $\omega_e^{max}$ , the smaller time step. Therefore, a trade off is made on the control parameter  $\mu$  [18]. Car-Parrinello approach also introduces a thermostat into the system. For the CP simulations discussed in this thesis (third paper), the Nose-Hoover thermostat is used [19]. The method originates from the extension of the analysis of Nose to derive a set of equations of motion

$$q' = p/m p' = F(q) - \zeta_p \quad (2.35)$$



where  $p$  and  $q$  represent of the momentum and the coordinates of particles in a physical system, and  $F(q)$  represents the force which is derived from the inter-particle potentials. The friction coefficient  $\zeta$  can be achieved by the first-order differential equation:

$$\zeta = \frac{\sum \frac{p^2}{m - Xk_B T}}{Q} \quad (2.36)$$

where  $X$  is the number of degrees of freedom in the physical system,  $T$  is the specified temperature,  $k_B$  is Boltzmann's constant, and the parameter  $Q$  defines temperature fluctuation's time-scale. The function  $\zeta$  can be either a negative or positive value depending on the instantaneous kinetic energy of the particle to be higher or lower than  $Xk_B T$ , which results in acceleration or damping of the particle and thus to cooling or heating.

## References

- [1] Materials, Applied. "GINESTRA". English. In: (2020).
- [2] Henry, CH and Lang, D Vo. "Nonradiative capture and recombination by multiphonon emission in GaAs and GaP". In: *Physical Review B* vol. 15, no. 2 (1977), p. 989.
- [3] Huang, Kun and Rhys, Avril. "Theory of light absorption and non-radiative transitions in F-centres". In: *Selected Papers Of Kun Huang: (With Commentary)*. World Scientific, 2000, pp. 74–92.
- [4] Vandelli, Luca et al. "A Physical Model of the Temperature Dependence of the Current Through SiO<sub>2</sub>/HfO<sub>2</sub> Stacks". In: *IEEE Transactions on Electron Devices* vol. 58, no. 9 (2011), pp. 2878–2887.
- [5] Jiménez-Molinos, F et al. "Physical model for trap-assisted inelastic tunneling in metal-oxide-semiconductor structures". In: *Journal of Applied Physics* vol. 90, no. 7 (2001), pp. 3396–3404.
- [6] Zhang, Manhong et al. "Unification of three multiphonon trap-assisted tunneling mechanisms". In: *Journal of Applied Physics* vol. 110, no. 11 (2011), p. 114108.
- [7] Thomas, Llewellyn H. "The calculation of atomic fields". In: *Mathematical proceedings of the Cambridge philosophical society*. Vol. 23. 5. Cambridge University Press. 1927, pp. 542–548.
- [8] Fermi, E. "Statistical calculation of the Rydberg corrections of the s terms". In: *magazine for "u r physics* vol. 49, no. 7-8 (1928), pp. 550–554.
- [9] Hohenberg, P and Kohn, W. "Elementary excitations in solids". In: *Physical Review* vol. 136 (1964), B864–B871.
- [10] Levy, Mel and Perdew, John P. "Hellmann-Feynman, virial, and scaling requisites for the exact universal density functionals. Shape of the correlation potential and diamagnetic susceptibility for atoms". In: *Physical Review A* vol. 32, no. 4 (1985), p. 2010.

- [11] Kohn, Walter and Sham, Lu Jeu. “Self-consistent equations including exchange and correlation effects”. In: *Physical review* vol. 140, no. 4A (1965), A1133.
- [12] Ceperley, David M and Alder, Berni J. “Ground state of the electron gas by a stochastic method”. In: *Physical review letters* vol. 45, no. 7 (1980), p. 566.
- [13] Perdew, John P and Wang, Yue. “Accurate and simple analytic representation of the electron-gas correlation energy”. In: *Physical review B* vol. 45, no. 23 (1992), p. 13244.
- [14] Perdew, John P, Burke, Kieron, and Ernzerhof, Matthias. “Generalized gradient approximation made simple”. In: *Physical review letters* vol. 77, no. 18 (1996), p. 3865.
- [15] Csonka, Gábor I et al. “Assessing the performance of recent density functionals for bulk solids”. In: *Physical Review B* vol. 79, no. 15 (2009), p. 155107.
- [16] Armiento, Rickard and Mattsson, Ann E. “Functional designed to include surface effects in self-consistent density functional theory”. In: *Physical Review B* vol. 72, no. 8 (2005), p. 085108.
- [17] Car, Richard and Parrinello, Mark. “Unified approach for molecular dynamics and density-functional theory”. In: *Physical review letters* vol. 55, no. 22 (1985), p. 2471.
- [18] Marx, Dominik and Hutter, Jürg. *Ab initio molecular dynamics: basic theory and advanced methods*. Cambridge University Press, 2009.
- [19] Nosé, Shūichi. “A molecular dynamics method for simulations in the canonical ensemble”. In: *Molecular physics* vol. 52, no. 2 (1984), pp. 255–268.

# Results



## Chapter 3

# Multiscale modeling of $\text{CeO}_2/\text{La}_2\text{O}_3$ stacks for material/defect characterization

### Abstract

Presence of defects in high-k dielectric materials will affect device's electrical properties, thus, defect/material characterization is of great importance. We present a simulation based methodology relying on an accurate description of charge trapping and transport that is useful to extract relevant information on material and defect characteristics. This methodology was applied to cerium oxide and lanthanum oxide high-k dielectric materials and as a result, material properties alongside defect characteristics were extracted. Consequently, main charge conduction mechanism was identified to be trapassisted tunneling (TAT).

### Contents

3.1	Introduction . . . . .	35
3.2	Device experiments and simulations . . . . .	36
3.3	Results . . . . .	37
3.4	Conclusion . . . . .	39
	References . . . . .	41

### 3.1 Introduction

With the advancements in technology such as Artificial Neural Networks (ANN), Resistive Random-Access Memory (RRAM) and silicon being saturated in device application, the need for new materials is increasing [1]. High dielectric constant materials used in complementary metal oxide material (CMOS) transistors replaced silicon-based gate oxides [2]. Among these new high-k materials, lanthanides with their high permittivity and large electron mean-free-path are promising materials for next generation devices [3]. Bilayer  $\text{CeO}_2/\text{La}_2\text{O}_3$  has shown to improve MOSFET characteristics, such as channel mobility, sub-threshold slope and control over negative threshold voltage shift [4]. However, although lacking, a clear assessment and characterization of the traps present in

these materials is crucial for technology optimization as well as for identifying their potential as gate dielectric stacks. In this work we use a simulation-based methodology, relying on an accurate and comprehensive description of charge trapping and transport, to characterize defect properties and identify the charge transport mechanisms by employing experimental data obtained from measurements.

### 3.2 Device experiments and simulations

A comprehensive multiscale modeling methodology was developed to characterize and accurately describe/extract defect properties in dielectric stacks used in logic and memory devices (resistive RAMs and ferroelectrics). This is important for linking the atomic properties of the material to the electrical behavior of the device. The methodology utilized GINESTRA<sup>TM</sup> [5], a software based on a multiscale modeling approach which includes a wide-range of physics models accounting for charge trapping and transport, atomic species motion, and material modifications due to different phenomena such as degradation, polarization switching, phase change [6, 7, 8, 9, 10]. Charge transport is modeled accounting for multiple conduction mechanisms as illustrated in Figure 3.1. Defect-assisted charge trapping and transport is described in the framework of the multi-phonon theory accounting for carriers–phonons coupling and lattice relaxation processes. It is found to be the dominant transport mechanism in a wide variety of dielectric materials. Non-defectrelated conduction mechanisms, such as direct/Fowler–Nordheim tunneling, thermionic emission, and drift, are also considered consistently with the trap-assisted transport. Calculations are performed considering the local potential given by the applied bias and the defect charge state and occupation.

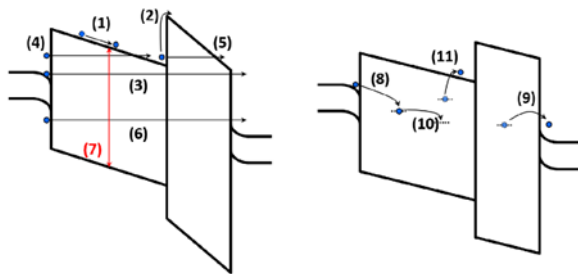


Figure 3.1: Schematic representation of the different carrier transport mechanisms considered in GINESTRA<sup>TM</sup>, mechanisms are shown in two similar devices for better comprehension. (1) drift-diffusion, (2) thermionic emission, (3) direct tunneling, (4) electrode-band tunneling, (5) intra-band tunneling, (6) band-to-band tunneling, (7) local generation-recombination, (8) electrode-to-trap capture, (9) trap-to-electrode emission, (10) trap-to-trap transition, RTT, (11) trap-to-band transition, RTTB were used for calculations.

The methodology we developed exploits the simulation framework to automatically reproduce a given set of experimental data (I-V, C-V, G-V as a function of temperature and frequency) in order to extract material (e.g. permittivity, band-gap, electron-affinity) and defect (thermal ionization energy  $E_t$ , relaxation energy  $E_{rel}$ , and traps density  $N_t$ ) parameters. This parameter extraction tool [6, 7, 8] – that relies on the charge trapping/transport mechanisms described above – is applied to capacitance and leakage current data measured on  $CeO_2$  and  $La_2O_3$  based stacks that we collected from the literature. Temperature dependent leakage currents are used to accurately estimate  $E_{rel}$ , which ultimately controls carriers capture,  $\tau_c$ , and emission,  $\tau_e$ , times and thus the whole TAT process [9-10]

### 3.3 Results

Material stoichiometry will affect its physical properties (band gap, permittivity, ...) which in turn, will result in some variations in device's electrical behavior. Hence, prior to defect investigation of bilayer temperature-dependent J-V, the physical values of  $CeO_2$  and  $La_2O_3$  had to be extracted. Since all samples had thicknesses between 4nm to 13nm, identifying any changes that might have been originated from interfacial/intermixing layer during sample preparation was crucial. These changes, although small, might degrade electrical properties. Dielectric permittivity ( $k$ ) was extracted by reproducing experimental C-V data (Figure 3.2) measured on  $CeO_2$  and  $La_2O_3$  monolayer stacks [11, 12]. Extracted dielectric permittivity values of  $La_2O_3$  and  $CeO_2$  are 14 and 17.35 respectively, i.e. significantly lower than the values of 27 and 26 typically reported [13, 14]. This can be ascribed to the presence of carbon [13]. The extracted dielectric permittivity was used in subsequent leakage current simulations that allowed to automatically and consistently reproduce several sets of experimental data (Figure 3.3) [11], [15, 16, 17, 18].

Parameter	Dielectric material						
	Monolayer					Bilayer	
	$CeO_2$ [3]	$CeO_2$ [8]	$La_2O_3$ [7]	$La_2O_3$ [5]	$La_2O_3$ [6]	$CeO_2$ [9]	$La_2O_3$ [9]
Relaxation energy (eV)	1.44	1.34	0.6	0.4	0.6	1	0.4
Electron affinity (eV)	2.2	2.9	2.1	1.97	2.3	2.9	2
Permittivity	17.35	17.35	14	14	14	17.35	14
Bandgap (eV)	3.33	3.11	5.8	5.8	5.8	3.11	5.8
Defect density ( $cm^{-3}$ )	$2 \times 10^{21}$	$7.7 \times 10^{19}$	$2.9 \times 10^{19}$	$1.44 \times 10^{20}$	$2.1 \times 10^{20}$	$1.4 \times 10^{21}$	$1.6 \times 10^{20}$
Thermal ionization energy (eV)	$2.3 \pm 0.3$	$1.74 \pm 0.4$	$2.1 \pm 0.6$	$1.7 \pm 0.8$	$2.1 \pm 0.9$	$1.8 \pm 0.3$	$2.1 \pm 0.6$

Table 3.1: Table of extracted parameters

This allowed to characterize the relevant material ( $E_g$  and electron affinity) and defect properties ( $E_{rel}$ ,  $E_T$ ,  $N_t$ ). Extracted defects thermal ionization energies are of 2.1eV and 1.7 eV below the conduction band minimum for  $La_2O_3$  and  $CeO_2$  respectively. Table. 1 summarizes the set of material and defect

parameters extracted by applying the automated methodology to the wide set of experimental data in Figure 3.2 and Figure 3.3. As can be seen, there is a good consistency between extracted parameters from different reports in literature.

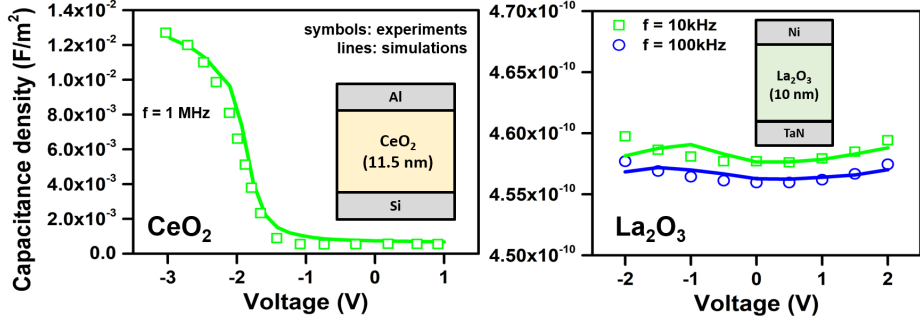


Figure 3.2: C-V fittings for a)  $\text{CeO}_2$  and b)  $\text{La}_2\text{O}_3$  monolayers to that of the reports from literature [11, 12], simulations and experimental data are shown with lines and symbols respectively.

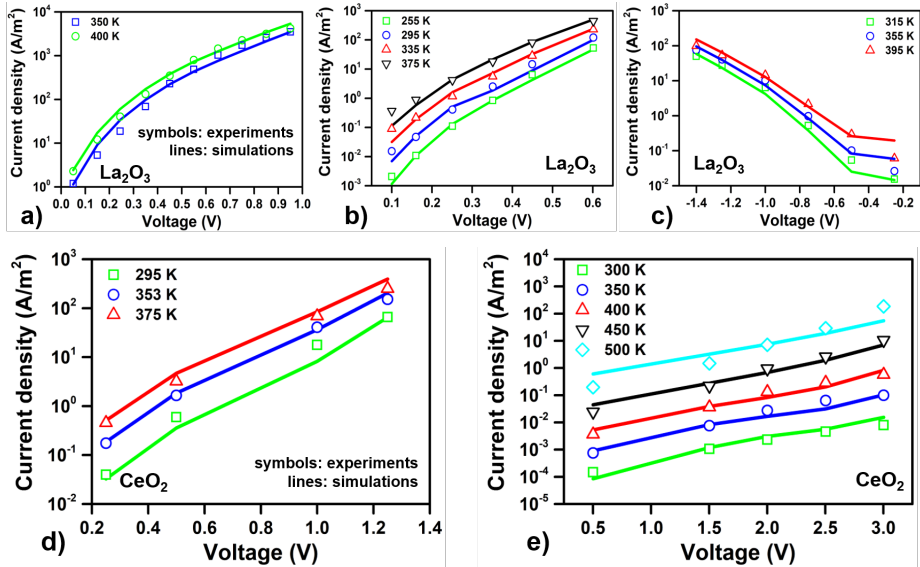


Figure 3.3: Temperature-dependent J-V curves reproduced from five sets of experimental data (a-e) for  $\text{La}_2\text{O}_3$  and  $\text{CeO}_2$  which were collected from literature [11] [15, 16, 17, 18]. For the sake of comparison the simulations are drawn with lines and experimental data are displayed by symbols.

Finally, by combining extracted material/defect parameters from single layers, temperature dependent J-V curves of bilayer  $\text{La}_2\text{O}_3/\text{CeO}_2$  were reproduced, see



Figure 3.4. The current contribution due to pure tunneling mechanisms (i.e. the ones not assisted by traps such as Direct and Fowler-Nordheim) is also shown (dashed lines). As can be seen the presence of traps increases the currents by

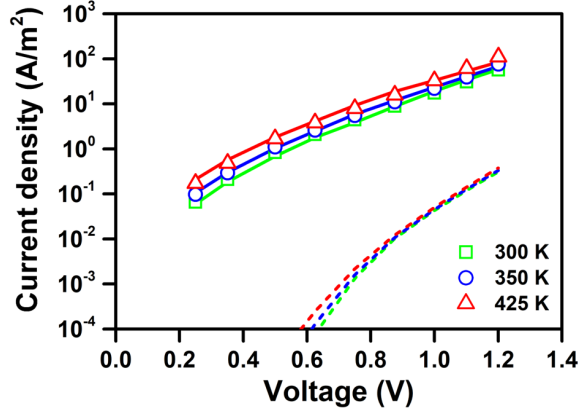


Figure 3.4: Depicting J-V curves of  $\text{CeO}_2/\text{La}_2\text{O}_3$  stack fittings of reported experimental results [19], a comparison between charge transport with (solid lines) and without (dashed lines) TAT are visible. Experimental data are demonstrated by symbols.

orders of magnitude, indicating TAT as the dominant conduction mechanism. In Figure 3.4, reproduced data fits the experimental results [19] with less than 2 % error, proving the accuracy and validity of the provided methodology. Extracted trap properties can also be used to identify their atomic nature. A comparison of the extracted traps energy level with the values calculated with Density Functional Theory (DFT) for different trap types, Figure 3.5, indicate that neutral and neutral/positively charged oxygen vacancies are the most probable defects assisting the conduction in  $\text{La}_2\text{O}_3$  and  $\text{CeO}_2$  respectively [20, 21]. Device's band diagram is drawn in Figure 3.6, illustrating the extracted defect energy levels in the bandgap.

### 3.4 Conclusion

We introduced a new methodology for characterization of materials properties and defects. Utilizing Multiscale modeling software GINESTRA<sup>TM</sup> we were able to accurately characterize  $\text{La}_2\text{O}_3$  and  $\text{CeO}_2$  material and defect properties by reproducing C-V and J-V measurements. Extracted parameters suggest that the trap energy levels for  $\text{La}_2\text{O}_3$  and  $\text{CeO}_2$  are 2.1eV and 1.7 eV below conduction-band bottom respectively, which are consistent with DFT calculation results for neutral and positively charged oxygen vacancies. Finally, results indicate trap-assisted tunneling as the dominant conduction mechanisms.

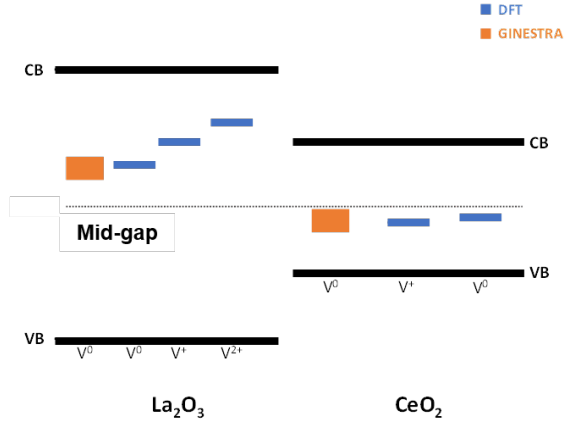


Figure 3.5: Illustration of  $\text{La}_2\text{O}_3$  and  $\text{CeO}_2$  bandgap. Orange rectangle represents the range of defect energies extracted by  $\text{GINESTRA}^{TM}$  and blue lines represent calculated neutral and charged oxygen vacancies from DFT calculations reported in literature.

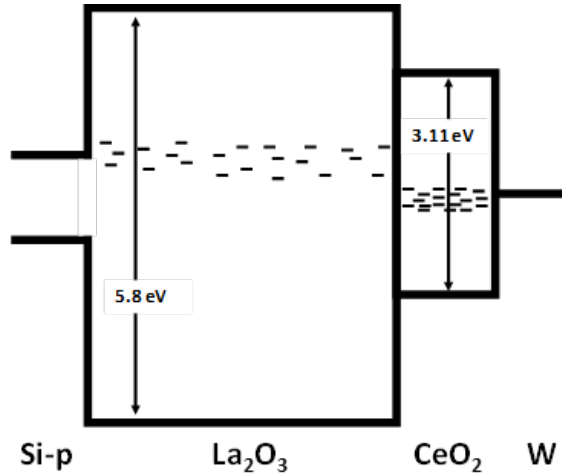


Figure 3.6: Bandgap plot of bilayer  $\text{CeO}_2/\text{La}_2\text{O}_3$ , scattered dashes represent energy traps.

## References

- [1] La Torraca, P. et al. “Multiscale modeling for application-oriented optimization of resistive random-access memory”. English. In: *Materials* vol. 12, no. 21 (2019). Cited By :8.
- [2] Gopalan, S. et al. “Al2O3 thin films on Silicon and Germanium substrates for CMOS and flash memory applications”. English. In: *AIP Conference Proceedings*. Vol. 1859. Cited By :1. 2017.
- [3] Chiang, Y. -. et al. “Defect and transport properties of nanocrystalline CeO<sub>2-x</sub>”. English. In: *Applied Physics Letters* vol. 69, no. 2 (1996). Cited By :330, pp. 185–187.
- [4] Yang, B. L. et al. “Improving the electrical characteristics of MOS transistors with CeO<sub>2</sub>/La<sub>2</sub>O<sub>3</sub> stacked gate dielectric”. English. In: *Microelectronics Reliability* vol. 52, no. 8 (2012). Cited By :15, pp. 1613–1616.
- [5] GINESTRA, Applied Material’s. “<http://www.appliedmaterials.com/products/applied-mdlx-ginestrasimulation-software>”. In: (0). Cited By :1.
- [6] Padovani, A. et al. “A Sensitivity Map-Based Approach to Profile Defects in MIM Capacitors From I-V, C-V, and G-V Measurements”. English. In: *IEEE Transactions on Electron Devices* vol. 66, no. 4 (2019). Cited By :6, pp. 1892–1898.
- [7] Larcher, L. et al. “Defect spectroscopy from electrical measurements: A simulation based technique”. English. In: *2018 IEEE Electron Devices Technology and Manufacturing Conference, EDTM 2018 - Proceedings*. Cited By :1. 2018, pp. 145–147.
- [8] Padovani, A. et al. “Multiscale modeling of defect-related phenomena in high-k based logic and memory devices”. English. In: *Proceedings of the International Symposium on the Physical and Failure Analysis of Integrated Circuits, IPFA*. Vol. 2017-July. Cited By :14. 2017, pp. 1–6.
- [9] Larcher, L. et al. “Extracting Atomic Defect Properties From Leakage Current Temperature Dependence”. English. In: *IEEE Transactions on Electron Devices* vol. 65, no. 12 (2018). Cited By :8, pp. 5475–5480.
- [10] Vandelli, L. et al. “A physical model of the temperature dependence of the current through SiO<sub>2</sub>/HfO<sub>2</sub> stacks”. English. In: *IEEE Transactions on Electron Devices* vol. 58, no. 9 (2011). Cited By :179, pp. 2878–2887.
- [11] Chiu, F. -. “Current conduction mechanisms in CeO<sub>2</sub> thin films”. English. In: *Electrochemical and Solid-State Letters* vol. 11, no. 6 (2008). Cited By :21, H135–H137.
- [12] Wu, S. -. et al. “Stability of La<sub>2</sub>O<sub>3</sub> metal-insulator-metal capacitors under constant voltage stress”. English. In: *Japanese Journal of Applied Physics* vol. 49, no. 4 PART 2 (2010). Cited By :11.

- [13] Cheng, J. -. et al. “Growth and characteristics of La<sub>2</sub>O<sub>3</sub> gate dielectric prepared by low pressure metalorganic chemical vapor deposition”. English. In: *Applied Surface Science* vol. 233, no. 1-4 (2004). Cited By :64, pp. 91–98.
- [14] Tye, L. et al. “Electrical characteristics of epitaxial CeO<sub>2</sub> on Si(111)”. English. In: *Applied Physics Letters* vol. 65, no. 24 (1994). Cited By :127, pp. 3081–3083.
- [15] Sen, B. et al. “Trapping characteristics of lanthanum oxide gate dielectric film explored from temperature dependent current-voltage and capacitance-voltage measurements”. English. In: *Solid-State Electronics* vol. 51, no. 3 (2007). Cited By :40, pp. 475–480.
- [16] Kim, Y. et al. “Space-charge-limited currents in la<sub>2</sub>O<sub>3</sub> thin films deposited by E-beam evaporation after low temperature dry-nitrogen annealing”. English. In: *Japanese Journal of Applied Physics, Part 1: Regular Papers and Short Notes and Review Papers* vol. 44, no. 6 A (2005). Cited By :43, pp. 4032–4042.
- [17] Kim, Y. et al. “Electrical properties of vacuum annealed La<sub>2</sub>O<sub>3</sub> thin films grown by E-beam evaporation”. English. In: *Microelectronics Journal* vol. 36, no. 1 (2005). Cited By :38, pp. 41–49.
- [18] Rahman, M. S. et al. “Current transport mechanism in high- cerium oxide gate dielectrics grown on germanium substrates”. English. In: *Electrochemical and Solid-State Letters* vol. 12, no. 5 (2009). Cited By :18, H165–H168.
- [19] Feng, X. et al. “On the current conduction mechanisms of CeO<sub>2</sub>/La<sub>2</sub>O<sub>3</sub> stacked gate dielectric”. English. In: *Microelectronics Reliability* vol. 54, no. 6-7 (2014). Cited By :7, pp. 1133–1136.
- [20] Xiong, K. and Robertson, J. “Oxygen vacancies in high dielectric constant oxides La<sub>2</sub>O<sub>3</sub>, Lu<sub>2</sub>O<sub>3</sub>, and LaLuO<sub>3</sub>”. English. In: *Applied Physics Letters* vol. 95, no. 2 (2009). Cited By :34.
- [21] Aškrabić, S. et al. “F-centre luminescence in nanocrystalline CeO<sub>2</sub>”. English. In: *Journal of Physics D: Applied Physics* vol. 46, no. 49 (2013). Cited By :53.

## Chapter 4

# BELLO: a script tool for bond element and lattice local-order analysis of disordered systems

### Abstract

The characterization of reliable atomic structure of disordered systems, such as amorphous and glasses, is a fundamental step for most theoretical investigations. The properties of short- and medium-range local order structures are responsible for the electronic, optical and transport properties of the disordered systems. Here, we present BELLO code, a post-processing script-tool created for the automatic analysis and extraction of structural characteristics of disordered and amorphous systems. BELLO is agnostic to the code that generated single configurations or trajectories. Its capabilities include calculation of order parameter  $q$ , folded structure identification and statistics, and detailed atomic coordination number and pair/angle-distribution functions. Working principles of the code are described and tested on ab initio molecular dynamics trajectories of amorphous  $\text{Ge}_{0.5}\text{Se}_{0.5}$  chalcogenide.

### Contents

4.1	Introduction . . . . .	43
4.2	Software Design . . . . .	45
4.3	Description of the code . . . . .	46
4.4	Installation, input and Output structure . . . . .	52
4.5	User Inputs . . . . .	54
4.6	Module outputs . . . . .	56
4.7	Conclusion . . . . .	60
	References . . . . .	60

### 4.1 Introduction

Non-crystalline solids are rapidly growing interest for their photonic, electronic, and photoelectric applications. This includes, *e.g.*, amorphous hydrogenated

Si and amorphous oxides for solar cells [1, 2], optical amplifier [3] and thin-film transistors [4, 5], polymeric fibers optics [6] and sensors [7], chalcogenide amorphous thin films for DVDs [8] and memories [9, 10]. The common characteristics of these materials is the disordered atomic structure. This implies a few general properties such as homogeneity, isotropy, nanoscale structure controllability, large sample dimension, conchoid surface cleavage, more flexibility and lower density with respect to the corresponding crystalline phase. At the same time, disorder affects most of the electronic and transport properties of these materials. For example, in a non-crystal system electrons and holes at band edges and mid-gaps are localized [11, 12]. As a consequence, the mobility in amorphous systems becomes smaller than that in the corresponding crystal. In a similar way, the lattice vibrations are also localized in non-crystal structure, which provide lower thermal conductivity.

The microscopic origin of these characteristics is intimately related the formation of local-order structures within the sample. Indeed, even though it is impossible to envisage a unique atomic configuration for a disordered lattice, amorphous and glass structures are not completely random, as that in an ideal gas. At the atomic scale, non-crystalline solids are characterized by so-called *normal bonding* structures and defects [13]. A normal bond can be defined as topologically the same atom connection with that existing in the corresponding crystal, while defects refer to ill-atomic coordination, such as dangling and *wrong* bonds, which do not exist in the crystal [14]. The normal bonding structure can further be divided into the short ( $< 0.5$  nm) [15] and the medium-range (0.5–3.0 nm) structures. The former describe atomic bonding and first-neighbor interactions, the latter describe the atomic coupling beyond the second-neighbors. Short range structures are determined by three main parameters: the coordination number  $Z$  of atoms, the bond length  $r$ , and the bond angle  $\theta$ . The coordination number is a direct consequence of the electron configuration and the chemical composition of the system which may cause the formation of both homopolar and heteropolar bonds. The bond length  $r$  increases in proportion to size of the atomic species. Bond angles keep into account the bond distortions and quantify the variance to the ideal crystal structure. Characteristic angles may also produce the so-called corner-shared and edge-shared configurations, which are connected to the medium-range structures, such as rings or three-dimensional continuous random networks. Thus, the analysis of structural properties (e.g. coordination and bond orientational order) is of paramount relevance the understanding of disordered systems [12, 16], including their electronic [17, 18], elastic [19] and thermodynamics properties (e.g. phase change transitions) [20, 21].

Experimentally, x-ray (e-beam and neutron) diffraction [22] and EXAFS spectroscopy [23] are the most common investigation approaches for the analysis of disordered systems. In addition to these direct structural experiments, there are less direct ones, such as vibrational spectroscopy (e.g. infrared transmission, Raman scattering, and inelastic neutron scattering) [24] and spin-related methods (e.g. NMR) [25]. While these methods provide general information on short range order, by measuring for example the radial distribution function or the first sharp diffraction peak (FSDP), they do not give sufficient in-depth quantitative

information about local orders, such as bond polarity, folded structures, angular distortions, ring statistics and networks connectivity.

Since the non-crystalline structure cannot be determined explicitly from experiments, structural computer simulations have become indispensable. Most atomistic studies employ both classical or *ab initio* molecular dynamics (MD) calculations, which rely upon Newton equations of ions at finite temperature. The amorphous models are obtained by using melt-and-quench techniques, in which a sample is melt at a temperature higher than the melting temperature and followed by a thermal quench (typically to room temperature) fast enough to avoid crystallization. Within the ergodic assumption, the statistical structural properties of disordered systems (liquids, melt systems, amorphous and glasses) rely on the time average properties extracted from simulated trajectories. This implies to analyze a multitude of configurations with tens to thousands of simulated atoms.

In this paper, we introduce the code BELLO (Bond Element Lattice Local Order), a script-tool designed to extract and analyze local order structures in disordered materials. BELLO acts as computationally inexpensive post-processing step that needs as unique input, the atomic positions in standard XYZ format, independently from the physical model (e.g. classical or *ab initio* MD, MonteCarlo, tight-binding, etc) and the numerical assumptions or the code used to generate them. BELLO is publicly available under the terms of the GNU General Public License as published by the Free Software Foundation, either version 3 of the License, or any later version; and is distributed at **Web link**. In the following we present the main technical characteristics of the code and its principal features. As prototypical application case, we present the structural analysis of melt  $\text{Ge}_{0.5}\text{Se}_{0.5}$  chalcogenide system at 1000K, resulting from first principles molecular dynamics simulations.

## 4.2 Software Design

BELLO is written in python 3.7 utilizing NumPy and Pandas standard libraries, hence the code is compatible with standard trajectory outputs from most of the atomistic simulation engines. Parallelization is not yet implemented as the code runs relatively fast for dense systems. BELLO requires a calculation with most of the first-principles electronic-structure calculation packages (QuantumEspresso, VASP, SIESTA, etc.) to generate atomic structure trajectories in standard XYZ format. No additional calculations are required. Using these trajectories as input and by analyzing them in 3D real space, the code extracts statistical data such as order parameter  $q$ , detailed-coordination number, radial and angle distribution functions, local population statistics and local order coordinates in PDB and XYZ. Furthermore, BELLO is agnostic the code that generated the single configuration or trajectories as well as the elements of the structure.

## 4.3 Description of the code

### 4.3.1 Module: BELLO-core-v1.py, BELLO-core-more-folds-v1.py

BELLO-core automatically characterizes and extracts morphological values based on atomic structures which is then used to compute relevant statistical parameters for amorphous glass and liquid investigation. Initially, input file is read as a standard atomic trajectory, the file can either be a single or multiple snapshots (trajectory frames). Importing and exporting files are done by Pandas and Numpy libraries respectively as they make for a more structured and faster data handlings. User inputs include interatomic distance, interatomic distance tolerance, unit cell dimensions in X Y Z axis (axis are perpendicular to another by default ). Prior to any calculation, initial boundary condition is applied on the whole system, shifting all outer atoms inside unit cell Figure 4.1. a,b). Then, trajectory frames (if any) are sequentially differentiated by their position in the input file. After that, by reading the number of atoms in XYZ format's first line, the trajectories are separated from one another. Next, by recursive looping over all atoms and selecting them as the center of local order, distances to neighboring atoms are calculated and the ones within the defined range are selected as local order bonds. Figure 4.1.c illustrates the selection process in which an atom's image (neighboring unit cell) is closer to the central atom, thus, it is selected as a ligand . Number of ligands can vary between three for three folded geometries to six for octahedral, the rest are disregarded. After that, all relevant information about the extracted local order including bond angles, bonding atom types and atomic coordinates are collected for calculation purposes, Figure 4.1.d shows angle calculation processes with respect to the boundary condition, distance and angles are computed according to atom 2' (image of atom #2) even though atom #2 is saved in the outputs.

Collected information are used for characterizations and statistic computations, these parameters include:

#### 4.3.1.1 q-parameter

Quantifying short-range structural order in liquids and glasses is possible through computing q order parameter (equation.1). Where  $\theta_{ijk}$  is the angle formed between a central atom j and its neighboring atoms i and k. these values are then averaged over each frame and stored alongside the contributing individual values.

$$q = 1 - \frac{3}{8} \sum_{k>i} \left( \frac{1}{3} - \cos \theta_{ijk} \right)^2 \quad (4.1)$$

Measuring the tetrahedrlicity of atomic environments, q can distinguish different atomic geometries with 1 being the perfect tetrahedral and 0 for perfect octahedral. additionally, defective octahedral geometries are represented by values between 0 and 1, Figure 4.2 represents the ideal versions of these geometries with their corresponding q value. The module collectively reports



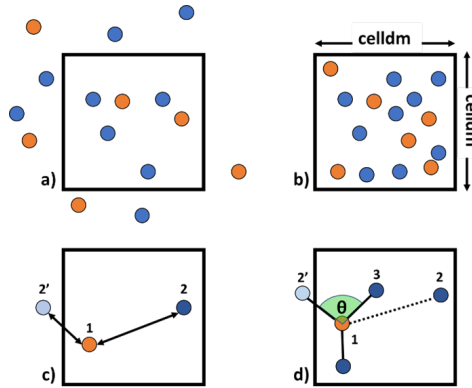


Figure 4.1: Schematic representation of the applied boundary conditions, trajectories with atoms outside of unitcell (a) are move inside (b). atomic distances between the central atom (#2) and the ligands (#2') are calculated considering the boundary condition. (d) shows angle calculation process between ligands.

total  $q$  parameter in one output file Figure 4.3 as well as discrete files for  $q$ 's contribution to each geometry Figure 4.4

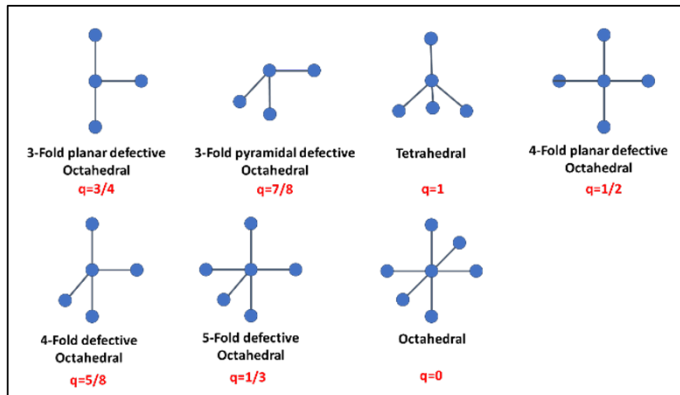


Figure 4.2: Local order geometries with their corresponding  $q$  values.

### 4.3.1.2 PDB

PDB (protein data bank) is a widely used database for the three-dimensional structural data, it contains unit cell data as well as grouped information about different configurations and can be read by many visualization softwares. In addition to the atom types and coordinates, local order type and number, and

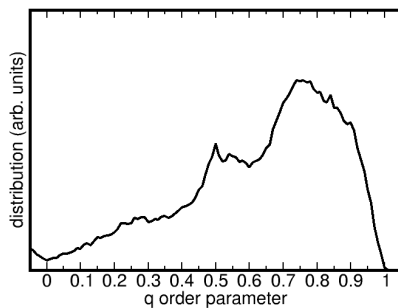


Figure 4.3: Total q value illustrated from total-q-output.

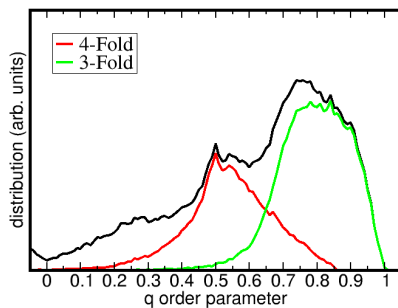


Figure 4.4: Local order geometries with their corresponding q values.

every atom's listing number in input are saved within PDB output. Figure 4.5 illustrates a 3D sample visualization from the module's PDB output. Ge and Te atoms are represented by Purple and yellow colors, respectively. Polyhedral information for all extracted geometries is saved within the file and can be viewed with visualization softwares.

### 4.3.1.3 Bond Angle Distribution Function

Bond angle distribution function (BADF) in addition to radial distribution function and the detailed coordination, significantly contributes to short-range order characterization. Thus bello-core-v1 extracts all bond angles between two ligands and the central atom in extracted local orders, making it a more tailored distribution. A sample output for the case of  $\text{Ge}_{54}\text{Te}_{216}\text{As}_{20}\text{Se}_{30}$  is presented in Figure 4.6, the distribution is for the angles between Te-Ge-Te bonds with Ge being the central atom and Te as ligands. additionally, angle-sorting.py module handles further BADF output processing. By reading the BADF output,

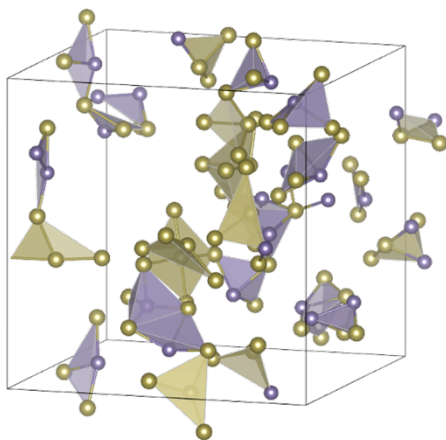


Figure 4.5: 3D visualization from PDB module's output for super-cell of chalcogenide  $\text{Ge}_{54}\text{Te}_{216}\text{As}_{20}\text{Se}_{30}$ .

the module discriminates and sorts bond angles with respect to their elements, resulting in multiple output files for each element combination.

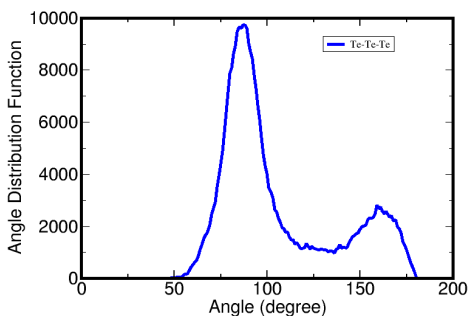


Figure 4.6: Bond angle distribution function of Te-Ge-Te from extracted local orders of crystalline  $\text{Ge}_{54}\text{Te}_{216}\text{As}_{20}\text{Se}_{30}$ .

#### 4.3.1.4 XYZ-Coordinates

atomic coordinates of the extracted geometries are saved in XYZ standard formatting. Duplicate atoms emerging from bond sharing between local orders are removed in the output file. Standard XYZ formatting is the most common format file amongst almost every visualization software.

### 4.3.1.5 Local-order-statistics

extracted geometry's population, categorized by the local order type and the containing frame are statistically reported in output-local-statistics.txt. local order population fluctuations throughout the trajectory frames can be seen from Figure 4.7, "total" value is the accumulative of all geometries. The second module (BELLO-core-more-folds-v1.py) has a similar functionality to BELLO-core with the addition of extracting more local orders (0-fold, 1-fold and 2-fold) which is especially useful while studying some amorphous systems.

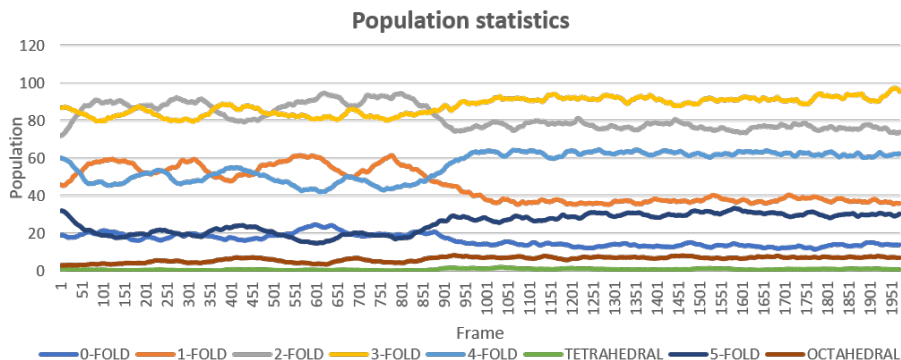


Figure 4.7: Local order population variations of extracted statistics corresponding to the trajectory frames. The plot belongs to molecular dynamics simulation from  $\text{Ge}_{54}\text{Te}_{216}\text{As}_{20}\text{Se}_{30}$ .

### 4.3.2 Module: Radial-Distribution-function.py

Quantitative description of internal structure of liquids and amorphous materials can be achieved via Radial Distribution Function  $g(r)$  (RDF). it quantifies how an atom of interest is surrounded by other atoms, in an ideal gas which has no internal structure, RDF yields a constant number while a crystalline solid with regularly located atoms, results in a sharply picked RDF at the position of atoms and is almost zero in between. Starting with the standard atomic structure trajectory as input file, RDF module takes advantage of python's Numpy, Pandas and Matplot standard libraries. user defines initial values such as atoms of interest (A and B), unit cell dimensions, maximum range and  $\Delta r$ . RDF module leverages from BELLO-core-v1's boundary condition algorithm, meaning, for each frame, interatomic distances between the defined elements are computed accounting for neighboring unit cells. Then, the conditional probability density of finding atom B at "r", given atom A is at the coordinate origin is computed by  $g(r)$  (eq.2)[2].

$$g(r) = \frac{V}{4\pi r^2 N^2} \left( \sum_i \sum_{j \neq i} \delta(r - r_{ij}) \right) \quad (4.2)$$

Where  $V$  is unit cell volume,  $N$  is the total number of atoms inside unit cell,  $i$  and  $j$  represent atom A and B respectively. Computed radial distribution function is then averaged over all frames and plotted in an external windows using matplotlib library Figure 4.8.

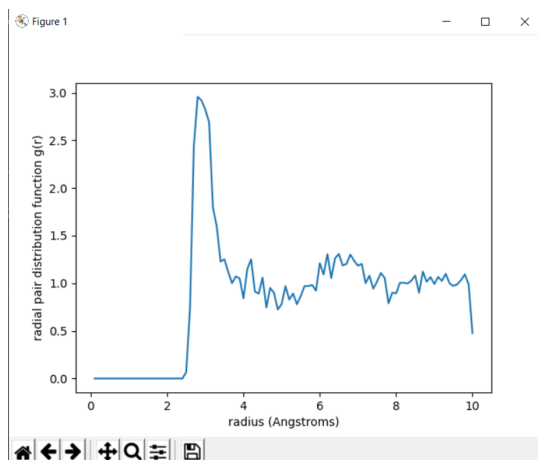


Figure 4.8: Output windows of matplotlib library depicting radial distribution function of GeTe4.

### 4.3.3 Module: Detailed-coordination-number.py

Coordination number, being the number of bonded atoms to a certain atom, represents a whole number for a coordination which can be further expanded. Detailed coordination number module discriminates central and ligand atom types and their population frequency, it is done by reading Output-human-readable.txt from BELLO-core-v1, user inputs include: three atom types to be distinguished and extracted (currently V1 supports maximum of 3 elements), if the desired output is less than three types, input fields can be either skipped (empty) or filled with irrelevant characters. By collecting local order types and the consisting atoms from input file, the module computes the percentage of each geometry with respect to all local orders. Additionally, within each geometry, contribution percentage of different element combinations to all local orders are extracted. Figure 4.9 represents a 2-element sample output of an amorphous GeTe4 structure. Separated by each element, the first row reports the contribution of the geometries. Accompanied rows are the present combinations within the local order with their percentages. Results with 0 value are not reported in this table. A 3D schematic of the highlighted geometries is illustrated

in Figure 4.9.a as a 3-Fold  $\text{GeTe}_2$  with Ge center and Figure 4.9.b as 4-Fold  $\text{Ge}_2\text{Te}_3$ .

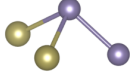
A schematic representation of BELLO’s work flow and modular dependency is presented in Figure II10. As can be seen, BELLO’s only input-file dependency is the trajectory file generated by ab-initio electronic structure calculations, then multiple output files for each statistical parameter are created which can be used for further calculations by the code.

	3-Fold	4-Fold	Tet.	5-Fold	Oct.
<b>Ge:</b>	75%	18.75%	0%	6.25%	0%
	<b>GeTe2:</b> 18.75%	<b>Te4:</b> 18.75%		<b>GeTe4:</b> 6.25%	
	<b>Te3:</b> 56.25%				
<b>Te:</b>	87%	12.10%	0%	3%	0%
	<b>Ge3:</b> 6.45%	<b>Ge2Te2:</b> 6.5%		<b>Ge2Te3:</b> 3%	
	<b>Ge2Te:</b> 16.1%	<b>GeTe3:</b> 6.5%			
	<b>GeTe2:</b> 29%				
	<b>Te3:</b> 35.5%				

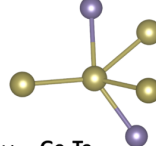
  

● Ge

● Te



a)  $\text{GeTe}_2$



b)  $\text{Ge}_2\text{Te}_3$

Figure 4.9: Detailed coordination number table of extracted geometries from  $\text{GeTe}_4$ . results with 0 value are not reported. (a)(b) illustrates the highlighted structures of local orders corresponding to (a)  $\text{GeTe}_2$  and (b)  $\text{Ge}_2\text{Te}_3$ .

## 4.4 Installation, input and Output structure

BELLO does not require any installation or specific setup given that the Python 3.7 as well as Numpy and Pandas libraries are installed on the system. BELLO-core-v1.py, BELLO-core-more-folds-v1.py and Radial-Distribution-function.py modules call the input file “traj.xyz”, the file should be in the same directory as the modules since the outputs will be generated there as well. Since other modules call BELLO-core’s outputs, no specific input file needs to be created for them.

### 4.4.1 Input file format

BELLO calls the input file in standard XYZ format, the file can either be a single snapshot or multiple trajectories. The structure of the input file “traj.xyz” of an MD simulation trajectory is illustrated in listing.1.

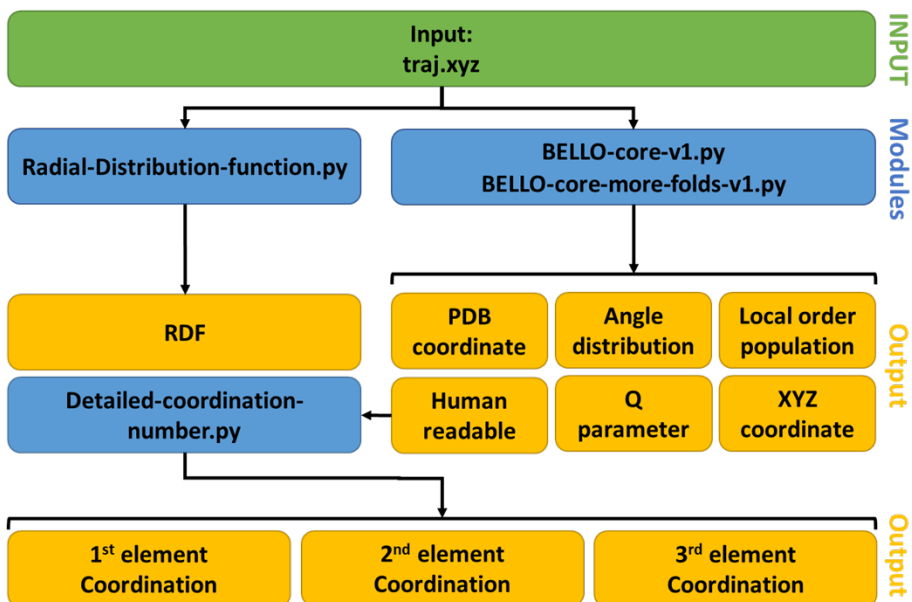


Figure 4.10: Graphic illustration of BELLO’s workflow starting from a single trajectory file. Detailed-coordination-number module takes advantage of the Human-readable output produced from BELLO-core to generate coordination number for three types of elements.

```

Listing 1: traj.xyz - file format
15
Ge      -0.940965    8.645859    -5.631683
Ge      7.781063    18.668819    16.983537
Ge      7.762954    -7.321926    11.319025
Ge     -10.993783    20.291725    5.086786
Ge     15.822496    18.291140    4.347558
Te     22.169233     0.911630    8.895549
Te     -1.112528     2.938022    3.353387
Te     -9.068296    15.097867    9.649382
Te     32.304161    13.109065    -0.249639
Te    -19.554041   -12.838981    7.135789
Te     3.066865    19.304098    6.651413
Te     17.697591    12.169512    -4.646699
Te     6.566489     1.375293    -1.197619
Te     0.900941     1.172735    11.431760
Te     5.787254     7.420000    29.475777

```

Figure 4.11: Listing 1

## 4.5 User Inputs

### 4.5.1 Module: BELLO-core-v1.py, BELLO-core-more-folds-v1.py

- trhld
  - Description. average interatomic distance threshold ( $r$ ).
  - type. Integer or Float. Default= 3.0.
  - Example. See listing 2.
  
- tlrc
  - Description. interatomic distance tolerance ( $\pm\Delta r$ ).
  - type. Integer or Float. Default= 0.1.
  - Example. See listing 2.
  
- celldmx, celldmy, celldmz
  - Description. X Y Z axis dimensions of unit cell in angstrom unit.
  - type. Integer or Float.
  - Example. See listing 2.

```
Listing 2: BELLO-core-/more-folds/-v1.py User input format
|-----|
|-----B.E.L.L.O-----|
|-----Bond Element Lattice Locality Order-----|
|-----|
|-----|
|-----|

filename should be traj.xyz
Input atomic distance threshold (Ang): 3.0
Input atomic distance tolerance (Ang): 0.1
X-axis lattice constant in Ang: 10
Y-axis lattice constant in Ang: 10
Z-axis lattice constant in Ang: 10
```

Figure 4.12: Listing 2

### 4.5.2 Module: Radial-Distribution-function.py

- fat
  - Description. First element to be set as the reference atom.
  - type. String (2 characters).
  - Example. See listing 3.
  
- sat
  - Description. The element that the distance should be calculated to.



- type. String (2 characters).
  - Example. See listing 3.
- rmax
    - Description. Maximum range of RDF calculation radius.
    - type. integer. Default= 10.
    - Example. See listing 3.
  - dr
    - Description. Intervals between radius shells ( $\Delta r$ ). typically, a number between 0 and 1, lower values mean more accuracy.
    - type. float. Default= 0.1.
    - Example. See listing 3.
  - celldmx, celldmy, celldmz
    - Description. X Y Z axis dimensions of unit cell in angstrom unit.
    - type. Integer or Float.
    - Example. See listing 3.

```

Listing 3: Radial-Distribution-Function.py User input format
|-----|
|-----B.E.L.L.O-----|
|-----Bond Element Lattice Locality Order-----|
|-----|
|-----Radial Pair Distribution Function-----|
X-axis lattice constant in Ang: 10
Y-axis lattice constant in Ang: 20
Z-axis lattice constant in Ang: 30
First element: Ge
Second element: Te
Maximum range(integer): 10
delta r: 0.1

```

Figure 4.13: Listing 3

### 4.5.3 Module: Detailed-coordination-number.py

- ele1, ele2, ele3
  - Description. Write elements to be characterized in local orders. (currently structures with three or less elements are supported). Skipping inputs can either be done by pressing “enter” or typing “XX”.
  - type. String (2 character).

-Example. See listing 4.

```
Listing 4: Detailed-coordination-number.py User input format
|-----|
|-----B.E.L.L.O-----|
|-----Bond Element Lattice Locality Order-----|
|-----|
|-----Detailed Coordination Number-----|
input Element #1: Ge
input Element #2: Te
input Element #3: Se
```

Figure 4.14: Listing 4

## 4.6 Module outputs

### 4.6.1 Module: BELLO-core-v1.py, BELLO-core-more-folds-v1.py

- output-/ q-total/ q3fl/ q4fl/ qtet/ q5fl/ q6fl.txt
  - Description. Order parameters q for all trajectories (q-total) and separated ones (q3fl, q4fl, etc.), each row represents the values for a snapshot.
  - type. Python list
  - Example. See listing 5.

```
Listing 5: output-q-total.txt output format
[0.53, 0.64, 0.62, 0.59, 0.8, 0.67, 0.76, 0.66, 0.52]
[0.84, 0.64, 0.62, 0.58, 0.8, 0.67, 0.65, 0.72, 0.88]
[0.63, 0.58, 0.8, 0.66, 0.81, 0.67, 0.4, 0.4, 0.65]
[0.78, 0.61, 0.76, 0.92, 0.63, 0.8, 0.75, 0.6, 0.66]
[0.79, 0.6, 0.75, 0.8, 0.87, 1.0, 0.83, 0.86, 0.71, 0.6]
[0.65, 0.33, 0.9, 0.73, 0.92, 0.33, 0.76, 0.64, 0.67]
```

Figure 4.15: Listing 5

- output-angle-distribution.txt
  - Description. Accumulated bond angle population of extracted local orders. The extra module “angle-sorting.py” will categorize distributions based on the atom types.
  - type. Python list
  - Example. See listing 6.
- output-local-statistics.txt
  - Description. Frame by frame (rows) statistics of extracted local orders.
  - type. Python list

```

Listing 6: output-angle-distribution.txt output format
79.030 Te-Ge-Te
168.262 Te-Ge-Te
90.032 Te-Ge-Te
86.176 Te-Ge-Te
90.746 Te-Ge-Te
84.223 Te-Ge-Te
64.567 Ge-Ge-Te
92.743 Te-Ge-Te
77.900 Ge-Ge-Te
65.920 Te-Ge-Te
151.126 Te-Ge-Te
85.656 Te-Ge-Te
61.334 Ge-Ge-Te
167.047 Te-Ge-Te
118.405 Ge-Ge-Te

```

Figure 4.16: Listing 6

-Example. See listing 7.

```

Listing 7: output-local-statistics.txt output format
3-FOLD 4-FOLD TETRAHEDRAL 5-FOLD OCTAHEDRAL Total
39      7      0          1          0      47
42      4      0          2          0      48
37      9      0          0          0      46
42      6      0          0          0      48
36      7      0          0          0      43

```

Figure 4.17: Listing 7

- output-pdb-coords.txt
  - Description. Collection of extracted geometries in PDB coordinates, first two lines are reserved for the header and the third line is the unit cell. Second columns report listing number of the specific atom in trajectory file. Frames are discriminated by the line “End of frame #”, with “#” being the frame number.
  - type. Python list
  - Example. See listing 8.

```

Listing 8: output-pdb-coords.txt output format
PDB coordinates
-----BELL0-----
CRYST1  20.644848  20.644848  20.644848  90.00  90.00  90.00 P1  1
ATOM    3  Ge  4FL  C  1    7.763 13.223 11.315  1.00  0.00  Ge00
ATOM   98  Te  4FL  C  1   10.706 12.467 11.182  1.00  0.00  Te00
ATOM   73  Te  4FL  C  1    9.170 16.091 10.881  1.00  0.00  Te00
ATOM   144 Te  4FL  C  1    6.887 10.291 11.506  1.00  0.00  Te00
ATOM   236 Te  4FL  C  1    7.692 12.829  8.260  1.00  0.00  Te00
ATOM    4  Ge  3FL  A  2    9.651 20.292  5.087  1.00  0.00  Ge00
ATOM   23  Ge  3FL  A  2   10.752 17.748  4.045  1.00  0.00  Ge00
ATOM   214 Te  3FL  A  2    8.239 19.159  2.782  1.00  0.00  Te00
ATOM   235 Te  3FL  A  2   11.898  0.579  3.432  1.00  0.00  Te00
ATOM   13  Ge  3FL  A  3    6.566  1.375 19.447  1.00  0.00  Ge00
ATOM   89  Te  3FL  A  3    9.299  0.163 19.984  1.00  0.00  Te00
End of frame 0
ATOM    3  Ge  3FL  A  1    7.801 13.232 11.305  1.00  0.00  Ge00
ATOM   98  Te  3FL  A  1   10.694 12.498 11.181  1.00  0.00  Te00
ATOM   236 Te  3FL  A  1    7.701 12.828  8.274  1.00  0.00  Te00
ATOM   241  Te  3FL  A  1    5.140 12.956 12.526  1.00  0.00  Te00
ATOM    4  Ge  3FL  A  2    9.685 20.275  5.090  1.00  0.00  Ge00
ATOM   23  Ge  3FL  A  2   10.757 17.717  4.036  1.00  0.00  Ge00
ATOM   214 Te  3FL  A  2    8.243 19.111  2.778  1.00  0.00  Te00
ATOM   235 Te  3FL  A  2   11.893  0.568  3.464  1.00  0.00  Te00
ATOM   13  Ge  3FL  A  3    6.570  1.391 19.467  1.00  0.00  Ge00

```

Figure 4.18: Listing 8

- output-xyz-coords.txt
  - Description. Collection of extracted geometries in standard XYZ coordinates. Frames are discriminated by the line “End of frame #”, with “#” being the frame number.
  - type. Python list
  - Example. See listing 9.

```

Listing 9: output-xyz-coords.txt output format
Ge 7.762954 13.322922284633 11.319025
Te 10.705732715366999 12.466542 11.181861999999999
Te 9.170264284633 16.091110999999999 10.881241000000001
Te 6.887399 10.290699 11.506095
Te 7.692244000000005 12.829288 8.259656715367
Ge 9.651065284632999 20.291725 5.086786
Ge 10.751939 17.747941284633 4.045448715367002
Te 8.238856 19.159036999999998 2.7815207153670016
Te 11.897616000000001 0.578861 3.4316190000000004
Ge 6.566489 1.375293 19.447229284633
Te 9.299348 0.16330071536700075 19.983515284633
Te 8.382021 1.262304 16.99519
Te 5.90308799999999994 0.594719715366999 1.762893
Ge 15.757987 1.1441437153670009 13.656444
Ge 18.249854 1.229382 15.359584284633
Te 15.470567284632999 1.0649907153670028 16.47664839

End of frame 0

Te 16.045014000000002 0.558938 10.77093
Ge 2.326602 3.066079 16.870125
Te 0.7592260000000001 2.614155 14.421851284633

```

Figure 4.19: Listing 9

- output-human-readable-coords.txt
  - Description. A summarized human readable description of all the extracted parameters.
  - type. Python list
  - Example. See listing 10.

```

Listing 10: output-human-readable-coords.txt output format
4-FOLD - q is: 0.5377475399918501
Te 0.36811271536699763 4.753806 7.505930715366997
Te 1.3909559999999999 3.4732199999999995 10.11999
Ge 1.090807284632998 7.805867284632999 7.135789
Te 17.876057 4.500368 7.088508999999999
Te 19.173180284633 5.701999 9.664308

3-FOLD - q is: 0.6197467322920007
Te 7.977861715366998 19.385447 14.016097
Ge 7.7810630000000005 18.668819 16.983537
Ge 10.10042 18.668542284633 11.874239999999999
Te 6.327874715366999 16.939925 13.486948000000002

End of frame 0

Number of 3-FOLD, 4-FOLD, TETRAHEDRAL, 5-FOLD,
OCTAHEDRAL: 1, 1, 0, 0, 0

Number of local orders are: 2

```

Figure 4.20: Listing 10

## 4.6.2 Module: Radial-Distribution-function.py

- RDF.txt
  - Description. Computed radial distribution function vs atomic radius.
  - type. Python list
  - Example. See listing 11.

```
Listing 11: RDF.txt output format
0.1 0.0
0.3 0.0
0.5 0.0
0.7 0.0
0.9 0.0
1.1 0.0
1.3 0.0
1.5 0.0
1.7 0.0
1.9 0.0
2.1 0.0
2.3 0.0
2.5 0.06521202835198883
2.7 2.436944419829218
2.9 2.9208704128369716
3.1 2.6900273893722564
3.3 1.597070394049982
3.5 1.2516177333503355
3.7 1.0002569648964783
3.9 1.0500852263922926
```

Figure 4.21: Listing 11

## 4.6.3 Module: Detailed-coordination-number.py

- • D-coordination-number-XX.txt
  - Description.  $XX^{th}$  element coordination with “XX” being the described element. writes a table of element contribution percentage for each geometry. First row describes local order’s different element combinations and consecutive rows represent a snapshot.
  - type. Python list
  - Example. See listing 12.

```
Listing 12: D-coordination-number.txt output format
3-Fold_XX, ..., 4-Fold_XX, ..., Tet_XX, ..., 5-Fold_XX, ..., Oct_XX, ...
65.0, ..., 2.46, ..., 4.54, ..., 10.2, ..., 19.8, ...
61.0, ..., 4.5, ..., 4.5, ..., 12, ..., 19, ...
67.0, ..., 1.43, ..., 5.04, ..., 11.5, ..., 17.3, ...
60.45, ..., 3.5, ..., 6.5, ..., 9.55, ..., 20, ...

[3-E1_0-E2_0-E3, 2-E1_1-E2_0-E3, 1-E1_2-E2_0-E3, 0-E1_3-E2_0-E3, ...]
↓
[2-atoms of element#1 and 1-atom of element#2 and 0-atoms of element#3]
↓
Example:
If:          Then:
element#1= Ge          Ge,Te
element#2= Te
Element#3= Se
```

Figure 4.22: Listing 12

## 4.7 Conclusion

By introducing BELLO we provided a post-processing script-tool created for the automatic analysis and extraction of structural characteristics of disordered and amorphous systems. The modular nature and the flexibility of the code makes it a great tool for the community to use in different ways. We hope by contributing this code, we will witness it's applications in modern material researches and developments.

## References

- [1] Zhu, Jia et al. "Optical Absorption Enhancement in Amorphous Silicon Nanowire and Nanocone Arrays". In: *Nano Lett.* vol. 9, no. 1 (Jan. 2009), pp. 279–282.
- [2] Jia Zhu, Ching-Mei Hsu Zongfu Yu Shanhui Fan and Cui, Yi. "Nanodome Solar Cells with Efficient Light Management and Self-Cleaning". In: *Nano Lett.* vol. 10 (May 2010), pp. 1–6.
- [3] Gai, Xin, Choi, Duk-Yong, and Luther-Davies, Barry. "Negligible nonlinear absorption in hydrogenated amorphous silicon at  $155\mu\text{m}$  for ultra-fast nonlinear signal processing". In: *Optics Exp.* vol. 22, no. 8 (2014), pp. 9948–11.
- [4] Nomura, K. et al. "Room-temperature fabrication of transparent flexible thin-film transistors using amorphous oxide semiconductors". In: *Nature* vol. 432 (Nov. 2004), pp. 488–492.
- [5] Kamiya, T., Nomura, K., and Hosono, H. "Present status of amorphous In-Ga-Zn-O thin-film transistors". In: *Sci. Tech. Adv. Mater.* vol. 11, no. 4 (2010), p. 044305.
- [6] Kuzyk, Mark. G. *Polymer Fiber Optics*. Boca Raton FL, USA: CRC Press, Taylor & Francis Group, 2007.
- [7] Peters, Kara. "Polymer optical fiber sensors—a review". In: *Smart Mater. Strct.* vol. 20 (Dec. 2010), p. 013002.
- [8] Ohta, T. "Phase-change optical memory promotes the DVD optical disk". In: *J. Opt. Adv. Mater.* vol. 3, no. 3 (2001), pp. 609–626.
- [9] Wuttig, M. and Yamada, N. "Phase-change materials for rewriteable data storage". In: *Nature Mater.* vol. 6, no. 11 (2009), pp. 824–832.
- [10] Burr, G. W. et al. "Phase change memory technology". In: *J. Vac. Sci. Tech. B* vol. 28, no. 2 (2010), pp. 223–262.
- [11] Thouless, David J. "Electrons in Disordered Systems and the Theory of Localization". In: *Phys. Rep.* vol. 13, no. 3 (1974), pp. 93–142.
- [12] Häußler, P. "Interrelations between atomic and electronic structures—Liquid and amorphous metals as model systems". In: *Phys. Rep.* vol. 222, no. 2 (Dec. 1992), pp. 65–143.

- [13] Ovshinsky, S. R. and Adler, D. “Local structure, bonding, and electric properties of covalent amorphous semiconductors”. In: *Contemp. Phys.* vol. 19 (1978), pp. 109–126.
- [14] Popescu, Mihai. *Structure, Defects and Electronic Properties of Amorphous Semiconductors*. Weinheim, Germany: John Wiley & Sons, Ltd, June 2003.
- [15] Steinhardt, Paul J, Nelson, David R, and Ronchetti, Marco. “Bond-orientational order in liquids and glasses”. In: *Phys. Rev. B* vol. 28, no. 2 (July 1983), pp. 784–805.
- [16] Stachurski, Zbigniew H. “On Structure and Properties of Amorphous Materials”. In: *Materials* vol. 4, no. 9 (Sept. 2011), pp. 1564–1598.
- [17] Moorjani, Kishin and Feldman, Charles. “Electrical Properties of Amorphous Semiconductors”. In: *Rev. Mod. Phys.* vol. 36, no. 4 (Oct. 1964), pp. 1042–1049.
- [18] Adler, David, Henisch, Heinz K, and Mott, Sir Nevill. “The mechanism of threshold switching in amorphous alloys”. In: *Rev. Mod. Phys.* vol. 50, no. 2 (Apr. 1978), pp. 209–220.
- [19] Alexander, Shlomo. “Amorphous solids: their structure, lattice dynamics and elasticity”. In: *Phys. Rep.* vol. 296, no. 2-4 (Mar. 1998), pp. 65–236.
- [20] Stillinger, Frank H. “Supercooled liquids, glass transitions, and the Kauzmann paradox”. In: *J. Chem. Phys.* vol. 88, no. 1 (June 1988), pp. 7818–7825.
- [21] Berthier, Ludovic and Biroli, Giulio. “Theoretical perspective on the glass transition and amorphous materials”. In: *Rev. Mod. Phys.* vol. 83, no. 2 (June 2011), pp. 587–645.
- [22] Greaves, G. N. and Sen, S. “Inorganic glasses, glass-forming liquids and amorphizing solids”. In: *Adv. Phys.* vol. 56 (2007), pp. 1–166.
- [23] M.Vaccari et al. “High pressure transition in amorphous  $\text{As}_2\text{S}_3$  studied by EXAFS”. In: *J. Chem. Phys.* vol. 131 (2009), p. 224502.
- [24] Yannopoulos, S. N. and Andrikopoulos, K. S. “Raman scattering study on structural and dynamical features of noncrystalline selenium”. In: *J. Chem. Phys.* vol. 121 (2004), pp. 4747–4758.
- [25] Böhmer, R. et al. “Dynamics of supercooled liquids and glassy solids”. In: *Progr. Nucl. Magn. Res. Spec.* vol. 39 (2001), pp. 191–267.





## Chapter 5

# Hierarchical short- and medium-range order structures in amorphous $\text{Ge}_x\text{Se}_{1-x}$ for selectors applications

### Abstract

In the upcoming process to overcome the limitations of the standard von Neumann architecture, synaptic electronics is gaining a primary role for the development of in-memory computing. In this field, Ge-based compounds have been proposed as switching materials for nonvolatile memory devices and for selectors. By employing the classical molecular dynamics, we study the structural features of both the liquid states at 1500 K and the amorphous phase at 300 K of Ge-rich and Se-rich chalcogenides binary  $\text{Ge}_x\text{Se}_{1-x}$  systems in the range  $0.4 < x < 0.6$ . The simulations rely on a model of interatomic potentials where ions interact through steric repulsion, as well as Coulomb and charge-dipole interactions given by the large electronic polarizability of Se ions. Our results indicate the formation of temperature-dependent hierarchical structures with short-range local orders and medium-range structures, which vary with the Ge content. Our work demonstrates that nanosecond-long simulations, not accessible via ab initio techniques, are required to obtain a realistic amorphous phase from the melt. Our classical molecular dynamics simulations are able to describe the profound structural differences between the melt and the glassy structures of GeSe chalcogenides. These results open to the understanding of the interplay between chemical composition, atomic structure, and electrical properties in switching materials.

### Contents

5.1	Introduction . . . . .	64
5.2	Methods . . . . .	66
5.3	Results and Discussion . . . . .	67
5.4	Conclusion . . . . .	76
5.5	Associated content . . . . .	77
	References . . . . .	77

## 5.1 Introduction

A radical alternative to the existing scaling issues of Si-based technology relies on new disrupting solutions commonly referred as in-memory computing, where data are processed directly within the memory element integrated in the back end of line (BEOL).[1] Among the novel technologies that are being explored, the class of emerging memory devices or storage class memories (SCMs), such as resistive switching memory (RRAM),[2] phase change memory (PCM),[3] and spin transfer torque memory (STTRAM),[4] is the most promising. This new class of memory technology has performance characteristics that fall between DRAM and flash characteristics, and it bridges the latency gap between server storage and external storage. These devices have key characteristics, such as full compatibility with the CMOS technology, simple geometry, low-power operations, and scalability beyond the 10 nm node.[5] SCMs are in complex memory cells,[6] which include three dimensional (3D) cross-point arrays of switching memories interconnected by selectors, which control the accessibility and quality of data transmission within and outside the entire cell.[7] Selectors are dynamical switches to the encoding mode with a possible lowest bit error rate, which suppresses the unselected shunt path for the leakage current in large (Gbit) arrays.[8] Selectors control the cell-to-cell write/read programming and allow for the realization of high-density crossbar memory array with  $4F^2$  cell. The ovonic threshold switching (OTS) selector technology showed the capability to overcome key issues with performance degradation over time, providing high endurance and a high ON/OFF current ratio ( $I_{ON}/I_{OFF}$ ) required for crossbar applications.[9] [10]The general OTS mechanism in amorphous chalcogenide materials is known[11] and consists of a volatile switch between a high resistive state (OFF state) and a low resistive state (ON state) when the voltage applied to the material exceeds a critical voltage, called threshold voltage  $V_{th}$ . However, the detailed interplay between the parameters that characterize the materials (e.g., structure, composition, doping, and chemical and thermal stabilities) and the influence they have on the device characteristics (e.g., data retention, power consumption, and switching time) has not been completely understood. Amorphous chalcogenides such as  $Ge_xSe_{1-x}$  compounds have been proposed as ovonic switching materials[12] for both nonvolatile memory devices and selectors,[13] in view of their high ON-state drive current, good half-bias linearity, fast switching, endurance, and a higher crystallization temperature with respect to, e.g., GST or GeSbSeTe materials.[14] First experimental evidences indicate that the modulation of the stoichiometry ratio affects the electrical response of the device,

in terms of both I-V characteristics and power dissipation.[15] In particular, devices based on Ge-rich GeSe compounds exhibit a high OFF current and a low threshold voltage,[16][17] while Se-rich GeSe-based devices have a higher energy gap, a lower OFF-state leakage current, and a higher thermal stability.10 The origin of this behavior is still unknown: while much effort has been dedicated to GeTe as a prototypical phase change material, or to GeSe2 as an efficient opto-electronic system, very little is known on quasi-stoichiometric  $Ge_xSe_{1-x}$  compounds. In analogy with other chalcogenide systems, it is

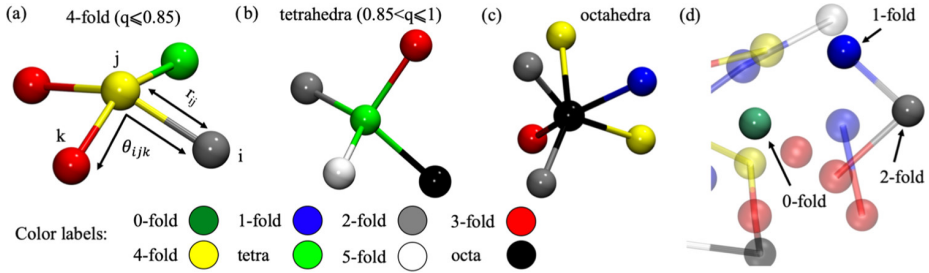


Figure 5.1: Sample of configurations of (a) 4-fold, (b) tetrahedral, and (c) octahedral structures. (d) The 0-fold, 1-fold, and 2-fold atoms with respective connections scheme rendered as solid spheres, while the neighboring atoms as transparent ones. Color codes for all folds are given at the bottom.

expected that the characteristics of  $\text{Ge}_x\text{Se}_{1-x}$  mobility gap and the presence of gap states are related to under-/overcoordinated Ge atoms[14][15] and to the ratio of homopolar/heteropolar bonds in the sample.[12] On the experimental side, neutron or Xray measurements only give statistical averages of the structures with a lack of description of the coordination path at the atomistic level. On the theoretical side, unraveling the interplay between chemical composition, local-order structures, trap states, and the resulting electrical response is a major challenge that requires the capability of treating large systems at the atomistic level along with their electronic structure. The prerequisite to this analysis is the identification of reliable atomic structures of the amorphous solid-state phase at room temperature. However, to date, no univocal determination of structural properties of  $\text{Ge}_x\text{Se}_{1-x}$  is available. Most previous experimental and computational studies dealt with  $\text{GeSe}_2$  in both liquid and glass phases.[18][19] In the case of  $\text{Ge}_x\text{Se}_{1-x}$ , only studies on the liquid phase at high temperatures ( $>700$  K) have been conducted, and no results are available for the amorphous solid phase at room temperature, especially for Ge-rich systems. The interpretation of the liquid  $\text{Ge}_x\text{Se}_{1-x}$  is also nontrivial, as no experiment or computer study was able to yield a definitive structure. A few quantum-mechanical models of amorphous  $\text{GeSe}$  and  $\text{GeSe}_2$  systems exist,[20][21][22] but are plagued by the severe computational costs that limit the size and the duration of the simulations. In this regard, the time required for reliable melting-and-quenching annealing cycles ( $>20$  ns) necessary to generate the amorphous glasses is usually not accessible to first-principles simulations. In this paper, we investigate the structure of  $\text{Ge}_x\text{Se}_{1-x}$  systems in the range  $0.4 < x < 0.6$ , using classical molecular dynamics (MD) simulations. The use of classical MD increases the possibility to study extended systems with thousands of atoms for several nanoseconds, which allows for medium-range spatial-order organization. Our results indicate a clear effect of the stoichiometry in the formation of hierarchical short-range local structures and medium-range connectivity networks in large-scale amorphous models in

both melt (high temperature) and glass (room temperature) phases. These are expected to play a crucial role in the definition of the mobility gap of the materials and their electrical response, thus explaining the differences observed experimentally in Ge-rich and Se-rich GeSe-based devices. The present analysis may also guide the identification of smaller but realistic models to be used in first-principles simulations, which are mandatory to correlate the complex structure of amorphous glasses with the corresponding electronic structure.

## 5.2 Methods

### 5.2.1 computational Details

The  $\text{Ge}_x\text{Se}_{1-x}$  systems have been built starting from the crystal structure of GeSe obtained from the Crystallography Open Database (COD), code: 4003515.[23] The Ge50Se50 initial structure has been built by replicating the unit cell 12, 4, and 12 times along the X, Y, and Z directions, respectively, to obtain a system made by 4608 atoms with a density in the order of 5.5 g/cm<sup>3</sup>. The  $\text{Ge}_{0.4}\text{Se}_{0.6}$  and  $\text{Ge}_{0.6}\text{Se}_{0.4}$  systems have been built by substituting a proper number of atoms to obtain the correct stoichiometry. To simulate the correct amorphous structure, the density of the systems has been decreased by 8% with respect to the corresponding crystal phase, as reported for the density of GeSe<sub>2</sub> and  $\text{Ge}_x\text{Se}_{1-x}$ . [24][25] For a comparison of the density of  $\text{Ge}_{0.5}\text{Se}_{0.5}$ , we performed an ab initio simulation at 1200 K with variable cell dimensions coupled within the Parrinello-Rahman approach and with the Nose-Hoover thermostat switched on electrons and ions obtaining a density in the order of 5.28 g/cm<sup>3</sup>, consistent with our thesis. The systems with glass density have been melted at 1500 K for 10 ns to have a liquid phase and to let the systems lose the memory of the initial configuration. Then, the temperature has been gradually decreased to 300 K with a cooling rate of 5 K/ps, which is a good compromise to keep a quite low computational cost and to avoid freezing effects that can alter the medium-range structures. After quenching, a production run has been conducted at 300 K for 50 ns. Simulations have been performed on an NVT ensemble with a Nose-Hoover thermostat with a characteristic time of 10 fs, and the MD timestep was taken to be 1 fs. Simulations have been performed using the LAMMPS package.[26] The force field (FF) employed is obtained customizing the wellknown potential of Vashishta et al.[24][27][28] for GeSe<sub>2</sub> to the case of  $\text{Ge}_x\text{Se}_{1-x}$ . The Vashishta FF has already been used to describe the structural features of several systems such as Ag<sub>2</sub>Se,[29] Ag/Ge/Se,[30] AlN,[31] SiO<sub>2</sub>,[32][33] and GaAs[34][35] with good accuracy; although ab initio molecular dynamics (AIMD) simulations provide higher accuracy, large systems and long simulation times as those required in this study are not accessible via AIMD.

### 5.2.2 Structural Analysis

The radial distribution function  $g(r)$  and the Faber-Ziman structure factor  $S_n(q)$  have been computed in the last 5 ns of the simulation at 1500 K for the

melt and in the last 15 ns at 300 K for the amorphous phase. The melting temperature for  $\text{Ge}_{0.33}\text{Se}_{0.67}$  and  $\text{Ge}_{0.5}\text{Se}_{0.5}$  is just above 1000 K, while the glass-transition temperature for  $\text{Ge}_{0.4}\text{Se}_{0.6}$  at around 350 K; [28] thus, the high and low temperatures considered in the analysis are well representative of the melt and glassy states, respectively. The number of atoms bound to a central atom (i.e., the fold) has been computed with a cutoff distance of 3.0 Å and a tolerance of 0.2 Å using an in-house code called BELLO. For example, a 2-fold atom is an atom bound to the other two atoms that lie within 3.0 Å, while a 5-fold has five neighboring atoms at less than 3.0 Å. Special cases are the 0-fold, which means that an atom is not bound to any other atom, and the 1-fold, where the atom is connected only to another atom, for example, at the end of a chain. The difference between tetrahedral and 4-fold atoms is given by the local-order parameter  $q$  [36][37].

$$q = 1 - \frac{3}{8} \sum_{k>i} \left( \frac{1}{3} - \cos \theta_{ijk} \right)^2 \quad (5.1)$$

where  $\theta_{ijk}$  is the angle formed by atoms  $ijk$ , with  $j$  the central atom. The local-order parameter can assume values from 1, i.e., a perfect tetrahedral network, to 0, i.e., a 6-fold octahedral network. We have chosen a range for  $q$  values from 1 to 0.85 to describe the tetrahedral fold (high bond order) and from 0.85 to 0 for the generic 4-fold (low bond order); see Figure 5.1. The ring statistics has been computed using the R.I.N.G.S. code40 with the King’s criterion, which defines a ring as the shortest path connecting a number of atoms or nodes.[38]

## 5.3 Results and Discussion

### 5.3.1 Short-Range Order

The radial distribution function is obtained directly from MD simulations, and it is used to analyze the two-body structural correlations. Figure 5.2 shows the radial distribution function,  $g(r)$ , for the amorphous phase at 300 K of  $\text{Ge}_x\text{Se}_{1-x}$ . All previous experimental and theoretical studies dealt with either liquid and amorphous phases[18][39][40] in the case of  $\text{GeSe}_2$  or liquid phase [19, 21, 22] in the case of  $\text{Ge}_{0.5}\text{Se}_{0.5}$ ,

while no results are available for the room-temperature amorphous structure of  $\text{Ge}_x\text{Se}_{1-x}$  systems in the range of  $0.4 < x < 0.6$ , that are used in selector devices. In this work, we used previous results of the  $g(r)$  of the liquid  $\text{Ge}_{0.5}\text{Se}_{0.5}$  as a benchmark for the validation of our force field [41] The Se-rich system considered here ( $\text{Ge}_{0.4}\text{Se}_{0.6}$ ) has a composition close to  $\text{GeSe}_2$  (i.e.,  $\text{Ge}_{0.33}\text{Se}_{0.67}$ ). The resulting Ge-Se and Se-Se  $g(r)$ ’s of the melt phase show behavior similar to the previously published results[18][42] for  $\text{GeSe}_2$  with primary peaks at 2.6 and 4.0 Å, respectively. A similar trend has been observed for both  $\text{Ge}_{0.5}\text{Se}_{0.5}$  and  $\text{Ge}_{0.6}\text{Se}_{0.4}$  liquid phases for Ge-Se and Se-Se bonds. The Ge-Ge  $g(r)$  for the liquid  $\text{Ge}_{0.4}\text{Se}_{0.6}$  has a single main peak located at 4.2 Å, without the presence of the first small peak at around 2.5 Å that can be observed in ab initio simulation studies.[22][43] This difference can be ascribed to the different

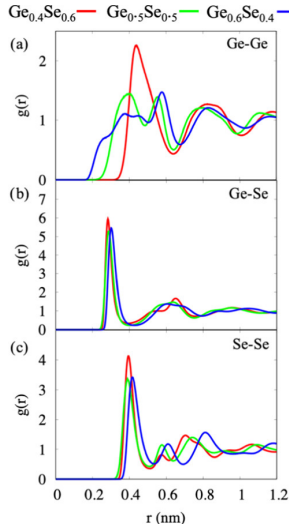


Figure 5.2: Radial distribution function,  $g(r)$ , for the amorphous phase at 300 K for each  $\text{Ge}_x\text{Se}_{1-x}$  system: (a) Ge-Ge, (b) Ge-Se, and (c) Se-Se interactions.

level of resolution of classical MD with respect to ab initio MD and to the corresponding different time scales. On increasing the Ge content to 50%, the main peak splits into two with maximum located at 4.1 and 5.35 Å with a wider distribution. On increasing the Ge content to 60%, we observed the formation of a new peak at 2.2 Å, which is close to the Ge-Ge distance of 2.4 Å in the crystal phase. This trend has been observed in particular for the liquid phase using both computational and experimental approaches,[19][22][43] where the  $g(r)$  of the melt shows two peaks at 2.5 and 4 Å, but at lower temperatures [19]. In particular, the work of Raty et al.[43] showed a quite different behavior of the  $g(r)$  of Ge-Ge going from 1053 to 1000 K, while the work of van Roon et al.[22] showed a marked difference between the experimental and computational  $g(r)$ 's of Ge-Ge at the liquid phase. The high structural difference for a- $\text{Ge}_x\text{Se}_{1-x}$  with  $x > 0.5$  with respect to  $x = 0.4$  well agrees with the experimental FIR and Raman measurements by Trodahl.[44] We conclude that our FF well reproduces the structural features of the existing systems in the liquid phase. In the amorphous phase at room temperature, the  $g(r)$  peaks appear more sharp and well defined with respect to the melt due to the lower mobility of atoms and to the increased structuring, as shown in Figure 5.2. For each stoichiometry, the position and width of the Ge-Se and Se-Se peaks remain almost unaltered, while the secondary peaks are found to be concentration-dependent. The case of Ge-Ge interactions is more complex. The 10% increased Ge content from the  $\text{Ge}_{0.4}\text{Se}_{0.6}$  to the  $\text{Ge}_{0.5}\text{Se}_{0.5}$  case results in the loss of a marked peak along with the formation of two peaks at 4.0 and 5.5 Å, as seen for the melt phase, but with a higher intensity. For  $\text{Ge}_{0.6}\text{Se}_{0.4}$ , the distribution is centered at around 3.76 Å, with

a marked secondary peak at  $5.7 \text{ \AA}$ . The shift of these distributions to smaller radii when increasing the Ge content is consistent with the values of pure Ge systems where the average Ge-Ge distance is  $2.4 \text{ \AA}$ . [45] Moreover, all three systems show a marked propensity for heteropolar Ge-Se bonds, while Ge-Ge and Se-Se are disfavored. The integration over the first peak of the  $g(r)$  gives the coordination number of each chemical species contributing to the different peaks in the  $g(r)$ . By averaging the elemental coordination number times their relative concentrations, it is possible to obtain the mean coordination number (MCN) of the system, which is relevant to empirically identify the rigidity of the chalcogenide glass: a floppy-to-rigid transition in chalcogenides is found for MCN values of 2.4; values between 2.4 and 2.65 indicate that systems are characterized by flexible segments with a layer-like structure. [46] In the present case and assuming Ge atoms four-coordinated and Se atoms two-coordinated, the MCN ranges from 2.8 for  $\text{Ge}_{0.4}\text{Se}_{0.6}$  to 3.2 for  $\text{Ge}_{0.6}\text{Se}_{0.4}$  and indicates a 3D “stressedrigid” phase. [46] The MCNs computed from our simulations are really close to the values predicted by the empirical law for  $\text{Ge}_{0.4}\text{Se}_{0.6}$  and  $\text{Ge}_{0.6}\text{Se}_{0.4}$  (2.80 and 3.04, respectively), while for  $\text{Ge}_{0.5}\text{Se}_{0.5}$ , the MCN computed from simulations is slightly higher (3.56) than the theoretical value of 3 Figure 5.3

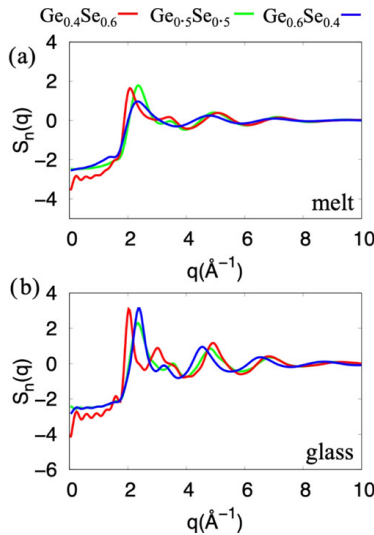


Figure 5.3: Faber-Ziman total static structure factors for melt (a) and amorphous (b) phases. Each composition is represented with a different color as shown in the legend above.

shows the results of the total neutron static structure factor  $S_n(q)$  in the melt and amorphous phase. The first sharp diffraction peak (FSDP) in the melt phase for  $\text{Ge}_{0.4}\text{Se}_{0.6}$  is located at  $2.0 \text{ \AA}^{-1}$ , with a second small peak at  $3.4 \text{ \AA}^{-1}$ ; these values are close to the values obtained for GeSe2. [27] [47] In the case of melt  $\text{Ge}_{0.5}\text{Se}_{0.5}$ , the FSDP is at  $2.34 \text{ \AA}^{-1}$  with a small peak at  $3.4 \text{ \AA}^{-1}$  and a

minimum at  $4.0 \text{ \AA}^{-1}$ . These values are very close to those obtained both by spectrometry analysis and ab initio simulations and by Raty et al.[45] and Le Roux et al.[21] for liquid GeSe. In the amorphous phase, the FSDPs are much higher, due to the higher structuring of the systems, and the position of the first peaks is similar to that of the melt phase. The height of the peaks in the glassy state is slightly larger than that in the molten phase, as previously shown for GeSe2.[24] At high temperatures, the partial correlation function on  $S_n(q)$  of Ge-Se has a minimum at  $1.8 \text{ \AA}^{-1}$  together with a peak at  $2.3 \text{ \AA}^{-1}$ , while in the case of Se-Se, the FSDP is at  $1.8 \text{ \AA}^{-1}$ . These values are close to those obtained by both experiment and computer simulation studies on liquid GeSe.[21][22][48] Previous studies on the liquid  $\text{Ge}_{0.5}\text{Se}_{0.5}$  system for Ge-Ge  $S_n(q)$  showed a peak at around  $1.7 \text{ \AA}^{-1}$ , but the curve is more flat with respect to the others and also to ab initio simulations, whose results depend on the choice of the exchange-correlation functional.[21][22][43][48] The Ge-Ge interactions in the liquid reported in Figure 5.4.a show a marked peak at  $1.7 \text{ \AA}^{-1}$  with a trend similar to those previously obtained, confirming the good accuracy of the force field employed.

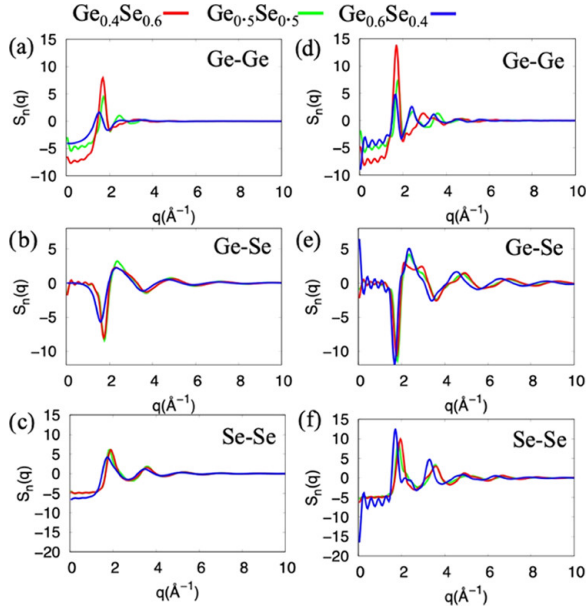


Figure 5.4: Faber-Ziman partial static structure factors for melt (right) and amorphous (left) phases. Each composition is represented with a different color, as shown in the legend at the top. (a, d) Ge-Ge  $S_n(k)$ , (b, e) Ge-Se  $S_n(k)$ , (c, f) Se-Se  $S_n(k)$ .

For all of the amorphous phases, the FSDP has the same position as in the liquid phase, but the peaks are more pronounced, and the curve shapes change with stoichiometry. The most appreciable differences can be observed on  $S_n(q)$  of Ge-Ge where the increase in the Ge content corresponds to decreasing FSDP



height. In a similar way, the secondary peak shifts to smaller values of  $q$ , as shown in Figure 5.4.d. From the intensities of the FSDP curves reported in Figure 5.4, it results that the main contribution to the total  $S_n(q)$  is given by Ge-Ge interactions for amorphous  $\text{Ge}_{0.5}\text{Se}_{0.5}$ , while in the other systems, the Se-Se interaction is predominant.

### 5.3.2 Local Order

The understanding of local-order structures in terms of folding, composition, and temperature evolution is of fundamental relevance in the design of materials for more efficient selectors. Local spatial order in chalcogenides is expected to be closely related to their electronic properties. [39][49][50] Raty et al.[43] showed that midgap states are caused by Ge-Ge homopolar bonds of tetrahedral Ge, while Zipoli et al.[51] suggested that clustering of undercoordinated or overcoordinated Ge atoms is associated with midgap states. Moreover, it has been suggested that Ge-Ge chains in a crystalline-like environment produce midgap states [52] and that high-ordered structures, such as close but not-bound high-fold Ge atoms, are associated with the localization of midgap states.[53]

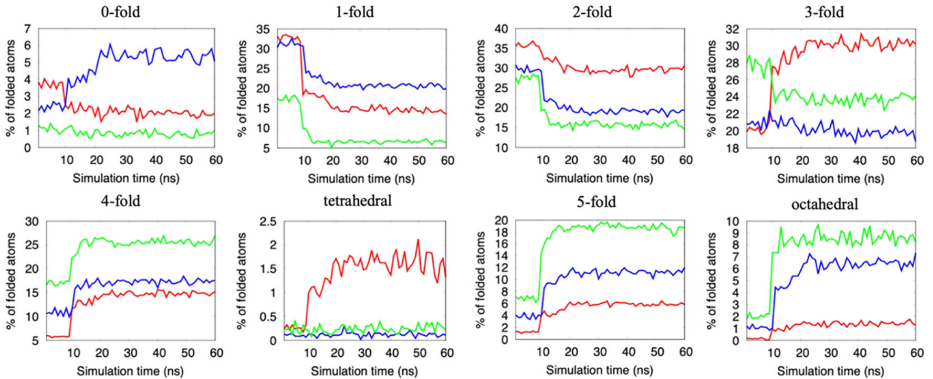


Figure 5.5: Percentage of folded atoms for each  $\text{Ge}_x\text{Se}_{1-x}$  system during the simulation time. The first 10 ns correspond to the melt, the jump corresponds to the quenching, and the last 50 ns correspond to the amorphous phase. In red, data for  $\text{Ge}_{0.4}\text{Se}_{0.6}$ ; in green, data for  $\text{Ge}_{0.5}\text{Se}_{0.5}$ ; and in blue, data for  $\text{Ge}_{0.6}\text{Se}_{0.4}$ .

Figure 5.5 shows the percentage of folds during the simulation time, where the first 10 ns are related to the melt phase and the last 50 ns to the solid amorphous phase, assuming as central atom both Ge and Se. The local order in the liquid phase is preferentially given by low-folded structures with a high percentage of 1- and 2-folds and by the lack of high-folded structures characteristic of the glassy networks. After cooling down, the amorphous phase shows an increase in high-folded structures from 3- to 6-folds, while the bond distribution percentage depends on stoichiometry. In particular,  $\text{Ge}_{0.4}\text{Se}_{0.6}$  has 2-, 3-, and

	$\text{Ge}_{0.4}\text{Se}_{0.6}$		$\text{Ge}_{0.5}\text{Se}_{0.5}$		$\text{Ge}_{0.6}\text{Se}_{0.4}$	
0-fold	$1.9 \pm 0.1$	0.2	$0.9 \pm 0.2$	0.3	$5.3 \pm 0.3$	2.1
		1.7		0.6		3.2
1-fold	$14.2 \pm 0.4$	2.9	$6.7 \pm 0.3$	3.2	$20.6 \pm 0.6$	16.9
		11.3		3.5		3.7
2-fold	$29.9 \pm 0.5$	7.5	$16.0 \pm 0.4$	7.6	$19.0 \pm 0.6$	12.6
		22.4		8.4		6.4
3-fold	$30.4 \pm 0.8$	11.3	$23.6 \pm 0.5$	11.1	$19.8 \pm 0.5$	11.8
		19.0		12.0		8.0
4-fold	$14.7 \pm 0.3$	10.7	$25.6 \pm 0.7$	12.4	$17.3 \pm 0.4$	9.2
		4.0		13.2		8.1
tetrahedral	$1.5 \pm 0.2$	0.1	$0.3 \pm 0.1$	0.2	$0.1 \pm 0.0$	0.1
		1.4		0.1		0.0
5-fold	$5.9 \pm 0.3$	5.8	$18.5 \pm 0.4$	9.7	$11.3 \pm 0.3$	5.1
		0.1		8.8		6.2
octahedral	$1.5 \pm 0.2$	1.5	$8.4 \pm 0.4$	5.5	$6.5 \pm 0.4$	2.2
		0.0		2.9		4.3

<sup>a</sup>On the central cell, the value considering both Ge and Se as central atoms, while we indicate the decomposition of the central Ge (Se) atom in the smaller cell at the top (bottom) right for each computed system.

Table 5.1: Percentage (%) of Folded Atoms for Each  $\text{Ge}_x\text{Se}_{1-x}$  Amorphous System Computed on the Last 10 ns of Simulations<sup>a</sup>

tetrahedral folds with a low amount of 5- and 6- folds with respect to the other two stoichiometries. On the contrary,  $\text{Ge}_{0.5}\text{Se}_{0.5}$  has the highest number of 4-, 5-, and 6- folded structures, while  $\text{Ge}_{0.6}\text{Se}_{0.4}$  is in between, as shown in Figure 5.5 and Table 1. These results clearly indicate that high Ge contents promote the formation of networks. Experimental results based on photoemission X-ray photoelectron spectroscopy (XPS) and ultraviolet photoelectron spectroscopy (UPS) on a-GeSe [54] suggest the presence of a chemically ordered structure and not a random bond structure. It has been shown that a thin film of a-GeSe deposited onto a cooled substrate has a 3:3-fold coordination (i.e., 3-fold Ge and 3-fold Se), but it relaxes onto a 4:2-fold coordination after thermal annealing (i.e., 4-fold Ge and 2-fold Se). Other studies have also suggested a possible 4:2 folding of a-GeSe, but a common consensus is lacking. O'Reilly et al.[55] stated that a- GeSe has a 3:3 coordinated structure, while Trodahl et al.[56] used far-infrared absorption to show that the 4:2-fold coordinated model is more appropriate for this system, although the 3:3-fold is also possible. Trodahl[44] also showed how heteropolar bonds are favored over homopolar bonds. We must highlight that these experimental studies do not have enough sensitivity to small density of defects because the signal is averaged over the whole material. Our findings for the a- $\text{Ge}_{0.5}\text{Se}_{0.5}$  indicate that the most probable folds at room temperature are the 3- and 4-folds for both Ge and Se species. To prove that the amorphous structure does not keep memory of the starting structure or of the melting-quenching preparation process, we performed a second cycle of heating at 1500 K for 10 ns and quenching to 300 K using as starting structure the last configuration reached from the amorphous phase (i.e., continuing the MD simulation). The same parameters described in the Methods section were used and the atoms folding were calculated on the new obtained amorphous system. The resulting folding values for the liquid have the same average values reported in Figure 5.5, with a high number of low-folded atoms. This demonstrates that the system has completely lost the memory of the initial amorphous structure.

In a similar way, after quenching, a- GeSe show the same folding distributions as those reported in Table 1. Subsequent cycles of heating and quenching produce new amorphous structures with very similar properties but with no memory of previous configurations. Apart from the specific differences due to stoichiometry, analysis of Figure 5.5 indicates two general features: (i) the atomic folding increases as the temperature is reduced and (ii) the process to form highly folded structures requires a reorganization time of the order of 10 ns. The latter time scale is unaffordable for standard first-principles simulations. Thus, fast ab initio quenching steps (ca. 10-20 ps) may freeze the system in liquid-like phase (i.e., low-folded distribution), not allowing the atoms to rearrange and fold in the structures typical of the amorphous solid. As a comparison, we report in the SI the results of an ab initio Car-Parrinello molecular dynamics simulation on  $\text{Ge}_{0.5}\text{Se}_{0.5}$  that clearly shows an overall low-folded atomic distribution of the sample, even at room temperature. We analyzed the chemical distribution of the folded structures, and we found that both Ge and Se may be at the center of the fold. However, while central Se atoms are connected only to peripheral Ge atoms, central Ge atoms are connected to both Se and Ge external atoms. This behavior is found for all three compositions, and in particular for  $\text{Ge}_{0.6}\text{Se}_{0.4}$ . In this case, the central Ge atoms preferentially connect to Se but always coordinate with at least one peripheral Ge per folded structure. For example, for the 4-fold case, Ge atoms mostly bind to 3 Se and 1 Ge, suggesting that Ge can form minority homopolar bonds, as previously shown by Liu et al.[57] The analysis of the bond angle distribution (BAD) can help to gain insight into the short-range order structures and, in particular, those for Ge-Se-Ge and Se-Ge-Se triads that are the most significant. As shown in Figure 5.6, the angle distributions are dependent on Ge concentration, but a general trend can be observed: the main peaks are located around  $90^\circ$ , with smaller contributions between  $130$  and  $170^\circ$ . Furthermore, on increasing the Se concentration, we detect an increase of spectral weight around  $109.5^\circ$  (Table 1), which is the typical fingerprint of tetrahedral structures, in agreement with a-GeSe<sub>2</sub> results.[24][27] On the contrary, on increasing the Ge content, the distribution is centered close to  $90^\circ$ , but the peak height diminishes and two additional peaks at  $75^\circ$  and at  $130^\circ$  appear. These findings suggest that increasing the Ge content increases the disorder of the system in chalcogenides. The decomposition of BAD for each folded kind indicates that the major contribution to both angles in  $\text{Ge}_{0.4}\text{Se}_{0.6}$  is associated with the 2- and 3-folds, while the contribution of tetrahedral and octahedral folds is negligible. In the case of  $\text{Ge}_{0.5}\text{Se}_{0.5}$ , the 3-, 4-, 5-, and octahedral folds contribute almost equally to the distribution with marked peaks close to  $90^\circ$ . In the case shown by Trodhal[56] for the 4:2-fold coordination of a-GeSe, the GeSe<sub>4</sub> tetrahedral folds have an average angle of  $90^\circ$ , in agreement with Figure 5.6.b.

### 5.3.3 Medium-Range Order

The medium-range order describing the connectivity of the network of  $\text{Ge}_x\text{Se}_{1-x}$  has been obtained by computing the ring size and their spatial distribution using the King’s algorithm,[38] as implemented in the R.I.N.G.S. code.[58] Topological

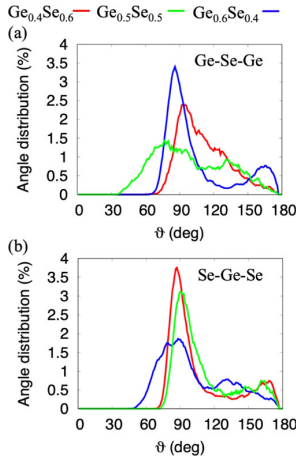


Figure 5.6: Bond angle distribution of Ge-Se-Ge (a) and Se-Ge-Se (b) in amorphous  $\text{Ge}_x\text{Se}_{1-x}$  systems at 300 K.

networks, such as amorphous systems, are represented in graph theory associating nodes for the atoms and links for the bonds. The possible formation of links between nodes is given by the analysis of the radial distribution function. A closed path connecting linked  $n$  nodes is called an  $n$ -membered ring. Previous

ring size	$\text{Ge}_{0.4}\text{Se}_{0.6}$	$\text{Ge}_{0.5}\text{Se}_{0.5}$	$\text{Ge}_{0.6}\text{Se}_{0.4}$
3	0	63	402
4	46	403	184
5	0	69	178
6	85	965	165
7	0	118	169
8	56	1144	188
9	0	169	228
10	61	888	293
11	0	56	316
12	87	313	351
13	0	0	375
14	68	22	40
total	403	4209	2889

Table 5.2: Ring Size Counts for  $\text{Ge}_x\text{Se}_{1-x}$  Systems

studies[59] on  $\text{GeSe}_2$  showed a correlation between band gap and the presence of medium-range order structures, such as four- and six-membered rings and Ge-Se-Ge angles. These findings suggest that there is a strong correlation between the ring network and their electrical properties, although a clear view is still missing due to the large number of variables involved. The ring statistics have been performed using the location of the first peaks of the radial distribution functions as input for the ring's code. For each composition, the locations are slightly different, and they implicitly take into account the different densities of the system. In this way, the results coming from the ring analysis are consistent and they do not depend on the chosen density.

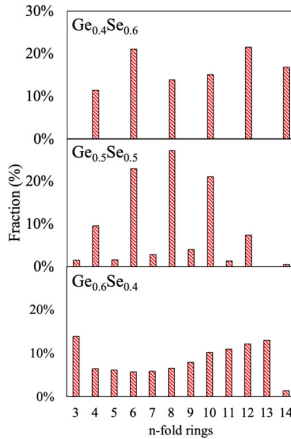


Figure 5.7: Ring size probability for  $\text{Ge}_x\text{Se}_{1-x}$  systems.

The results of ring analysis are summarized in Table 2: Systems with a high Ge content ( $\text{Ge}_{0.5}\text{Se}_{0.5}$  and  $\text{Ge}_{0.6}\text{Se}_{0.4}$ ) may form both homopolar Ge-Ge and heteropolar Ge-Se bonds<sup>61</sup> that arrange in both even-membered and odd-membered rings. In particular, for  $\text{Ge}_{0.5}\text{Se}_{0.5}$ , the majority of the rings are composed of 6, 8, and 10 elements (Figure 5.7), while the  $\text{Ge}_{0.6}\text{Se}_{0.4}$  system has a predominance of 3- and 10- to 13- membered rings. In the Se-rich  $\text{Ge}_{0.4}\text{Se}_{0.6}$  system, the lack of homopolar Ge-Ge and Se-Se bonds results in the formation of only even-membered rings (i.e., ABAB rings) with alternating sequences of Ge-Se atoms. The size of rings (i.e., number of nodes per ring) and their chemical character (i.e., homopolar or heteropolar links) are not sufficient to fully characterize the spatial distribution of rings across the sample and the possibility to have spatial networks of connected rings. In this regard, we introduce two indexes, namely,  $\text{Rc}(n)$  and  $\text{PN}(n)$ .<sup>[58]</sup>  $\text{Rc}(n)$  is the number of rings per cell, that is, the number of all different rings of size  $n$  that correspond at least once to the King's criterion,<sup>[38]</sup> divided by the number of nodes;  $\text{PN}(n)$  is the proportion of nodes, which is the number of nodes that share more than one ring of size  $n$ . The former accounts for the spatial extension of rings, while the latter accounts for the connectivity of rings with the same size. The  $\text{Rc}(n)$  values (Figure 5.8.a) for  $\text{Ge}_{0.4}\text{Se}_{0.6}$  are extremely low for each ring size, indicating a limited propensity of the system in forming rings and a low network connectivity (low medium-range order). The other two systems have higher  $\text{Rc}(n)$  values, which correspond to a high probability to form rings, whose size distribution is given in Table 2. In  $\text{Ge}_{0.5}\text{Se}_{0.5}$ , the high  $\text{Rc}(n)$ , along with the low  $\text{PN}(n)$  for  $n < 8$ , indicates the formation of connected networks made of rings with different sizes (i.e., 4-, 6-, and 8-membered rings). Notably, the  $\text{PN}(n)$  values reported in Figure 5.8.b are lower than the ones estimated for other amorphous systems such as  $\text{GeS}_2$ ,  $\text{SiO}_2$ ,<sup>[58]</sup>  $\text{TeO}_2$ ,<sup>[60]</sup> and  $\text{ZnCl}_2$ ,<sup>[61]</sup> indicating for these systems the formation of networks of interconnected rings with the same size

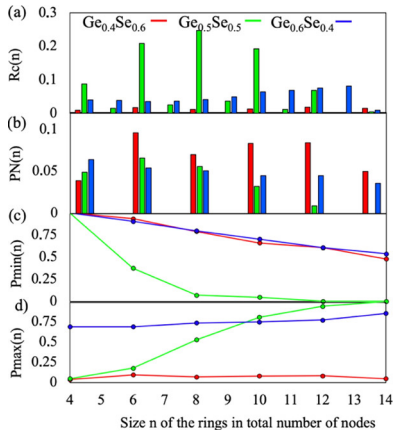


Figure 5.8: Connectivity profiles for the  $\text{Ge}_x\text{Se}_{1-x}$  system: (a)  $R_c(n)$ , (b)  $P_N(n)$ , (c)  $P_{\min}(n)$ , and (d)  $P_{\max}(n)$ .

( $n$ -membered). To have a deeper understanding of the network connectivity, we introduced other two parameters,  $P_{\min}(n)$  and  $P_{\max}(n)$ , that describe the proportion of nodes for which the rings of size  $n$  are the shortest and longest closed paths using these nodes to start the search, respectively. These parameters quantify the distribution of short-to-long connected rings. For homogeneous networks made only of  $n$ -membered rings,  $P_{\min}(n) = P_{\max}(n) = 1$ , while for networks that alternate short and long rings,  $P_{\min}(n)$  is higher for starting long-ring nodes, i.e., the opposite holds for  $P_{\max}(n)$ . In the case of  $\text{Ge}_{0.5}\text{Se}_{0.5}$ , the  $P_{\min}$  curve (Figure 5.8.c) decreases rapidly to 0 for  $n > 6$ , while  $P_{\max}$  increases to 1 for  $n = 12$  (Figure 5.8.d). This corresponds to the formation of connected networks by the alternation of rings of different sizes, ranging from  $n = 6$  to 12. For both  $\text{Ge}_{0.4}\text{Se}_{0.6}$  and  $\text{Ge}_{0.6}\text{Se}_{0.4}$ , a large  $P_{\min}$  value indicates the high probability of finding the shortest path for the node at the origin of the search, which corresponds to alternation of rings of all possible sizes. However, the different  $P_{\max}$  index indicates a different long-range distribution: low connectivity (low number of disconnected rings) for  $\text{Ge}_{0.4}\text{Se}_{0.6}$  and high connectivity for  $\text{Ge}_{0.6}\text{Se}_{0.4}$ , in agreement with the corresponding large number of shared nodes (connected rings) expressed by  $R_c(n)$  and  $P_N(n)$ , respectively. The large ring network variability is expected to impart a different electrical behavior to  $\text{Ge}_x\text{Se}_{1-x}$  systems, as a function of the stoichiometry, as detected in experimental measurements. [10][16][17]

## 5.4 Conclusion

In summary, we have performed classical molecular dynamics (MD) simulations of large-scale  $\text{Ge}_x\text{Se}_{1-x}$  systems in the  $0.4 < x < 0.6$  range to study the structure of their liquid and amorphous phases over nanosecond-long time scales.

MD simulations well reproduce all of the main short-range features previously observed by ab initio molecular dynamics and by neutron diffraction studies for similar systems, such as GeSe<sub>2</sub> and liquid Ge<sub>0.5</sub>Se<sub>0.5</sub>, and provide a reliable model for the amorphous phase at room temperature. Amorphous phases are characterized by different levels of ordering depending on the relative Ge content. In the short range, all systems present a predominant amount of highly folded structures, whose chemical composition differs in the formation of homopolar Ge-Ge bonds, for Ge-rich samples. In the medium range, systems with Ge from 50 to 60% show the formation of a dense and interconnected network with a high percentage of rings, while networks of systems containing a lower Ge content are characterized by a reduced number of disconnected rings. In analogy with other chalcogenide systems, these structural differences are expected to affect the gap properties of Ge<sub>x</sub>Se<sub>1-x</sub> compounds. However, while a different hierarchical short- and long-range order is clearly seen in three examined stoichiometries, its direct effect of the electronic and electrical properties (e.g., ovonic switching) has to be confirmed by specific quantum-mechanical investigations. The success of classical MD simulations in the description of amorphous Ge<sub>x</sub>Se<sub>1-x</sub> structures paves the way to the study of other chalcogenide glasses, including dopants, for applications as OTS chalcogenides materials.

## 5.5 Associated content

The Supporting Information is available free of charge at:

<https://pubs.acs.org/doi/10.1021/acsaelm.0c00581>.

Numerical details and tests on the generated FF (Section S1); further analysis of Ge<sub>x</sub>Se<sub>1-x</sub> melt and amorphous phase, including g(r) for the liquid phase, coordination number atom statistics of the folds, decomposition of angle distribution, and sample of ring structures (Section S2); and comparison with an ab initio molecular dynamics simulation (Section S3) (PDF)

## References

- [1] Indiveri, G. and Liu, S. -. “Memory and Information Processing in Neuromorphic Systems”. English. In: *Proceedings of the IEEE* vol. 103, no. 8 (2015). Cited By :279, pp. 1379–1397.
- [2] Waser, R. and Aono, M. “Nanoionics-based resistive switching memories”. English. In: *Nanoscience and Technology: A Collection of Reviews from Nature Journals*. Cited By :27. 2009, pp. 158–165.
- [3] Raoux, S. et al. “Phase change materials and phase change memory”. English. In: *MRS Bulletin* vol. 39, no. 8 (2014). Cited By :238, pp. 703–710.

- [4] Chappert, C., Fert, A., and Van Dau, F. N. “The emergence of spin electronics in data storage”. English. In: *Nanoscience and Technology: A Collection of Reviews from Nature Journals*. Cited By :17. 2009, pp. 147–157.
- [5] Strukov, D. B. et al. “The missing memristor found”. English. In: *Nature* vol. 453, no. 7191 (2008). Cited By :6410, pp. 80–83.
- [6] Zhang, L. In: *Study of the Selector Element for Resistive Memory* (2015). Cited By :7.
- [7] Chai, Z. et al. “GeSe-Based Ovonic Threshold Switching Volatile True Random Number Generator”. English. In: *IEEE Electron Device Letters* vol. 41, no. 2 (2020). Cited By :4, pp. 228–231.
- [8] Chen, A. In: *Emerging Memory Selector Devices* (2013). Cited By :1.
- [9] Lee, M. -. et al. “A plasma-treated chalcogenide switch device for stackable scalable 3d nanoscale memory”. English. In: *Nature Communications* vol. 4 (2013). Cited By :78.
- [10] Chai, Z. et al. “Dependence of Switching Probability on Operation Conditions in GexSe1-x Ovonic Threshold Switching Selectors”. English. In: *IEEE Electron Device Letters* vol. 40, no. 8 (2019). Cited By :6, pp. 1269–1272.
- [11] Ovshinsky, S. R. “Reversible electrical switching phenomena in disordered structures”. English. In: *Physical Review Letters* vol. 21, no. 20 (1968). Cited By :2562, pp. 1450–1453.
- [12] Liu, G. et al. “Increasing Trapped Carrier Density in Nanoscale GeSeAs Films by As Ion Implantation for Selector Devices in 3D-Stacking Memory”. English. In: *ACS Applied Nano Materials* vol. 2, no. 9 (2019). Cited By :3, pp. 5373–5380.
- [13] Sun, Y. et al. “Short-Term and Long-Term Plasticity Mimicked in Low-Voltage Ag/GeSe/TiN Electronic Synapse”. English. In: *IEEE Electron Device Letters* vol. 39, no. 4 (2018). Cited By :30, pp. 492–495.
- [14] Yoo, S. et al. “Chemical interactions in the atomic layer deposition of Ge-Sb-Se-Te films and their ovonic threshold switching behavior”. English. In: *Journal of Materials Chemistry C* vol. 6, no. 18 (2018). Cited By :15, pp. 5025–5032.
- [15] Song, B. et al. “An ovonic threshold switching selector based on Se-rich GeSe chalcogenide”. English. In: *Applied Physics A: Materials Science and Processing* vol. 125, no. 11 (2019). Cited By :7.
- [16] Kim, S. -. et al. “Effect of Ge concentration in GeXse1-x chalcogenide glass on the electronic structures and the characteristics of ovonic threshold switching (OTS) devices”. English. In: *ECS Solid State Letters* vol. 2, no. 10 (2013). Cited By :23, Q75–Q77.



- [17] Shin, S. -. et al. “The effect of doping Sb on the electronic structure and the device characteristics of Ovonic Threshold Switches based on Ge-Se”. English. In: *Scientific Reports* vol. 4 (2014). Cited By :32.
- [18] Micoulaut, M. and Massobrio, C. “Improving the structural description of high-temperature liquid GeSe<sub>2</sub> from ab initio molecular dynamics simulations”. English. In: *Journal of Optoelectronics and Advanced Materials* vol. 11, no. 12 (2009). Cited By :16, pp. 1907–1914.
- [19] Petri, I., Salmon, P. S., and Fischer, H. E. “Structure of the liquid semiconductor GeSe”. English. In: *Journal of Physics Condensed Matter* vol. 11, no. 37 (1999). Cited By :28, pp. 7051–7060.
- [20] Giacomazzi, L., Massobrio, C., and Pasquarello, A. “First-principles investigation of the structural and vibrational properties of vitreous Ge Se<sub>2</sub>”. English. In: *Physical Review B - Condensed Matter and Materials Physics* vol. 75, no. 17 (2007). Cited By :40.
- [21] Le Roux, S. et al. “The structure of liquid GeSe revisited: A first principles molecular dynamics study”. English. In: *Journal of Chemical Physics* vol. 138, no. 17 (2013). Cited By :20.
- [22] Van Roon, F. H. M. et al. “Structure of liquid GeSe: A first principle study”. English. In: *Journal of Chemical Physics* vol. 113, no. 13 (2000). Cited By :26, pp. 5425–5431.
- [23] Murgatroyd, P. A. E. et al. “GeSe: Optical Spectroscopy and Theoretical Study of a van der Waals Solar Absorber”. In: *Chem.Mater.* vol. 32 (2020). Cited By :5, pp. 3245–3253.
- [24] Vashishta, P., Kalia, R. K., and Ebbsjö, I. “Structural correlations and vibrational spectra of molten and glassy GeSe<sub>2</sub>”. English. In: *Solid State Ionics* vol. 32-33, no. PART 2 (1989). Cited By :3, pp. 872–881.
- [25] Yang, G. et al. “Physical properties of the Ge<sub>x</sub>Se<sub>1-x</sub> glasses in the 0<x<0.42 range in correlation with their structure”. English. In: *Journal of Non-Crystalline Solids* vol. 377 (2013). Cited By :44, pp. 54–59.
- [26] Plimpton, S. “Fast parallel algorithms for short-range molecular dynamics”. English. In: *Journal of Computational Physics* vol. 117, no. 1 (1995). Cited By :22968, pp. 1–19.
- [27] Vashishta, P. et al. “Atomic correlations and intermediate-range order in molten and amorphous GeSe<sub>2</sub>”. English. In: *Physical Review Letters* vol. 62, no. 14 (1989). Cited By :119, pp. 1651–1654.
- [28] Vashishta, P., Kalia, R. K., and Ebbsjö, I. “Structural correlations and phonon density of states in GeSe<sub>2</sub>: A molecular-dynamics study of molten and amorphous states”. English. In: *Physical Review B* vol. 39, no. 9 (1989). Cited By :96, pp. 6034–6047.
- [29] Rino, J. P. et al. “A molecular dynamics study of superionic Ag<sub>2</sub>Se”. English. In: *Solid State Ionics* vol. 32-33, no. PART 2 (1989). Cited By :4, pp. 968–973.

- [30] Iyetomi, H., Vashishta, P., and Kalia, R. K. “Incipient phase separation in Ag/Ge/Se glasses: Clustering of Ag atoms”. English. In: *Journal of Non-Crystalline Solids* vol. 262, no. 1 (2000). Cited By :24, pp. 135–142.
- [31] Vashishta, P. et al. “Interaction potential for aluminum nitride: A molecular dynamics study of mechanical and thermal properties of crystalline and amorphous aluminum nitride”. English. In: *Journal of Applied Physics* vol. 109, no. 3 (2011). Cited By :46.
- [32] Vashishta, P. et al. “Interaction potential for SiO<sub>2</sub>: A molecular-dynamics study of structural correlations”. English. In: *Physical Review B* vol. 41, no. 17 (1990). Cited By :453, pp. 12197–12209.
- [33] Campbell, T. et al. “Structural correlations and mechanical behavior in nanophase silica glasses”. English. In: *Physical Review Letters* vol. 82, no. 20 (1999). Cited By :52, pp. 4018–4021.
- [34] Kodiyalam, S. et al. “Grain boundaries in gallium arsenide nanocrystals under pressure: a parallel molecular-dynamics study”. English. In: *Physical Review Letters* vol. 86, no. 1 (2001). Cited By :53, pp. 55–58.
- [35] Kodiyalam, S. et al. “Multiple grains in nanocrystals: Effect of initial shape and size on transformed structures under pressure”. English. In: *Physical Review Letters* vol. 93, no. 20 (2004). Cited By :25, pp. 203401-1-203401-4.
- [36] Errington, J. R. and Debenedetti, P. G. “Relationship between structural order and the anomalies of liquid water”. English. In: *Nature* vol. 409, no. 6818 (2001). Cited By :999, pp. 318–321.
- [37] Chau, P. and Hardwick, A. J. “A new order parameter for tetrahedral configurations”. English. In: *Molecular Physics* vol. 93, no. 3 (1998). Cited By :349, pp. 511–518.
- [38] King, S. V. “Ring configurations in a random network model of vitreous silica [8]”. English. In: *Nature* vol. 213, no. 5081 (1967). Cited By :131, pp. 1112–1113.
- [39] Cobb, M. and Drabold, D. “Ab initio molecular-dynamics study of liquid”. English. In: *Physical Review B - Condensed Matter and Materials Physics* vol. 56, no. 6 (1997). Cited By :67, pp. 3054–3065.
- [40] Penfold, I. T. and Salmon, P. S. “Structure of covalently bonded glass-forming melts: A full partial-structure-factor analysis of liquid GeSe<sub>2</sub>”. English. In: *Physical Review Letters* vol. 67, no. 1 (1991). Cited By :132, pp. 97–100.
- [41] Petri, I., Salmon, P. S., and Fischer, H. E. “Defects in a disordered world: The structure of glassy GeSe<sub>2</sub>”. English. In: *Physical Review Letters* vol. 84, no. 11 (2000). Cited By :227, pp. 2413–2416.
- [42] Massobrio, C., Pasquarello, A., and Car, R. “Short- and intermediate-range structure of liquid GeSe<sub>2</sub>”. English. In: *Physical Review B - Condensed Matter and Materials Physics* vol. 64, no. 14 (2001). Cited By :78, pp. 1442051–14420512.

- [43] Raty, J. Y. et al. “Distance correlations and dynamics of liquid GeSe: An ab initio molecular dynamics study”. English. In: *Physical Review B - Condensed Matter and Materials Physics* vol. 64, no. 23 (2001). Cited By :22, pp. 2352091–2352097.
- [44] Trodahl, H. J. “Vibrational studies of the short range order in a-GeSe 1-x films”. English. In: *Journal of Physics C: Solid State Physics* vol. 17, no. 33 (1984). Cited By :7, pp. 6027–6033.
- [45] Lai, M., Zhang, X., and Fang, F. “Crystal Orientation Effect on the Subsurface Deformation of Monocrystalline Germanium in Nanometric Cutting”. English. In: *Nanoscale Research Letters* vol. 12 (2017). Cited By :13.
- [46] Tanaka, K. “Structural phase transitions in chalcogenide glasses”. English. In: *Physical Review B* vol. 39, no. 2 (1989). Cited By :571, pp. 1270–1279.
- [47] Iyetomi, H., Vashishta, P., and Kalia, R. K. “The intermediate-range order in molten and glassy GeSe<sub>2</sub>”. English. In: *Solid State Ionics* vol. 32-33, no. PART 2 (1989). Cited By :5, pp. 954–958.
- [48] Koura, A. and Shimojo, F. “Static Structure of Liquid GeSe Under Pressure: Ab Initio Molecular Dynamics Simulations”. English. In: *Physica Status Solidi (B) Basic Research* vol. 255, no. 11 (2018). Cited By :1.
- [49] Wełnic, W. et al. “Origin of the optical contrast in phase-change materials”. English. In: *Physical Review Letters* vol. 98, no. 23 (2007). Cited By :128.
- [50] Wełnic, W. et al. “Unravelling the interplay of local structure and physical properties in phase-change materials”. English. In: *Nature Materials* vol. 5, no. 1 (2006). Cited By :275, pp. 56–62.
- [51] Zipoli, F., Krebs, D., and Curioni, A. “Structural origin of resistance drift in amorphous GeTe”. English. In: *Physical Review B* vol. 93, no. 11 (2016). Cited By :35.
- [52] Li, H. and Robertson, J. “A unified mid-gap defect model for amorphous GeTe phase change material”. English. In: *Applied Physics Letters* vol. 116, no. 5 (2020). Cited By :3.
- [53] Konstantinou, K. et al. “Revealing the intrinsic nature of the mid-gap defects in amorphous Ge<sub>2</sub>Sb<sub>2</sub>Te<sub>5</sub>”. English. In: *Nature Communications* vol. 10, no. 1 (2019). Cited By :19.
- [54] Takahashi, T., Sakurai, H., and Sagawa, T. “Photoemission (UPS and XPS) study of crystallization of amorphous GeTe film”. English. In: *Solid State Communications* vol. 44, no. 5 (1982). Cited By :13, pp. 723–726.
- [55] O’Reilly, E. P., Robertson, J., and Kelly, M. J. “The structure of amorphous GeSe and GeTe”. English. In: *Solid State Communications* vol. 38, no. 7 (1981). Cited By :36, pp. 565–568.
- [56] Trodahl, H. J. “Far infrared absorption of a-GeSe”. English. In: *Solid State Communications* vol. 44, no. 3 (1982). Cited By :8, pp. 319–321.

- [57] Liu, G. et al. “The investigations of characteristics of GeSe thin films and selector devices for phase change memory”. English. In: *Journal of Alloys and Compounds* vol. 792 (2019). Cited By :4, pp. 510–518.
- [58] Le Roux, S. and Jund, P. “Ring statistics analysis of topological networks: New approach and application to amorphous GeS<sub>2</sub> and SiO<sub>2</sub> systems”. English. In: *Computational Materials Science* vol. 49, no. 1 (2010). Cited By :192, pp. 70–83.
- [59] Holomb, R. et al. “New ring-like models and ab initio DFT study of the medium-range structures, energy and electronic properties of GeSe<sub>2</sub> glass”. English. In: *Philosophical Magazine* vol. 93, no. 19 (2013). Cited By :10, pp. 2549–2562.
- [60] Gulenko, A. et al. “Atomistic simulations of TeO<sub>2</sub>-based glasses: Interatomic potentials and molecular dynamics”. English. In: *Physical Chemistry Chemical Physics* vol. 16, no. 27 (2014). Cited By :43, pp. 14150–14160.
- [61] Zeidler, A. et al. “Structure of liquid and glassy ZnCl<sub>2</sub>”. English. In: *Physical Review B - Condensed Matter and Materials Physics* vol. 82, no. 10 (2010). Cited By :51.

## Chapter 6

# A first principle study of the switching mechanism of $\text{Ge}_{54}\text{Te}_{216}\text{As}_{20}\text{Se}_{30}$ for selectors applications

### Abstract

We present a first principle study of the switching mechanism of  $\text{Ge}_{54}\text{Te}_{216}\text{As}_{20}\text{Se}_{30}$  (ASGT) for Memory applications, The electrical and structural properties of  $\text{Ge}_3\text{Te}_4$  and the effects of  $\text{As}_2\text{Se}_3$  are studied in the framework of ab initio simulations coupled within the Carr-Parrinello approach and density functional theory. The approach is computationally expensive and took almost 2 years. The structural analysis are carried out via utilizing the BELLO code for structural trajectories. In order to simulated the electrical switching behavior of chalcogenide glasses in selectors, the systems are melted up to their melting temperature then quenched back down to 300K. The correlation between the amorphous and crystalline phases are thoroughly studied via our statistical approaches coupled with density functional calculations. Our findings paved new routes towards thermal approaches in chalcogenide glasses studies for switching materials.

### Contents

6.1	Introduction . . . . .	83
6.2	Methodology . . . . .	84
6.3	Results and Discussion . . . . .	85
6.4	Conclusion . . . . .	91
	References . . . . .	91

### 6.1 Introduction

Recent advancements in technology has increased the need for power efficient memories with more capacity. As the 3D stacking architecture for memories evolve, demand for better selectors in 3D joints also increase which can be tailored

to the specific electrical needs. Chalcogenide glasses, as the best candidate for these types of materials, display electrical switching under high electric fields [1, 2] which is desirable for selector applications. In these materials, like most of the materials, while the applied electric field is low, voltage and current follow a linear relationship, However, as the electrical field increases, its behavior becomes non-linear and at a critical point the electrical resistivity undergoes an abrupt change resulting in switching from a low-conducting state (OFF)(amorphous) to a high-conducting (ON)(crystalline) state. The ON state switching can be divided into two types (1) threshold switching and (2) memory switching [3, 4, 5, 6, 7, 8, 9, 10]. The threshold switching (TS) device tends to conserve the high conducting (ON) state provided that a minimum amount of holding current is maintained. Moreover, if the current is lowered below the holding current ( $I_h$ ), the material will quickly switches back to its high resistivity (amorphous) OFF state. Additionally, While in a memory switching (MS) device, the ON state will be maintained even after the current is reduced to zero. The OFF state can be achieved by applying a suitable current pulse. These types of materials can be used in solid-state devices, wireless antennas, automotive industries and storage class memories [11, 12, 13, 14, 15]. Threshold switching is defined by electronic models, moreover, memory switching can be understood by thermal models [2, 16, 17]. Generally, the current-voltage curves of these materials have similar shapes showing negative differential resistance (NDR) before switching to the high conducting state. The difference is when the TS material reverts back to its OFF state while the MS one maintains the ON state. When all the trap states [16] in the band gap are filled by the field-induced charge carriers the threshold switching will occur, which results in a snap back in voltage leading to the switching from OFF to ON state. As In memory glasses, due to the Joule heating, a filament is created in between the electrodes with a temperature exceeding it's surrounding region. Therefore the current density passing in the filament is higher which leads to an even further temperature increase. Hence, a high conducting crystalline filament forms in between the electrodes [4, 5, 6, 7, 8, 9, 10, 18, 19, 20]. In this work, we have investigated the effects As<sub>2</sub>Se<sub>3</sub> on GeTe<sub>4</sub> chalcogenide glasses for selector applications. The investigation has been carried out in the framework of Density functional theory, the memory switching  $Ge_{54}Te_{216}$  (GeTe<sub>4</sub>) glass has been doped with  $As_{20}Se_{30}$  (As<sub>2</sub>Se<sub>3</sub>). Since the glass forming ability and the electrical resistivity of As<sub>2</sub>Se<sub>3</sub> are very high, it is expected that with the inclusion of As<sub>2</sub>Se<sub>3</sub>, there should be a conversion from memory to threshold switching. Using the statistical analysis of the density functional theory simulations we explored the switching mechanism of  $Ge_{54}Te_{216}As_{20}Se_{30}$  (ASGT) on an atomic level.

## 6.2 Methodology

**Computational Details:** Atomic structure of  $Ge_{54}Te_{216}$  was obtained by replicating the crystalline GeTe<sub>4</sub> unit cell in X, Y and Z directions. the initial structure was melted by increasing the temperature up to 1200K via ab initio

simulations coupled within the Carr-Parrinello approach with the Nose-Hoover thermostat switched on. after that, for obtaining a realistic amorphous phase, the system was quenched back down to 300K. The same process was then repeated for the  $\text{Ge}_{54}\text{Te}_{216}\text{As}_{20}\text{Se}_{30}$  alloy with the variable cell quenching down for 47.6 ps and staying at 300k for 9 ps with fixed cell dimensions. The systems were studied by means of electronic structure calculations based on density functional theory and a plane wave expansion of Kohn–Sham (KS) orbitals as implemented in the Quantum-Espresso suite of programs.[21] The Perdew–Burke–Ernzerhof (PBE) approximation<sup>33</sup> to the exchange and correlation functional and norm conserving pseudopotentials. A kinetic energy cutoff of 30 and 300 Ry were chosen for wavefunctions and charge density/potential respectively.

**Structure Analysis:** The radial distribution function  $g(r)$  has been computed in the last 5 ns of the simulation at 1200 K for the melt and in the last 15 ns at 300K for the crystalline/amorphous phases. The melting temperature for bulk  $\text{GeTe}_4$  is 720 C and  $\text{As}_2\text{Se}_3$  is around 350 c, while the glass-transition temperature for  $\text{GeTe}_4$  is at 190 C, thus, the high and low temperatures considered in the analysis are well representative of the melt and glassy states. The number of atoms bound to a central atom (i.e., the fold) has been computed with a cutoff distance of 2.8 Å and a tolerance of 0.2 Å using an in-house code called BELLO. The code primarily extracts geometrical structures varying from tetrahedral with 4 ligands (folds) to octahedral with 6 ligands, Special cases are the 0-fold, which means that an atom is not bound to any other atom, and the 1-fold, where the atom is connected only to another atom. The difference between tetrahedral and 4-fold atoms is given by the local-order parameter,  $q$  [22]

$$q = 1 - \frac{3}{8} \sum_{k>i} \left( \frac{1}{3} - \cos \theta_{ijk} \right)^2 \quad (6.1)$$

Where  $\theta_{ijk}$  is the angle formed between a central atom  $j$  and its neighboring atoms  $i$  and  $k$ . The  $q$  order parameter can discriminate between different geometries being equal to one for the perfect tetrahedral environment and to 0 for the ideal 6-Folded octahedral structure. In the case of a defective octahedral geometry,  $q = 5/8$  for 4-Fold coordinated atoms and  $q = 7/8$  for 3-Fold coordinated atoms in the pyramidal geometry.

## 6.3 Results and Discussion

**Short Range Order:** Radial distribution function of  $\text{GeTe}_4$  and  $\text{Ge}_{54}\text{Te}_{216}\text{As}_{20}\text{Se}_{30}$  are calculated for the results obtained from MD simulations. They are used for the analysis of two-body structural correlations. Figure 6.1 compares the radial distribution function  $g(r)$  of  $\text{GeTe}_4$  and  $\text{Ge}_{54}\text{Te}_{216}\text{As}_{20}\text{Se}_{30}$  at 300K for Ge and Te. The resulting Ge-Te and Te-Te  $g(r)$ 's of the amorphous phase show behavior similar to the previously published results [23]. As can be seen from Figure 6.1, a significant amount of Ge atoms tend to bond with Te atoms at 3 Å whereas the rest of the Te atoms are bonded to each other. This is while the Ge-Ge bonds are observed at a higher distance (second neighbour).

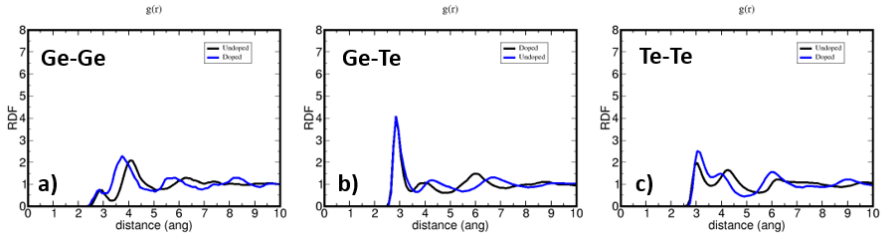


Figure 6.1: Radial distribution functions for  $\text{GeTe}_4$  (undoped) and  $\text{As}_2\text{Se}_3$  (doped) for different element correlations a) Ge-Ge b) Ge-Te c) Te-Te, 10 Å is chosen as the maximum distance for RDF as the first neighbour is in the vicinity of 3 Å.

The comparison reveals that  $\text{As}_2\text{Se}_3$  doping did not have a significant effect on the Ge-Te bonding while a small increase is observable in Te-Te. Ge-Ge atoms on the other hand. Figure 6.2 illustrates the radial distribution function for the

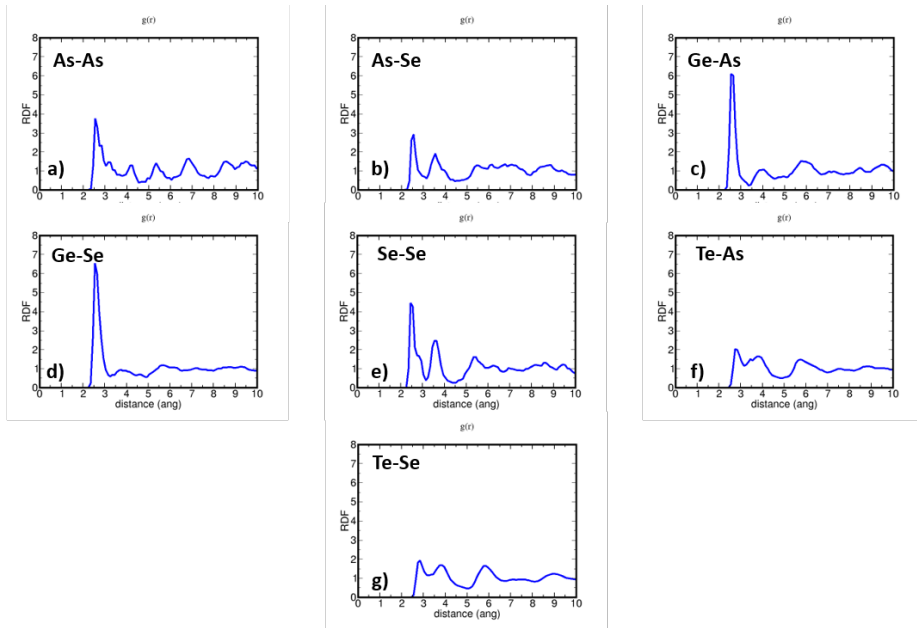


Figure 6.2: Radial distribution functions for ASGT illustrating the correlation between different elements present in the system a) As-As b) As-Se c) Ge-As d) Ge-Se e) Se-Se f) Te-As g) Te-Se.

case of  $\text{Ge}_{54}\text{Te}_{216}\text{As}_{20}\text{Se}_{30}$ , As present the majority of the bonds in the system belong to Ge-Se and Ge-As as well as Se-Se implying a more organized atomic structure to that of the undoped system.



**Electronic Structure:** Figure 6.3 shows a comparison between the calculated density of states of two systems. Fermi level is drawn by dashed lines at 5.7 eV and 8.2 eV for  $\text{GeTe}_4$  and ASGT respectively. The electronic state of  $\text{GeTe}_4$  during quenching can be seen in Figure 6.3.a, The curves indicate that while quenching down to room temperature the atomic structure has formed into a glassy amorphous phase but retaining some of its original crystalline structures contributing to the Fermi level states. However, in Figure 3-b with the Fermi level filled with electronic states a metal-like system is observed, Moreover, the IPR shows no localized trap states in the material. This is an indication that a significant amount of crystalline atomic structures should be present in the system.

**Local Order Statistics:** The correlation between the electronic state and the atomic local orders present in the system is further investigated by the local-order statistics obtained from BELLO with bonding cutoff distance of 2.8 Å for a fixed cell structure. Figure 6.4 presents the statistics throughout the simulation at 300K. Presence of high-folded local orders in the systems is a characteristic of crystalline structures while the amorphous materials form low-folded (0-fold, 1-fold, 2-fold) local orders. For the case of  $\text{GeTe}_4$  a considerable amount of

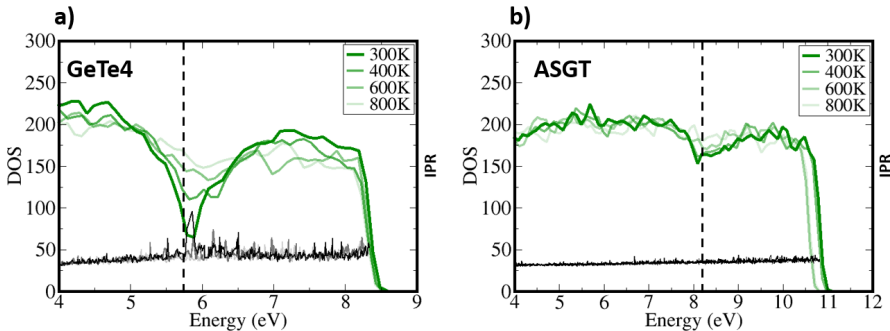


Figure 6.3: Density of state for a)  $\text{GeTe}_4$  and b) ASGT ( $\text{As}_2\text{Se}_3$ ) from liquid to solid phases, higher temperatures are illustrated by faded colors, Fermi levels are at 5.7 eV and 8.2 eV for  $\text{GeTe}_4$  and ASGT respectively.

local orders consist of 2-Folded with 3-Folds and 1-Folds being the second most popular geometry in the system, meaning the material is in a disordered state with 3-Folds causing the trap states in the mobility gap. On the contrary, for the crystalline  $\text{Ge}_{54}\text{Te}_{216}\text{As}_{20}\text{Se}_{30}$  (ASGT), 3-Folded structures dominate the system along side the 2-Fold and 4-Fold local orders, abundance of such geometries imply that the addition of As and Se promote the formation of networks. The percentage of tetrahedrals in the models of were quantified by computing the q order parameter introduced in [24] as a measure of the tetrahedrality of the atomic environments and defined by equation 1, Figure 6.5 reports the local order geometries with their corresponding q values. Figure 6.6 illustrates this

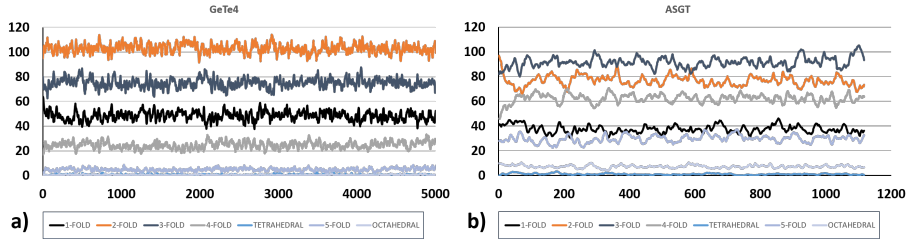


Figure 6.4: Statistical representation of local order population variations throughout the atomic structure trajectories for a)  $\text{GeTe}_4$  b)  $\text{As}_2\text{Se}_3$ . the noise in (a) is due to the high number of frames.

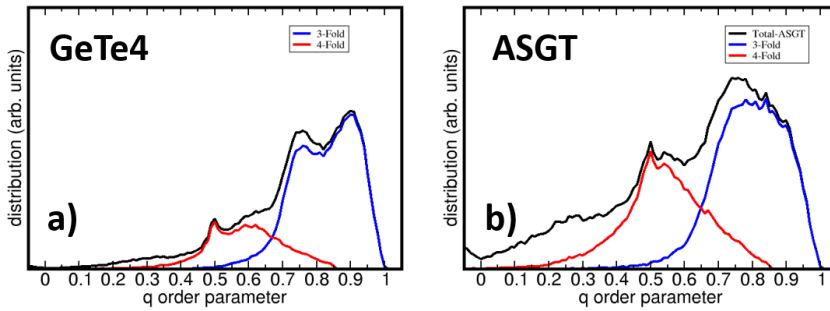


Figure 6.5: Order parameter  $q$  values shown for a)  $\text{GeTe}_4$  b)  $\text{As}_2\text{Se}_3$ . arbitrary values are normalized to unit cell density as well as trajectory size. overall increase of the  $q$  parameter indicates a more organized atomic structure.

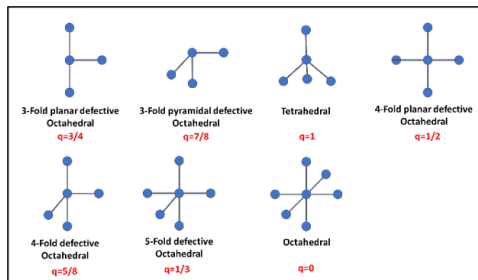


Figure 6.6: Present geometrical shapes and their corresponding  $q$  value.

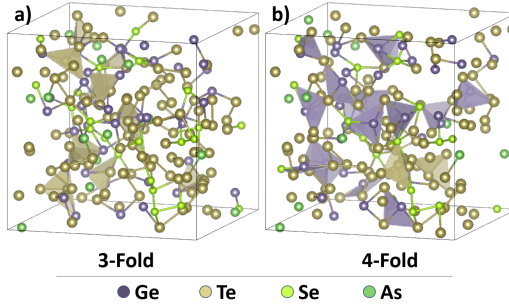


Figure 6.7: Snapshot of the last frame of ASGT structure with only a) 3-Fold b) 4-Fold geometries present.

parameter for GeTe<sub>4</sub> and ASGT, majority of the geometries are located in the 3-Fold and 4-Fold regions with 3-Fold-planar ( $q=0.75$ ) and 3-Fold-octahedral ( $q=0.87$ ) occupying the maximums in GeTe<sub>4</sub> while in ASGT, with the addition of As and Se and their bonding with Ge atoms an increase in the whole  $q$  parameter is observable. Furthermore, formation of more 3-Folds as suggested by the

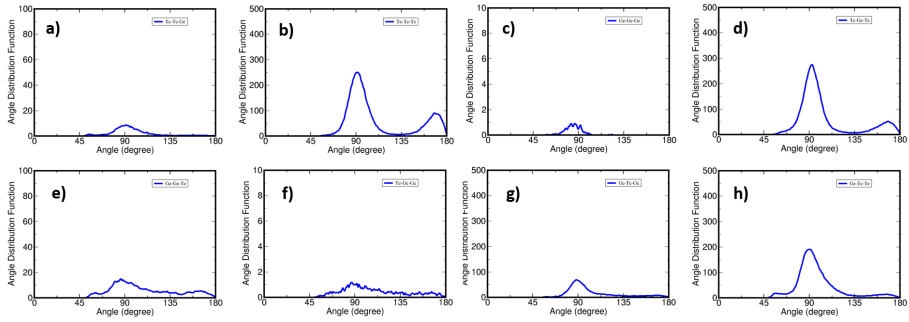


Figure 6.8: Bond angle distribution function for GeTe<sub>4</sub> for a) Te-Te-Ge b) Te-Te-Te c) Ge-Ge-Ge d) Te-Ge-Te e) Ge-Ge-Te f) Te-Ge-Ge g) Ge-Te-Ge h) Ge-Te-Te, axis scale values are changed accordingly.

local statistics and 4-Fold-planar geometries are present. Figure 6.7 depicts the extracted 3-Fold and 4-Fold polyhedral geometries, while most of the Ge atoms are shared between them, the 3-Fold structures are more densely packed. Atomic structure organization of the material can be further studied by means of Bond Angle Distribution Function which reports the frequency of angles occurring between bonds (between every two element which bonded to a central atom). Figure 6.8 reports the most frequent bond angle distribution function for GeTe<sub>4</sub>, the data is normalized on the unit cell density and averaged over trajectory frames. it is observable that the angles between Te-Te-Te, Te-Ge-Te

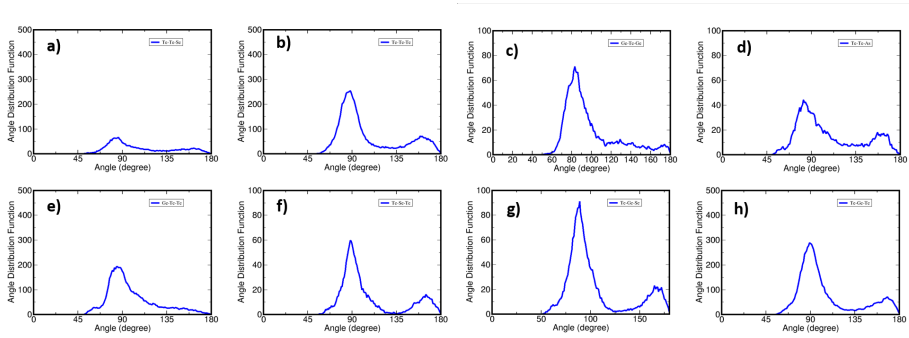


Figure 6.9: Bond angle distribution function for ASGT for angles of a) Te-Te-Se b) Te-Te-Te c) Ge-Te-Ge d) Te-Te-As e) Ge-Te-Te f) Te-Se-Te g) Te-Ge-Se h) Te-Ge-Te. a more pronounced distribution of angles at 90 and 180 degree is observable in comparison with the undoped structure.

and Ge-Te-Te bonds contribute the most to local orders respectively whereas the rest of the bonds are negligible. Moreover, concentration of bond angles in the vicinity of 90 and 180 degrees imply the existence of defective octahedral-like geometries in the system which are consistent with the reported results in the literature [25]. Additionally, Figure 6.9 depicts the bond angle distribution function for ASGT. As can be seen, a more organized structure is present here with more frequency on 90 and 180 degrees indicative of planar geometries. Present Te-Te and Te-Ge bonds are the remnants from undoped  $\text{GeTe}_4$  while the formation of Te-Ge-Se with 90/180 angles imply selenium's contribution to planar geometries. The remaining Te atoms are participating in Te-Se-Te bonds which indicates a planar structure with Se as the central atom. As on the other hand, mostly bonds as a solo ligand to Te-Te geometries (figure 8 d), This process transforms the previously 2-Folded Te-Te structures to 3-Folded ones as suggested by Figure 2. Ge atoms seem to be mostly surrounded with Te atoms while Te atoms act as both central atoms to Te-only geometries and ligands to Se atoms.

Overall, addition of  $\text{As}_2\text{Se}_3$  to  $\text{GeTe}_4$  not only conserves the already present local orders in the material but also forms new types of locally ordered structures which switch the material from its previously amorphous state to a metallic crystalline state, these states are caused by the 3-Fold and 4-Folded geometries in defective-octahedral and planar shapes formed by Se and Te atoms as central atom and ligand respectively, and As atoms acting as extra ligand to 2-folded Te atoms. Based on the predictions from experimental investigations reported by other groups [26] ASGT is presenting characteristics of a memory switching material.

## 6.4 Conclusion

In this work we have investigated the effects of  $\text{As}_2\text{Se}_3$  additive on  $\text{GeTe}_4$  for Memory switching application. As suggested by the experimental reports in [26], addition of  $\text{As}_2\text{Se}_3$  to  $\text{GeTe}_4$  controls the margin between threshold and memory switching via atomic structure configuration. We confirm that by simulating the melt-quench process in the framework of ab initio calculations coupled within the Carr-Parrinello approach. After the quenching, an amorphous state with remnants of its original crystalline structure was observed for  $\text{GeTe}_4$  which included Ge-Te and Te-Te bonds at 2.8 Å, this is to be expected since the starting configuration originated from a crystalline phase. These bonds belong to 3-Fold defective-octahedral and planar structures with some minor 4-Fold planar geometries. After the addition of  $\text{As}_2\text{Se}_3$  the system retained its crystalline state even after quenching down from liquid phase which are the characteristics of a memory switching material. The metallic electronic states of the system is mostly caused by the additional Se-centered 3/4-Fold atoms with Te ligands, Thus we confirm that the switching behaviour in chalcogenide glasses can be characterized by thermal models as suggested in the literature. Moreover, we confirm that  $\text{Ge}_{54}\text{Te}_{216}\text{As}_{20}\text{Se}_{30}$  material with its high melting temperature and its ability to retain the crystallinity even after melt-quenching process is a good candidate for memory switching devices.

## References

- [1] You, B. K. et al. “Self-Structured Conductive Filament Nanoheater for Chalcogenide Phase Transition”. English. In: *ACS Nano* vol. 9, no. 6 (2015). Cited By :16, pp. 6587–6594.
- [2] Ovshinsky, S. R. “Reversible electrical switching phenomena in disordered structures”. English. In: *Physical Review Letters* vol. 21, no. 20 (1968). Cited By :2581, pp. 1450–1453.
- [3] Wetnic, W. and Wuttig, M. “Reversible switching in phase-change materials”. English. In: *Materials Today* vol. 11, no. 6 (2008). Cited By :125, pp. 20–27.
- [4] Koelmans, W. W. et al. “Projected phase-change memory devices”. English. In: *Nature Communications* vol. 6 (2015). Cited By :63.
- [5] Burr, G. W. et al. “Phase change memory technology”. English. In: *Journal of Vacuum Science and Technology B: Nanotechnology and Microelectronics* vol. 28, no. 2 (2010). Cited By :663, pp. 223–262.
- [6] Yamada, N. “Origin, secret, and application of the ideal phase-change material  $\text{GeSbTe}$ ”. English. In: *Physica Status Solidi (B) Basic Research* vol. 249, no. 10 (2012). Cited By :55, pp. 1837–1842.

- [7] Park, W. I. et al. “Hierarchically self-assembled block copolymer blends for templating hollow phase-change nanostructures with an extremely low switching current”. English. In: *Chemistry of Materials* vol. 27, no. 7 (2015). Cited By :11, pp. 2673–2677.
- [8] Tsendin, K. D. “Physics of switching and memory effects in chalcogenides”. In: *Univ.J.Phys.Appl.* vol. 2 (2014). Cited By :3, pp. 53–59.
- [9] Raoux, S., Welnic, W., and Lelmini, D. “Phase change materials and their application to nonvolatile memories”. English. In: *Chemical reviews* vol. 110, no. 1 (2010). Cited By :546, pp. 240–267.
- [10] Park, J. H. et al. “Reduction of RESET current in phase change memory devices by carbon doping in GeSbTe films”. English. In: *Journal of Applied Physics* vol. 117, no. 11 (2015). Cited By :25.
- [11] Oike, H. et al. “Phase-change memory function of correlated electrons in organic conductors”. English. In: *Physical Review B - Condensed Matter and Materials Physics* vol. 91, no. 4 (2015). Cited By :18.
- [12] Kolobov, A. V., Fons, P., and Tominaga, J. “Understanding Phase-Change Memory Alloys from a Chemical Perspective”. English. In: *Scientific Reports* vol. 5 (2015). Cited By :30.
- [13] Le Gallo, M. et al. “Evidence for thermally assisted threshold switching behavior in nanoscale phase-change memory cells”. English. In: *Journal of Applied Physics* vol. 119, no. 2 (2016). Cited By :48.
- [14] Rodgers, J. et al. “Proc. of the IEEE Nonvolatile Memory Tech. Symp. NVMTS Pacific Grove CA”. In: (2008). Cited By :1.
- [15] Fazio, A. “Tech. Dig”. In: *Int.Electronics Devices Meet* (2009). Cited By :2.
- [16] Adler, D. et al. “Threshold switching in chalcogenide-glass thin films”. In: *Appl.Phys.Lett.* vol. 153 (1980). Cited By :1, pp. 289–309.
- [17] Warren, A. C. “Switching mechanism in chalcogenide glasses”. English. In: *Electronics Letters* vol. 5, no. 19 (1969). Cited By :55, pp. 461–462.
- [18] Nardone, M. et al. “A unified model of nucleation switching”. English. In: *Applied Physics Letters* vol. 94, no. 10 (2009). Cited By :61.
- [19] Hudgens, S. “Progress in understanding the Ovshinsky Effect: Threshold switching in chalcogenide amorphous semiconductors”. English. In: *Physica Status Solidi (B) Basic Research* vol. 249, no. 10 (2012). Cited By :15, pp. 1951–1955.
- [20] Bogoslovskiy, N. A. and Tsendin, K. D. “Physics of switching and memory effects in chalcogenide glassy semiconductors”. English. In: *Semiconductors* vol. 46, no. 5 (2012). Cited By :36, pp. 559–590.
- [21] Giannozzi, Paolo et al. “QUANTUM ESPRESSO: a modular and open-source software project for quantum simulations of materials”. In: *Journal of Physics: Condensed Matter* vol. 21, no. 39 (Sept. 2009), p. 395502. DOI: [10.1088/0953-8984/21/39/395502](https://doi.org/10.1088/0953-8984/21/39/395502).

- [22] Errington, Jeffrey R. and Debenedetti, Pablo G. “Relationship between structural order and the anomalies of liquid water”. In: *Nature* vol. 409, no. 6818 (Jan. 2001), pp. 318–321. DOI: [10.1038/35053024](https://doi.org/10.1038/35053024).
- [23] Silvestrelli, Pier Luigi et al. “Atomic Structure of Glassy GeTe<sub>4</sub> as a Playground to Assess the Performances of Density Functional Schemes Accounting for Dispersion Forces”. In: *The Journal of Physical Chemistry B* vol. 124, no. 49 (Nov. 2020), pp. 11273–11279. DOI: [10.1021/acs.jpcc.0c08628](https://doi.org/10.1021/acs.jpcc.0c08628).
- [24] Ribaldone, Chiara, Dragoni, Daniele, and Bernasconi, Marco. “A first-principles study of the switching mechanism in GeTe/InSbTe superlattices”. In: *Nanoscale Advances* vol. 2, no. 11 (2020), pp. 5209–5218. DOI: [10.1039/d0na00577k](https://doi.org/10.1039/d0na00577k).
- [25] Gabardi, S. et al. “Microscopic origin of resistance drift in the amorphous state of the phase-change compound GeTe”. In: *Physical Review B* vol. 92, no. 5 (Aug. 2015). DOI: [10.1103/physrevb.92.054201](https://doi.org/10.1103/physrevb.92.054201).
- [26] Pumlianmunga et al. “The mechanism of memory and threshold switching in (GeTe<sub>4</sub>)<sub>100-x</sub>(As<sub>2</sub>Se<sub>3</sub>)<sub>x</sub> glasses”. In: *Journal of Non-Crystalline Solids* vol. 452 (Nov. 2016), pp. 210–219. DOI: [10.1016/j.jnoncrysol.2016.08.044](https://doi.org/10.1016/j.jnoncrysol.2016.08.044).





## Chapter 7

# Conclusion

The study aims at exploring the mechanisms behind memory switching in chalcogenide glasses. As the efficient exploration of the switching behaviour in chalcogenide glasses are an important factor in selector manufacturing and a particular physics model for this phenomenon has not yet been decided on, a thorough investigation of the current possible models is in need.

In chapter 3, we explore the multi-scale modeling solution for high-k dielectric materials used in MOSFETs, the aim was to build a semi-classical model coupled with quantum transport theories which could set the foundation for material characterization at device level. Hence, we introduced a new methodology for characterization of materials properties and defects. Utilizing Multiscale modeling software GINESTRA<sup>TM</sup> we were able to accurately characterize  $\text{La}_2\text{O}_3$  and  $\text{CeO}_2$  material and defect properties by reproducing C-V and J-V measurements. Extracted parameters were consistent with DFT calculation results published by other groups. Finally, results indicated trap-assisted tunneling as the dominant conduction mechanisms. Consequently, The multi-scale modeling based on trap-assisted-tunneling has proven to be accurate in high-k dielectric characterization. Thus, paving route for future exploration of this approach.

Chapter 4, Introduces a tool we developed for the characterization of reliable atomic structure of disordered systems, such as amorphous and glasses since is a fundamental step for most theoretical investigations. Since the properties of short- and medium-range local order structures are responsible for the electronic, optical and transport properties of the disordered systems such as chalcogenide glasses, we present BELLO code, a post-processing script-tool created for the automatic analysis and extraction of structural characteristics of disordered and amorphous systems. BELLO is agnostic to the code that generated single configurations or trajectories. Its capabilities include calculation of order parameter  $q$ , folded structure identification and statistics, and detailed atomic coordination number and pair/angle-distribution functions. Working principles of the code are described and tested on ab initio molecular dynamics trajectories of amorphous  $\text{Ge}_{0.5}\text{Se}_{0.5}$  and  $\text{GeTe}_4\text{As}_2\text{Se}_3$  chalcogenide. The modular nature and the flexibility of the code makes it a great tool for the community to use in different ways. We hope by contributing this code, we will witness it's applications in modern material researches and developments.

In Chapter 5, we have performed classical molecular dynamics (MD) simulations of large-scale  $\text{Ge}_x\text{Se}_{1-x}$  systems in the  $0.4 < x < 0.6$  range to study the structure of their liquid and amorphous phases over nanosecond-long time scales. MD simulations well reproduce all of the main short-range features previously observed by ab initio molecular dynamics and by neutron diffraction studies

for similar systems, such as GeSe<sub>2</sub> and liquid Ge<sub>0.5</sub>Se<sub>0.5</sub>, and provide a reliable model for the amorphous phase at room temperature. Amorphous phases are characterized by different levels of ordering depending on the relative Ge content. In the short range, all systems present a predominant amount of highly folded structures, whose chemical composition differs in the formation of homopolar Ge-Ge bonds, for Ge-rich samples. In the medium range, systems with Ge from 50 to 60% show the formation of a dense and interconnected network with a high percentage of rings, while networks of systems containing a lower Ge content are characterized by a reduced number of disconnected rings. In analogy with other chalcogenide systems, these structural differences are expected to affect the gap properties of Ge<sub>x</sub>Se<sub>1-x</sub> compounds. However, while a different hierarchical short- and long-range order is clearly seen in three examined stoichiometries, its direct effect of the electronic and electrical properties (e.g., ovonic switching) has to be confirmed by specific quantum-mechanical investigations. The success of classical MD simulations in the description of amorphous Ge<sub>x</sub>Se<sub>1-x</sub> structures paves the way to the study of other chalcogenide glasses, including dopants, for applications as OTS chalcogenides materials.

Finally, in chapter 6, we have investigated the effects of As<sub>2</sub>Se<sub>3</sub> additive on GeTe<sub>4</sub> for Memory switching application. As suggested by the experimental reports in [1], addition of As<sub>2</sub>Se<sub>3</sub> to GeTe<sub>4</sub> controls the margin between threshold and memory switching via atomic structure configuration. We confirm that by simulating the melt-quench process in the framework of ab initio calculations coupled within the Carr-Parrinello approach. After the quenching, an amorphous state with remnants of its original crystalline structure was observed for GeTe<sub>4</sub> which included Ge-Te and Te-Te bonds at 2.8 Å, this is to be expected since the starting configuration originated from a crystalline phase. These bonds belong to 3-Fold defective-octahedral and planar structures with some minor 4-Fold planar geometries. After the addition of As<sub>2</sub>Se<sub>3</sub> the system retained its crystalline state even after quenching down from liquid phase which are the characteristics of a memory switching material. The metallic electronic states of the system is mostly caused by the additional Se-centered 3/4-Fold atoms with Te ligands, Thus we confirm that the switching behaviour in chalcogenide glasses can be characterized by thermal models as suggested in the literature. Moreover, we confirm that Ge<sub>54</sub>Te<sub>216</sub>As<sub>20</sub>Se<sub>30</sub> material with its high melting temperature and its ability to retain the crystallinity even after melt-quenching process is a good candidate for memory switching devices.